MAGNETIC BEAD BASED IMMUNOMAGNETIC SEPARATION FOR LAB-ON-A-CHIP DEVICES

Thesis submitted by

Abhishek Samanta

Doctor of Philosophy (Engineering)

Department of Mechanical Engineering
Faculty Council of Engineering & Technology
Jadavpur University
Kolkata, India-700032

2019

JADAVPUR UNIVERSITY

KOLKATA-700032, INDIA

INDEX NO. 275/16/E

1. **Title of the thesis:** Magnetic bead based immunomagnetic separation for lab-on-a-chip devices

2. Name, Designation & Institution of the supervisor/s:

Dr. Nipu Modak
Associate Professor
Department of Mechanical Engineering
Jadavpur University
India

Prof. Ranjan Ganguly
Professor
Department of Power Engineering
Jadavpur University
India

Prof. Amitava Datta
Professor
Department of Power Engineering
Jadavpur University
India

3. List of Publication:

Journal

1. Abhishek Samanta, Nipu Modak, Amitava Datta and Ranjan Ganguly, “Operating Regimes of a Magnetic Split Flow Thin (SPLITT) Fractionation Microfluidic Device for Immunomagnetic Separation” Microfluidics and Nanofluidics, Springer (2016) 20:87, DOI 10.1007/s10404-016-1751-0.
2. Abhishek Samanta, Ranjan Ganguly, Amitava Datta and Nipu Modak,” Separation of magnetic beads in a Hybrid continuous flow microfluidic device”, Journal of Magnetism and Magnetic Materials (JMMM), Elsevier (2017) Vol. 427 p-p 300-305. doi.org/10.1016/j.jmmm.2016.10.143

Book Chapter:

1. Abhishek Samanta, Ranjan Ganguly, Amitava Datta and Nipu Modak, ”On-Chip Microfluidic Separation of Biological Entities in Field Flow Fractionation and Split Flow Thin Fractionation Devices” Book ISBN: 978-81-322-2741-0, Chapter No.: 130, 1361-1369 Fluid Mechanics and Fluid Power – Contemporary Research, in Lecture Notes in Mechanical Engineering, Springer, DOI 10.1007/978-81-322-2743-4_130, 2017

4. List of Patents:NIL

5. List of Presentations in National / International / Conferences / Workshop:

International Conferences:

1. Abhishek Samanta, Ranjan Ganguly, Amitava Datta and Nipu Modak “On-chip microfluidic separation of biological entities in field flow fractionation and Split flow thin fractionation devices” by in 5th international and 41st national conference on Fluid Mechanics and Fluid Power, IIT Kanpur, 2014.

2. Abhishek Samanta, Ranjan Ganguly, Amitava Datta and Nipu Modak, “Separation of magnetic beads in a Hybrid continuous flow microfluidic device”, 11th International

Conference on the Scientific and Clinical Applications of Magnetic Carriers, Vancouver, BC, Canada, 2016.

3. Abhishek Samanta, Ranjan Ganguly, Amitava Datta and Nipu Modak, "Magnetic bead based analyte separation in microfluidic devices by Split Flow Thin Fractionation" 6th International and 43rd National Conference on Fluid Mechanics and Fluid Power, MNIT, Allahabad, India 2016.

4. Abhishek Samanta, Ranjan Ganguly, Amitava Datta and Nipu Modak, "A numerical study on transport and separation of bio-entities in a Lab-On-a-Chip device via Free Flow Magnetophoresis, 5^{TH} International Conference on Emerging Trends in Multidisciplinary Research, National University of Singapore, Singapore 2019.

National Conferences:

1. Abhishek Samanta, Ranjan Ganguly, Amitava Datta and Nipu Modak, Active continuous flow magnetic separation in lab on a chip device, National Conference in Advances in Thermal Engineering, Jadavpur University, Kolkata 2016.

DEPARTMENT OF MECHANICAL ENGINEERING
FACULTY OF ENGINEERING & TECHNOLOGY
JADAVPUR UNIVERSITY
KOLKATA, INDIA

C E RT I F I C A T E

This is to certify that the thesis entitled, "**MAGNETIC BEAD BASED IMMUNOMAGNETIC SEPARATION FOR LAB-ON-A-CHIP DEVICES**", submitted by **Mr. ABHISHEK SAMANTA** who got his name registered on 06.02.2016 for the award of Ph. D. (Engineering) degree of Jadavpur University is absolutely based upon his own work under our supervision and that neither his thesis nor any part of the thesis has been submitted for any degree/diploma or any other academic award anywhere before.

----------	----------	----------
(Dr. Nipu Modak)	**(Prof. Ranjan Ganguly)**	**(Prof. Amitava Datta)**
Signature of the Supervisor and date with Official Seal	Signature of the Supervisor and date with Official Seal	Signature of the Supervisor and date with Official Seal

About the Author

Mr. Abhishek Samanta, the author of this thesis, was born in the year of 1986 in Diamond Harbour, West Bengal, India. Mr. Samanta passed Secondary Examinations from Ramakrishna Mission Siksha Mandir, Sarisha, West Bengal (under West Bengal Board of Secondary Education) with First division, in the year of 2001. He completed his Higher Secondary Examinations from Belsingha Sikshayatan, Belsingha, West Bengal (under West Bengal Council of Higher Secondary Education) with First Division, in the year of 2003. Mr. Samanta obtained his Bachelor's Degree (B. Tech) in Mechanical Engineering from the Birbhum Institute of Engineering and Technology affiliated to West Bengal University of Technology (presently known as, Maulana Abul Kamal Azad University of Technology) in the year 2007 with First class. He qualified GATE 2007 examination in Mechanical Engineering and received scholarship from MHRD for pursuing Master in Engineering degree from the Jadavpur University from 2007 to 2009. He obtained his Master in Engineering in the year of 2009 from Jadavpur University with First class. He has presented research papers in national and international conferences and published several research articles in international journals, and book chapters from his doctoral research.

Acknowledgement

First and foremost, I would like to express much gratitude to all my advisors, Dr. Nipu Modak, Associate Professor, Department of Mechanical Engineering, Jadavpur University, Prof. Ranjan Ganguly, Professor, Department of Power Engineering, Jadavpur University, Prof. Amitava Datta, Professor, Department of Power Engineering, Jadavpur University. I would like to thank them for giving me the chance to work and supporting me throughout my thesis. I have learned how to look at things from a very different perspective under their guidance, during these past six years. They are embodiment of knowledge and wisdom, sincerity and integrity, ingenuity and hard work and yet, humble and very much down to earth. Their contributions to academic fraternity require no special mention. They were always reachable and prepared to answer my numerous queries regarding the doctoral work. Their credentials and work have instilled an attitude that would always encourage me to thrive for excellence. It was an immense learning experience to work with them.

I would like to take this opportunity to convey my sincere regards and reverence to Dr. Prokash Chandra Roy, Associate Professor, Department of Mechanical Engineering, Jadavpur University, for his blessings and encouragement during my work.

I would like to thank to Dr. Gautam Majumdar, Head of the Department and Professor, Mechanical Engineering Department, Jadavpur University, for blessings during my work.

My colleagues and peers in the Department of Production Engineering, whose experiences and knowledge I drew on for numerous tasks, their encouragement during my work has in no way been trivial to me. I appreciate the assistance they provided me when faced with unfamiliar results and methods, no matter how engaged they were.

I would like to thank Uttam Ghosh and Debraj Das, Assistant Professor, Department of Production Engineering and Mechanical Engineering, for constructive fundamental discussions and continuous encouragement.

A most special thanks goes to my family members and friends, who gave me unconditional support, lots of motivation and love throughout this endeavour. Lastly, my son, who brings me joy and laughing with him gives me the strength to move mountains.

Place: Kolkata

Date:

Abhishek Samanta

Dedicated To

My Beloved Family Members

Table of Contents

List of tables

List of figures

Fig. 3.5 Schematic showing the boundary conditions of the hybrid free flow magnetophoretic device.

Fig. 3.6 Basis of computing $\wedge$ (particle number density). Total number $N_{i,j}$ of particle clusters residing in the $(i, j)^{th.}$cell can be computed by Lagrangian tracking of all the particle clusters. After knowing the value of $N_{i,j}$, $\wedge$ can be calculated from Eq. (3.17).

Fig. 3.7 Shows the velocity and pressure at the cell faces and centers respectively.

Fig. 3.8 Grid structure for the flow simulations for the (a) FFF, (b) SPLITT and (c) hybrid free flow magnetophoretic devices.

Fig. 3.9 Particle trajectories from different initial positions (x_0, y_0) mapped from the present numerical code (dashed line) and the analytical results (continuous line) obtained by Nandy et al. [6].

Fig. 4.1 (a) Host fluid velocity profile, and (b) the axial variation of axial velocity throughout the channel along AA′, BB′, and CC′ for the base case operation (see Table 4.1).

Fig. 4.2 Particle trajectories in the magnetophoretic SPLITT device for the base case as shown in Table 4.1.

Fig. 4.3 Particle capture efficiencies (a) CE_1 as a function of Π_1 $(a_1^2\chi_{eff,1}P^2)/(\mu U_{av})$ and (b) CE_2 as a function of Π_2 $(a_2^2\chi_{eff,2}P^2)/(\mu U_{av})$ for the SPLITT device. Results show that all the parametric plots collapse on a single curve, representing how *CE* values depend upon different parameters (dipole strength *P*, magnetic susceptibility χ, particle size *a*, fluid viscosity μ and fluid velocity U_{av}).

Fig. 4.4 Particle separation indices (a) SI_1 as a function of Π_1 $(=\beta^*_1\gamma)$ and (b) SI_2 as a function of Π_2 $(=\beta^*_2\gamma)$. *SI* plots are segregated nearly to two basic trends: one for the constant β^* (i.e.,

varying γ) case and the other for constant γ (i.e., varying β^*) case. Here, $\beta^* = a^2\chi_{eff}$ and $\gamma = P^2/(\mu U_{av})$.

Fig. 4.5 Variation of SI_1 and SI_2 as functions of γ for $\Pi_1 = 4.0\times10^{-7}$ A^2m^5/N and $\Pi_2 = 1.69\times10^{-7}$ A^2m^5/N (corresponding to the base values). The corresponding β^*_1 (= 2.37 β^*_2) is plotted along the secondary x axis.

Fig. 4.6 Variation of CE_1 and CE_2 with variation of length of (a) outlet1, $L_{S,O1}$, (b) outlet3, $L_{S,O3}$.

Fig. 4.7 Variation of particle trajectories for different channel outlet length (a) $L_{S,O1} = L_{S,O2} = L_{S,O3}$=0.5 mm (b) $L_{S,O3}$=0.2 mm, $L_{S,O1} = L_{S,O2}$ =0.65 mm.

Fig. 4.8. Variation of CE_1 and CE_2 with length of outlet O_1, $L_{F,O1}$ when $L_{F,O1} + L_{F,O2}$ = 2.4 mm.

Fig. 4.9 Particle trajectories in different outlet length (a) $L_{F,O1}$ = 1.8 mm, $L_{F,O2}$ = 0.6 mm and (b) $L_{F,O1} = L_{F,O2}$ = 0.6 mm.

Fig 4.10 Particle trajectory of two different types magnetic microspheres (Red and turquoise ones) and one nonmagnetic microsphere (Black) inside the device at base operating regime as shown in Table 4.4.

Fig. 4.11: (a) Large magnetic particle and **(b)** small magnetic particle capture efficiency, CE_1 and CE_2 as a function of Π_1 $\{=(a_1^2\chi_{eff,1}P^2)/(\mu U_{av})\}$ and Π_2 $\{=(a_2^2\chi_{eff,2}P^2)/(\mu U_{av})\}$ respectively for the microfluidic device. Results confirmed that CE values depend upon different magnetic and fluidic operating parameters (dipole strength P, magnetic susceptibility χ, particle size a, fluid viscosity μ and fluid velocity U_{av}), since all the parametric plots collapse on a single curve.

Fig. 4.12: Depicts nonmagnetic particle capture efficiency CE_3 as a function of ξ $\{=(a_3\mu U_{av})\}$ for the microfluidic device. Results show that all the fluidic parametric plots collapse on a

single curve, showing, how *CE* values depend upon different operating parameters (particle size a, fluid viscosity μ and fluid velocity U_{av}).

Fig. 4.13 (a) Large and **(b)** small magnetic particle separation index SI_1 and SI_2 as a function of Π_1 and Π_2. Results clearly separate out two basic trends as one for β^*_1 ($=a_1^2\chi_1$) and the other is γ ($=P^2/U_{av}\mu$).

Fig. 4.14 Smallest nonmagnetic particle separation index SI_3 as a function of ξ. Results clearly separate out two basic trends as one for a_3 and the other is for γ^* ($=U_{av}\mu$).

Fig. 4.15 Particle trajectories in the magnetophoretic hybrid free flow magnetophoretic device for the base case (Tables 4.5 and 4.6).

Fig. 4.16 Particle trajectories for (a) $H_1 = H_4 = 0.0005$ m and $H_2 = H_3 = 0.0005$ m, and (b) $H_1 = H_4 = 0.0004$ m and $H_2 = H_3 = 0.0006$ m. Variation of *CE* (c) and *SI* (d) with the passage area of the channel. Area of the passage is increased by simultaneously reducing the heights of blocks B_2 (H_2) and B_3 (H_3) in steps of 500 μm and increasing those of B_1 (H_1) and B_4 (H_4) equally. Vertical dotted lines denote the base case (blue), case-a (red) and case-b (green).

Fig. 4.17 Particle trajectories for (a) $L_2 = 0.0041$ m and (b) $L_2 = 0.0035$ m. Variation of *CE* (c) and *SI* (d) with the position of the $Outlet_1$ (shown in terms of L_2). Vertical dotted lines denote the base case.

Fig. 4.18 Particle trajectories for (a) $O_3 = 0.00035$ m, $O_2 = 0.00065$ m and (b) $O_3 = 0.0007$ m, $O_2 = 0.0003$ m. L_2 (= 0.004 m) and L_3 (= 0.0015 m) are chosen from the optimum values observed in Fig. 2.14. Variation of *CE* (c) and *SI* (d) with the relative widths of outlets O_2 and O_3.

Fig. 4.19 Variation of *CE* (a) and *SI* (b) with H_5. Vertical dotted lines denote the best configuration for the range of study described in Table 4.7.

Fig. 4.20 Particle trajectory at optimized channel geometry.

List symbols

a	Radius of the particle (μm)
Λ	Particle density
dt_L	Time step for integration for Lagrangian tracking (s)
$\hat{e}_r, \hat{e}_\phi$	Unit vectors along r and ϕ
$\mathbf{F}_\mathrm{d}$	Drag force by the fluid on a particle (N)
$\mathbf{F}_\mathrm{m}$	Magnetic force on a particle (N)
$\mathbf{H}$	Magnetic field (A/m)
$\mathbf{B}$	Magnetic Induction
Ω	Permeability of the material
W	Height of the channel (m)
$\underline{\underline{\mathbf{I}}}$	Unit tensor
$K_{wall}\left(K_{wall}^{\perp}, K_{wall}^{ll}\right)$	Wall drag multipliers
Θ	The ratio of the particle diameter to its distance from the wall
k_n	Number of particle cluster entering the channel every dt_L time interval
N_c	Number of particles per cluster
N_{part}	Particle flux into the channel ($m^{-2}s^{-1}$)
P	Dipole strength (A/m)
p	Pressure (Pa)
p_0	Atmospheric pressure (Pa)
$\mathbf{M}$	Magnetic Dipole Moment (Am^2)
$\mathbf{m}$	Atomic Moments (Am^2)
μ_r	Relative permeability of a material
$\mathbf{r}$	Position vector (m)
t	Time (s)
T	Absolute temperature (K)

U_{av}	Average flow velocity (ms^{-1})
(x, y)	Coordinate references
(X_{mag}, Y_{mag})	Coordinates of the virtual origin of the line dipole (m)
χ_{eff}	Effective magnetic susceptibility of magnetic microspheres
χ_i	Intrinsic magnetic susceptibility of magnetic microspheres
μ	Viscosity (Pa-s)
μ_0	Permeability of vacuum (1.257×10^{-6} NA^{-2})
ϕ	Angular position
ρ_p	Density of particle (kgm^{-3})
ρ	Density of fluid (kgm^{-3})
$\underline{\underline{\tau}}$	Stress tensor (Nm^{-2})
$\boldsymbol{\Pi}$	$(a_2^2\chi_{eff,2}P^2)/(\mu U_{av})$ **(**A^2m^5/N)
β^*	$a^2\chi$ (m^2)
γ	$P^2/\eta \mathbf{U}_{av}$ ($A^2m^3N^{-1}$)
ξ	$(a\mu U_{av})$
γ^*	$1/U_{av}\mu$
∇p	Pressure gradient

List of abbreviations

LOC	Lab-On-a-Chip
μTAS	Micro Total Analytical System
HDF	Hydrodynamic Filtration
CTC	Circulating Tumour Cell
DNA	Deoxyribonucleic acid
IgG	Immunoglobulin G
IgM	Immunoglobulin M
ELISA	Enzyme-Linked Immunosorbent Assay
SEB	Staphylococcal Enterotoxin B
SPC	Stem and Progenitor Cell
FFF	Field Flow Fractionation
FIFFF	Flow Field Flow Fractionation
HFFIFFF	Hollow-fiber Field Flow Fractionation
SdFFF	Sedimentation (Sd) Field Flow Fractionation
GrFFF	Gravitational Field Flow Fractionation
ThFFF	Thermal Field Flow Fractionation
EIFFF	Electrical Field Flow Fractionation
MgFFF	Magnetic Field Flow Fractionation
DIFFF	Dielectric Field Flow Fractionation
SPLITT	Split Flow Thin Fractionation
CHO-K1	Chinese Hamster Ovary
BSA	Bovine Serum Albumin
DLLME	Dispersive Liquid-Liquid Microextraction

HGMF	High Gradient Magnetic Field
T_{CP}	Cloud-Point Temperature
MEMS	Micro Electro Mechanical System
MEPs	Magnetic Extraction Phases
I	Inlet
O	Outlet
ISs	Inlet Splitters
OSs	Outlet Splitters
$L_{F,O1.2,3}$	Length of the outlet in FFF device
$L_{S,O1,2,3}$	Length of the outlet in SPLITT device
CFL	Courant-Friedrichs-Lowy
CEi	Capture Efficiency
SIi	Separation Index
B	Block
HCl	Hydro Chloric Acid
MCF-7	Michigan Cancer Foundation-7 (breast cancer cell)
AFLP	Amplified Fragment Length Polymorphism (PCR-based tool used in genetics research)
CD4	Cluster of Differentiation 4
JM	Jurkat cell line

Abstract

Magnetic particles are widely used in Lab-On-a-Chip (LOC) devices for several applications, as it offers several advantages over other separation techniques. Using the externally applied magnetic field, various magnetic and nonmagnetic species can be manipulated in microfluidic format. Herein numerical studies are carried out for magnetophoretic separation in various continuous flow bio-separators. Eulerian-Lagrangian approach is considered for solving the particle-laden flow in the microchannels. A numerical code is developed based on SOLA-an explicit finite difference technique to solve coupled mass and momentum equations for the liquid phase. A staggered grid is used to describe the field variables. The diffusion terms and the advection terms are discretized using central differencing scheme. Both the stability criteria and the Courant-Friedrich-Lewy criteria have been satisfied to calculate the time increment for solving the continuum phase; the time increment ensures that a fluid element never cross a single cell in one-time step.

Initially, using the developed code, separation of two different type magnetic microspheres are studied in a micro-scale magnetic split flow thin fractionation (SPLITT) device for single phase background fluid medium. The device is characterized in terms of capture efficiency (*CE*) and separation index (*SI*) for each types of particles collected at their designated outlets. This study confirms the significant impact of operating parameters in capturing the microspheres at the outlets. Influence of the outlet positions in capturing the magnetic microspheres in a SPLITT and field flow fractionation (FFF) device is also carried out. This study confirms that, among the two devices, the FFF yields an overall better performance when the designated outlet widths are same for the given operating conditions. Next, a hybrid microfluidic device comprising of SPLITT, Field flow fractionation (FFF) and free flow magnetophoresis is proposed for

separating magnetic and nonmagnetic particles and characterized through *CE* and *SI*. From this study it is found that the influence of operating parameters, are very sensitive in capturing the magnetic microspheres but are not significant in separation of nonmagnetic microspheres. Thereafter influence of geometry in capturing the magnetic and nonmagnetic particles is observed for the hybrid free flow magnetophoretic device. This study confirms that position of outlets has significant effect on particle separation, as geometry can change the particle trajectory.

Keywards: *Lab-On-a-Chip, Microfluidics, Magnetophoresis, Split flow thin (SPLITT) fractionation, Field flow fractionation (FFF), Free flow magnetophoresis.*

Chapter one: Introduction

1.1 The concept of Lab on a Chip

The concept of lab-on-a-chip (LOC) or micro-total analysis system (μ-TAS) was introduced first in 1990 [1], which realized miniaturization of chemical, mechanical, fluidic, electro-mechanical or thermal systems for analytical applications. As a result of miniaturization, the processing power increases and/or the economic cost reduces. This miniaturization has given rise to many new areas like microfluidics-based biosensors, microreactors, and micro-actuators. μ-TAS are used for analyte identification and/or quantification purposes. Microreactors are used for chemical synthesis or energy production. Microfluidics concerns about the precise control of fluids with sufficiently low volumes of micro to nanolitre range, with the channel dimensions of tens to hundreds of micrometers. At the macroscale fluid flow, volume forces usually dominate, whereas, in microflows, surface force and surface interactions dominate. Manipulation of fluids at the micro scale with precise control over targeted concentrations, fulfil much of the world's requirements [2].

The LOC technology speeds up the analysis and reaction times because of short diffusion distances, high surface to volume ratios, fast heating, and small heat capacities. This technology is field-deployable, and allows drastic reductions in reagent and energy consumptions and the amount of waste produced. It also ensures better process control (due to the faster response of the system), compactness (because of the integration of multiple functionality and small volumes). Massive parallelization becomes possible because of

compactness, which allows high-throughput analysis and safer platform for chemical, radioactive or biological studies because of the integration of functionality, smaller fluid volumes, and stored energies.

A continuous effort is being made for improving global health [3] by scientists and researchers. The LOC technology possibly will become a significant part of these efforts by the development of numerous point-of-care testing devices [4], when the technology will be completely developed. Personalized medication is another feat of healthcare technology that will leverage on the emergence of fast, affordable microfluidic diagnostic devise. The LOC technology assures the researcher that this technology can be the key to develop such important new diagnostic instruments. The main intention of these researchers throughout the globe is to develop such LOC devices which will help the healthcare providers in poorly prepared health centers to conduct diagnostic tests such as immunoassays and nucleic acid assays without major laboratory supports.

Microfluidics ensures a viable solutions for chemical and biological challenges in the analytical devices; for instance, handling of small volumes of sample like proteins or DNA solutions [5,6], in vitro applications like selective separation of target analytes [7,8,9], point-of-care or in-the-field detection application or tumour cells separation from a mixed cell population such as peripheral blood, or bone marrow in metastasis research [10] – all have become possible because of the recent advent in microfluidic technology.

1.2 Magnetic materials and magnetism

Magnetic force can play an important driving role in clinical diagnosis or in healthcare applications like separation of ferromagnetic impurities from boiler water or removal of

magnetic coloured impurities from kaolin clay [11,12]. Application of magnetic field in Lab-On-a-chip devices is increasing day by day, due to its benefits over other external fields like electrical field, acoustic field, etc. For transporting, sorting or separation, use of the electric field in microfluidics is a widely used technique for long times, though magnetic field offers several advantages over the electric field. If electric field is used in the microfluidic environment, bio-species can be affected by Joule heating, surface charges, pH and ionic concentrations, etc. Magnetic field eliminates all these demerits. Nowadays, the magnetic field is also widely used in microfluidics, not only for manipulating the magnetic particles or magnetically loaded bio-entities but also for manipulating the nonmagnetic particles. Applications of the magnetic field includes separation, mixing, pumping etc.

Due to the movement of an electric charge, like current flows in a coil of wire, magnetism arises. There are certain materials which exhibit magnetism or respond to a magnetic field even though no free current is flowing through them. Magnetism for such materials thus originates from the spinning of an electron as well as from the orbital motion of electrons around the nucleus. Magnetism is fundamentally manifested as the magnetic force noticed as mutual attraction or repulsion between certain materials, and the space in which this force can be observed is referred to as the magnetic field. As the magnetism is originated from the movement of electric charge, magnetic field strength **H** in SI units are expressed as Am^{-1}. The magnetic induction **B** is the response of a given material or free space to the externally applied magnetic field. There is a relationship between the magnetic induction, permeability of the material (Ω) and magnetic field strength as

$$\mathbf{B} = \Omega\mathbf{H} \qquad \textbf{.....(1.1)}$$

If a magnetic material is placed within an externally applied magnetic field, the orientations of the individual dipole moments are changed and the material gets magnetized.

The magnetic moment **m** of a magnetic dipole is a vector, relating the torque $\boldsymbol{\tau}$ acting on the dipole in a magnetic field of magnetic induction **B**

$$\tau = \boldsymbol{m} \times \mathbf{B} \qquad \textbf{…..(1.2)}$$

For relating the magnetic properties of a material to the magnetic induction, the magnetization **M,** due to any individual electronic or atomic moments **m** existing in the sample, can be expressed as the magnetic moment per unit volume:

$$\mathbf{M} = \frac{1}{\mathrm{V}} \sum_{\mathrm{V}} \mathbf{m} \qquad \textbf{…..(1.3)}$$

The degree of magnetization depends upon the strength of the applied magnetic field and the materials. Any material, whether magnetic or not, can be determined by a quantity called magnetic susceptibility χ, which describe the material's magnetic behaviour. This magnetic susceptibility gives the magnetic response of a material through a relationship, as

$$\mathbf{M} = \chi.\mathbf{H} \qquad \textbf{…..(1.4)}$$

Where **M** is the magnetization of the magnetic material, **H** is the applied magnetic field strength (Am^{-1}). Magnetic susceptibility can also be measured using magnetic permeability of free space and relative susceptibility ($\mu_0 = 4\pi \times 10^{-7}\ NA^{-2}$). The relative susceptibility can be expressed as

$$\chi_r = \frac{\chi}{\mu_0} \qquad \textbf{……(1.5)}$$

Relative permeability of a material is the ratio of permeability of a specific medium to the permeability of free space can be expressed as

$$\mu_r = \frac{\Omega}{\mu_0} \qquad \textbf{…...(1.6)}$$

There are different types of magnets which can be used in microfluidic applications. Use of these magnets is application-specific. For instance, for getting the magnetic field in a discrete manner, (i.e., with a provision of switching “on” or “off”) only electromagnet [13] with a soft iron core can be used. Similarly, if the continuous magnetic field is required then permanent magnet [14,15] is essential. Both types of magnets offer some merits and demerits. Like soft or electromagnet can generate Joule heating, whereas by using permanent magnet, there will be no possibility of Joule heating. The permanent magnet cannot be used in a discrete manner though it can provide rapid, easy, highly selective, and inexpensive separation. In different research articles, it is found that for generation of the magnetic field, iron oxide or steel bar or different ferromagnetic wire [16] or different alloy (Nd-Fe-B [17,18],) can be used. According to the susceptibility, the magnetic materials can be divided into diamagnetic, ferromagnetic and paramagnetic ones. Due to negative magnetic susceptibility, diamagnetic particles try to move towards the regions of minimum magnetic field strength. On the contrary, paramagnetic particles are attracted towards the magnetic field, as it has positive magnetic susceptibility. Ferromagnetic particles are strongly attracted by magnetic fields. Superparamagnetic particles – a special type of paramagnetic particles with no magnetic memory – behave as magnetic when subjected to an imposed magnetic field, but return to nonmagnetic state after removal of the magnetic field.

Red blood cell (due to the presence of paramagnetic haemoglobin) and magnetostatic bacteria (that create intracellular chains of magnetic nanoparticles) show magnetic characteristics. But all other type bio-entities do not have any intrinsic magnetic characteristics. Therefore, for magnetic separation of those nonmagnetic entities, one requires them to bind to the micro or

nano magnetic particle through some functional attachment [19]. These are often achieved to specific and/or nonspecific binding through chemical or physical routes. Using ferrofluids (solution of nano magnetic particles in one fluid medium) is another option for magnetophoretic separation of nonmagnetic bio-entities. Inside magnetic field, ferrofluid move towards the magnet and nonmagnetic entities move towards the opposite side [20]. If the number of magnetic flux density remains constant in a space then the magnetic field is homogeneous otherwise it is inhomogeneous. Application of homogeneous magnetic field is from magnetohydrodynamic pumping to NMR spectroscopy, while the inhomogeneous magnetic field is widely used for separation or sorting purposes.

1.3 Magnetic bead

Magnetic bead, the spherically-contoured matter, can be viewed as encapsulated magnetic nanoparticles in an organic or aqueous carrier medium as shown in Fig. 1.1. A magnetic bead consists of magnetic nanoparticle core surrounded by the nonmagnetic coatings for selectively binding the biomaterial of interest (e.g., a specific cell, protein, or DNA sequence). The size of the beads can be varied from a few nanometers to micrometers. When these beads are used for separating different bio-species like DNA, bacteria, Circulating Tumor Cell (CTC), etc., they need to be bonded with the required nonmagnetic bio-species. Therefore, the surface of the beads should be functionalized for making a covalent bond with the bio-species. For these types of therapeutic applications, the bead matrix should have the capability of biocompatibility, biodegradability, stability and required size to reach specific target locations [21,22]. When these beads come under a magnetic field, they remain insensitive to the biochemical environment. As iron has the highest magnetic moment among different ferromagnetic transition metals, frequently, iron oxide is used as the nanomagnetic particle

fillers in the beads. When a magnetic material is placed in the magnetic field of strength **H**, produced by the free current, it induces a magnetic dipole moment **M**. Then the corresponding

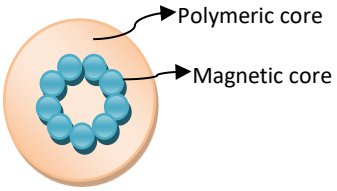

Fig. 1.1 Schematic diagram of a bead consisting of magnetic nanoparticles surrounding a polymeric core.

magnetic induction may be written as $\mathbf{B} = \mu_0(\mathbf{H} + \mathbf{M})$, where μ_0 ($=4\pi \times 10^{-7}$ N A^{-2}) denotes the permeability of free space. Atomic structure and temperature command the magnetic quality of the material. In terms of their volumetric magnetic susceptibility (χ), **M** can be roughly assumed to vary with the **H** as $\mathbf{M}=\chi\mathbf{H}$, which describes the magnetization induced in a material by the magnetic field.

1.4 Immunoassay

Immunoassay is an analytical method, which employs the immunochemical binding between antibodies and antigen [23]. Such assays are developed, based on the exclusive ability of an antibody to bind with high specificity to an antigen [24] and widely used for diagnosis, chemical analysis, and screening [25]. For measuring the amount of antigen present in a solution, an immunoassay often requires the use of a marker or a labelled material. Immunoassays offer several advantages like they are

a) Stable, soluble and abundant.

b) Simple to manufacture and immobilize.

c) Available with single binding (monoclonal) or multiple binding (polyclonal) receptors.

d) Available in monovalent fragments apart from bivalent, Immunoglobulin G (IgG), and polyvalent, Immunoglobulin M (IgM).
e) Able to bind with natural and man-made chemicals, bimolecular, cells and viruses.
f) Highly specific and have high binding constants between an antibody and its target.

Immunoassays can be classified into two major groups like heterogeneous and homogeneous assays. Heterogeneous formats necessitate separation of surface-bound and free labels before quantifying the assay signal. On the other hand, homogeneous assays do not require this type of separation step. Therefore, homogeneous assays faster, simpler, and more suitable for automation. Also, homogeneous immunoassay needs fewer handling steps compared to a heterogeneous assay. In lab-on-a-chip devices, small dimensions help in reducing the time needed for the reactions, and the low quantities of reagents can result in a cutdown of costs of the immunoassay.

Magnetic bead-based immunoassays

Magnetic immunoassay uses magnetic bead in replacement of conventional enzymes (ELISA), radioisotopes, for detecting analytes. The magnetic immunoassay comprises of the specific binding of an antibody to its antigen, where a magnetic label is conjugated to one element of the pair. This type of immunoassay offers various merits like, it can be conducted in a liquid medium, where other methods like ELISA require a stationary medium for the desired target to bind before the secondary antibody. As the immunoassay can be conducted in a liquid medium, more accurate measurements can be obtained. Also, the detection can occur in many different techniques. The most basic form of detection is to run a sample through a gravity column that contains a polyethylene matrix with the secondary antibody. The targeted compound is bounded to the antibody contained in the matrix, and any residual substances are

washed out using a chosen buffer. The magnetic antibodies are then passed through the same column and after an incubation period, any unbound antibodies are washed out using the same method. The results obtained from the captured antibodies on the membrane is used to quantify the target compound in solution. This method is used to detect viruses in plants.

Magnetic bead-based assays have several applications in bio-medical field. Among various toxins, Staphylococcal enterotoxin B (SEB) is formed by the Gram-positive bacterium Staphylococcal aureus. The SEB is the responsible agent of certain food poisons. Therefore, quick and precise identification of SEB during either surveillance or in response to a biothreat is required. For detecting this the magnetic bead-based immunoassays can be used. Alefantis et al., [26] developed an improved method to detect the SEB, based on an SEB-specific and two-antibody system – one antibody bound to a magnetic bead while the other was labeled with Alexa Fluor 647. Using the assay, they purified 100 pg of recombinant SEB, as well as SEB from the culture supernatant of several strains of methicillin-resistant S. aureus were detected. This assay provides enrichments over existing assays by the reduction in assay time length, assay sensitivity, ease of use, and application to automated high-throughput analysis.

1.5 Magnetophoresis

Magnetophoresis is the manipulation of magnetic, nonmagnetic or magnetizable (such as a hemoglobin-bearing red blood cell) materials in a fluid medium. When a magnetic particle or magnetic particle-attached species are separated in a nonmagnetic fluid medium, it is called positive magnetophoresis. On the other hand, if nonmagnetic species are separated using a magnetic field in a magnetic fluid medium, it is called negative magnetophoresis. First magnetophoresis was studied in 1977 [27]. Magnetic fields are very useful for clinical applications as it has no side effects. The US Food and Drug Administration, approved human

exposure limit to static magnetic fields are 4 Tesla (T) for the entire body raised [28] and 5T for a limb [29]. Magnetic separation is one of the simplest and fastest method of separation with respect to other separation methods. With respect to electrophoresis, magnetophoresis has several advantages like inside samples there is no chance of generation of heat. Therefore, for soft particles like cells, DNA or other cell composites, magnetophoretic separation is non-invasive. As a result, magnetic beads can be attached with those nonmagnetic soft particles like cells, DNA or other cell composites [30,31] to modify surface chemistry, physical properties and further multifunctional capabilities for separation. As the magnetic field has the capability to penetrate different materials from a safe distance, it can be used to manipulate

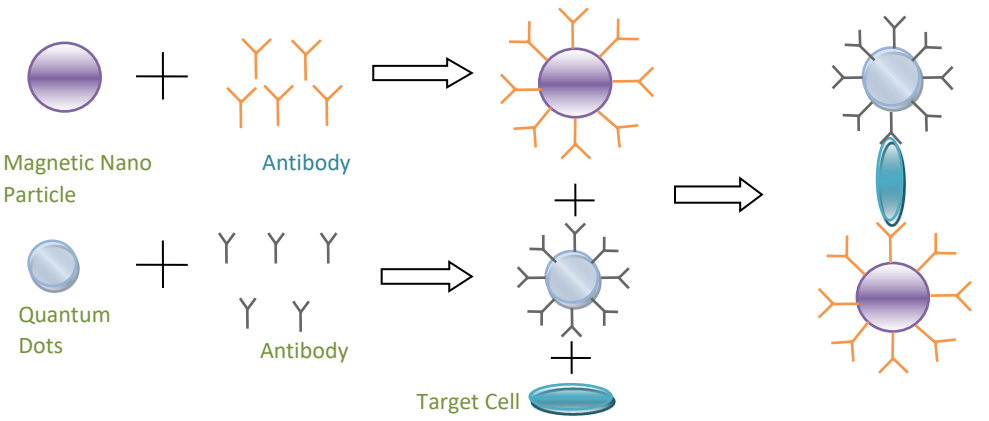

Fig. 1.2 Schematic view of magnetic particles, target cells and antibody conjugate.

targeted bio-species without direct contact. These different advantages accelerate the use of magnetophoresis in microfluidic separation [32,33] protocol. Some biological entities like, red blood cells, “magnetic” bacteria have intrinsic magnetic properties. Therefore, these type species can be separated with the help of a magnetic field. Most of the bio-species does not possess any intrinsic magnetic property. Hence, to separate those non-magnetic species using a magnetic field, one requires some special arrangement. The special arrangement includes

generation of magnetic property surrounding that species artificially. Artificial generation of magnetic property surrounding a non-magnetic species can be done by attaching magnetic micro or nano beads with the parent non-magnetic species as shown in Fig. 1.2. Therefore, both the magnetic as well as non-magnetic species can be separated easily by magnetophoresis. If the species have an intrinsic magnetic property, it can be separated without using any micro or nano bead attachment and this type of separation can be referred to as direct separation. However other type of species which does not have any intrinsic magnetic property requires the special arrangement of micro or nano magnetic bead attachment, after which the species can be separated by using an external magnetic field gradients. This type of separation can be referred to as an indirect mode of separation. Also, nonmagnetic species can be manipulated in magnetic fluid through remote manipulations of their magnetic chaperons.

There are many applications of magnetophoretic separation, for example, attachment of magnetic bead on the cell [34], separation of Fetal Nucleated Red Blood Cell from Maternal Blood [35], fractionation of a stem and progenitor cell (SPC) population [36], separation of MCF-7 breast cancer cells [37], elimination of rabbit apoptotic spermatozoa from insemination sample [38], separation of protein by using silica-coated superparamagnetic nanoparticles [39], capture and separation of target protein by using aptamer modified magnetic beads [40], capturing of cancer biomarker proteins [41], sorting of JM (human lymphocyte cell line) cells by using anti-CD4 immunomagnetic beads [42], or superparamagnetic bead-based fast isolation by AFLP [43].

1.6 Microfluidic techniques for separation

Separation is one of the most important applications of microfluidic technology. There are many techniques available for separating targeted particles or cells. Separation may be performed by continuous or segmented carrier flow configurations in the microchannel. Continuous flow separation configuration offers advantages over segmented flow type, like in the former type, the separation parameters can be adjusted at once and separation efficiency can be monitored in real-time [44]. Besides there is high throughput and potential for scale-up operations. If separation is performed without using any external force (except the pumping mechanism that drive the flow), it is referred to as a passive mode of separation where separation is performed by the various microfluidic flow phenomenon and with a variation of the geometry of the microfluidic channel. The passive separation may take place by using obstacle induced separation [45], hydrodynamic filtration [46], inertia and dean flow [47], pinched flow fractionation [48]. On the other hand, if any external force field like magnetic, electrical, acoustic, optical, etc is applied for accelerating the separation, it is referred to as an active mode of separation. Separation of the targeted species can be performed in a single carrier flow medium or in a two-phase carrier flow medium. For example, separation of targeted tumor cells from nontargeted ones can be done in a single carrier fluid medium. Likewise, separation is done with the external force field for single carrier fluid configuration, like Field Flow Fractionation (FFF), Split-Flow Thin Fractionation (SPLITT) and Free Flow Magnetophoresis, etc. Separation in binary phase medium in microfluidic configurations is also gaining recent traction. [49].

1.6.1 Field flow fractionation (FFF)

The massive expansion of analytical methods in the lab on a chip or micro total analytical systems requires excellent separation techniques of biological species. There are several techniques for separation of magnetic or nonmagnetic particles; one of the most important technique is field flow fractionation (FFF). J. Calvine Giddings in 1966 first illustrates about FFF method [50]. FFF devices are basically elution-based active type of microfluidic devices which takes help from some external force field, imposed transverse direction, to achieve axial separation of target species in the flow. This separation technique offers several advantages [51,52] like (a) wide variation of separation speed, (b) the entire sample can be recovered and fractions can be collected for additional methods of analysis (c) various FFF sub-techniques permit analysis of macromolecules with molecular weights (d) parallel processing with multiple separation channels is possible, (e) batch fabrication with reduced costs, (f) potentially disposable systems, etc. Depending on the particle size, FFF techniques are sometimes categorized as: (i) normal [53] for small particles (<0.5μm), (ii) steric [54] for medium (0.5-10μm) ones and (iii) cyclical [55] for large (>10μm) particles. In normal FFF (Fig 1.3(a)), macromolecules and sub-micrometer particles gravitate under an externally imposed force and accumulate on the wall (or exit through their designated channels). However, smaller, sub-micrometer particles exhibit a small "stand-off" distance from the wall due to Brownian fluctuation, which counters the imposed external force (e.g., the magnetic force). The Brownian motion predominates for particles of size of 40nm or less [56]; therefore, the smaller particles will be more affected by the Brownian motion and move further away from the accumulation wall. This, coupled with the fact that the axial velocity in the channel increases as one moves away from the wall, renders a finite "slip" of the smaller particles in the

downstream direction with respect to the larger particles. Hence, the smaller particles are found to collect at the downstream of the larger particles. For particles of larger size (0.5–10 μm), steric mode of FFF plays a role (as shown in Fig. 1.3 (b)). Since the particle size is well above the 40nm threshold, Brownian diffusion is negligible, and field-induced segregation leads to particle build-up on the wall. However, larger particles in such situation protrude out to a greater extent (than the smaller ones) in the shear layer near the wall. This leads to a larger fluidic drag on the larger particles than that on the smaller ones, leading to an axial separation between the particles. The larger particles move into streamlines faster than the smaller one, which is the opposite situation of the normal mode. This is why it is also referred to as a reversed FFF mode. For even larger particles (>10μm), i.e., the hyper layer FFF, hydrodynamic lift force becomes important, and particles with different sizes experience different lift forces, therefore stabilizing at different stand-off distances from the wall [57]. The steep velocity gradient in the flow, as a consequence separates the particles axially as the particles move through the separator (see Fig. 1.3(c)). Here separation does not entirely depend on size but also on other material properties of the element such as profile and deformability.

Field flow fractionation (FFF) devices have a wide range of applications, good resolution, and versatility. Different fields that can be used in separating particles in FFF are like flow FFF [58], hollow-fiber FFF [59], sedimentation FFF [60], Gravitational FFF[61], Thermal FFF [62], Electrical FFF [63], Magnetic FFF (MgFFF)[64], Dielectric FFF (DIFFF)[65], etc.

In magnetophoretic FFF, magnetic bead-analyte conjugates with different magnetophoretic mobility are segregated along the axial length of the channel – particles with the larger magnetophoretic mobility segregates near the wall of high field gradient at the upstream location while those having lower magnetophoretic mobility collect at the downstream location

(see Fig. 1.4). By suitably arranging the outlets along the separation wall, the particles of different mobilities can be segregated in a continuous flow system. Relative magnetophoretic mobility of different beads would depend not only on their size, but also on magnetic properties (e.g., magnetic susceptibility). In the magnetic FFF device, a transverse magnetic field gradient is established in the microfluidic channel that causes the particles to move towards one wall, and eventually escape through the designated channel outlet.

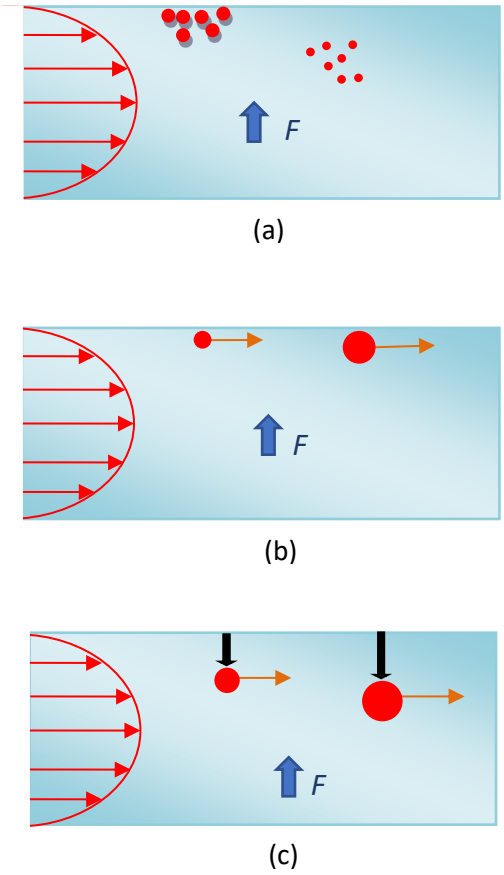

Fig. 1.3 Different FFF operating modes under a transverse force field (shown by the blue arrow). Based on particle size different mechanisms of separation of particles in FFF (a) normal, (b) steric and (c) hyper layer mode.

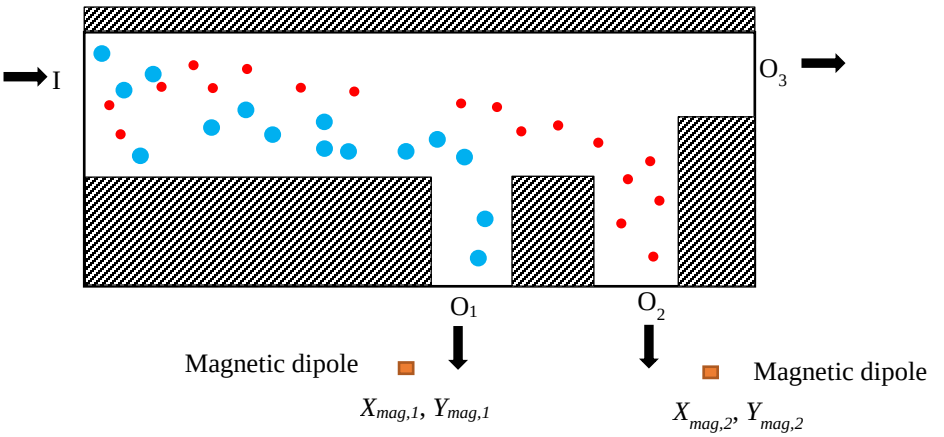

Fig. 1.4 Schematic of the magnetic field flow fractionation device.

1.6.2 Split flow thin fraction (SPLITT)

Split flow thin fraction (SPLITT) is a variant of field flow fractionation. SPLITT is one preparative scale continuous flow separation technique, where the separated particles leave the device in more than one number of co-flowing streams as shown in Fig. 1.5. The SPLITT channel consists of more than one inlet and outlet, separated in the transverse direction by thin separators, thus forming a ribbon-like a channel. The sample containing a mixture of analytes and carrier fluid is fed into the channel through a single inlet, while the other inlets carry buffer

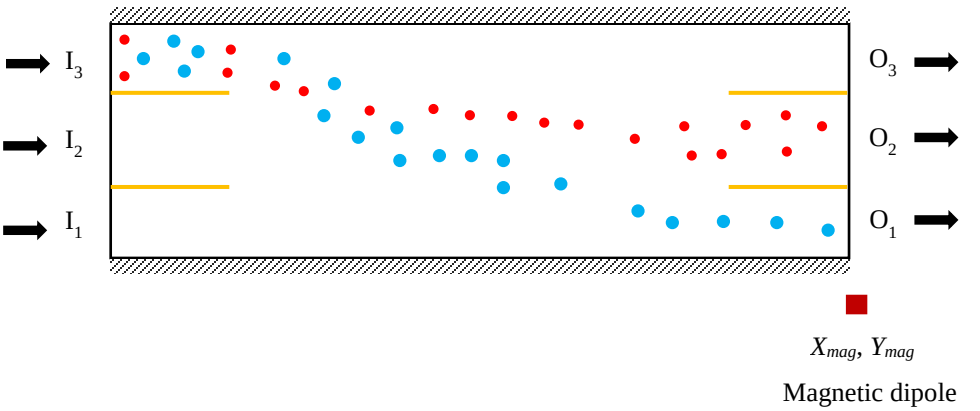

Fig. 1.5 Schematic of the microchannel for magnetophoretic Split Flow Thin Fractionation device.

solution. Under the external force field, the separation is achieved when the analytes obtain differential migration velocity across the streamlines. An ideal binary separation happens when each analyte type elutes separately through the two different outlets that are separated by a splitter wall. In addition to the externally applied primary forces e.g., the gravitational, centrifugal, magnetic, or electric, for driving the separation, secondary forces like lift forces may influence the overall separation process [66,67,68,69,70,71,72,73,74]. SPLITT fractionation allows a more compact design (co-flowing outlet streams can be laid over a shorter width instead of bifurcation or branching needed for sorter or FFF designs), they are effective only for separating target moieties from large sized non-targeted ones (> 1µm, so that its diffusional transport-induced cross contamination to non-designated outlet is minimal). Researchers have attempted for separating micro-sized particles using the SPLITT device. These have wide applications in biology, medical, environmental fields.

1.6.3 Free flow magnetophoresis

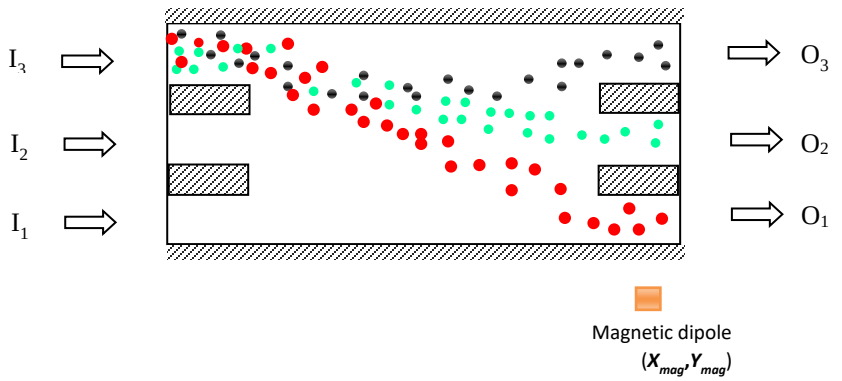

Fig. 1.6 Schematic of the microchannel for free flow magnetophoresis device.

Free flow magnetophoresis is a variant of SPLITT device, nonmagnetic particles-analyte conjugates are separated from one or more types the magnetic particle-analyte conjugates in a single device. Like the SPLITT or FFF, the magnetic is imposed transverse to the flow

direction as shown in Fig. 1.6. In this type of separation protocol, different types of magnetic and nonmagnetic particles are introduced into the microchannel through a single inlet. As the particle suspension enters the zone of magnetic influence, particle trajectories segregate out depending upon their levels of magnetophoretic mobility, based on their magnetic property or size. Intuitively, the nonmagnetic particles follow the fluid flow direction, not affected by the magnetic field. Complete separation in this process warrants that each particle type ensues through their designated outlets.

1.7 Societal Impacts

Microfluidic technology offers significant contributions in clinical, biomedical, industrial environmental fields. As a result, the technology has become very popular. It is clear that miniaturization helps the society a lot, irrespective of the underlying physics for building functional units. Still, some of the commitments of the technology have yet to be fulfilled, as it is one developing area.

The field of microfluidics is a consistently growing area since it is consistently getting better accessibility and applicability to a range of areas facilitating better living, ranging from environmental monitoring to low-cost biomedical assays. Lab-on-a-chip devices deploying various immunomagnetic separation systems can significantly cut down the costs of undertaking the interventions [2]. Microfluidic bioseparation devices can impact, in a beneficial way, the point-of-care diagnostics industry and basic healthcare services [75]. Such devices have also significant potential for mass deployment of environment monitoring and invigorating environmental consciousness. With the advent of wireless technology and internet of thing (IoT), development in microfluidic biosensor can lead to widespread, interconnected,

intelligent environmental monitoring systems that is expected to buttress societal wellness and sustainability in an unprecedented scale. At the individual level, the greatest benefit to human life will perhaps come in the form of the lab-on-a-chip based, wearable sensors offering protective care at the individual level – also known as personalized medication [76]. Food and water quality monitoring through microfluidic sensor is another means that integrates the microfluidics technology very well in the social framework [77].

Chapter two: Literature review and scope of present work

2.1 State of the art

In the microfluidic protocol, magnetophoretic separation is one important aspect, in which different magnetic and nonmagnetic species can be separated using magnetic field in continuous flow configuration. There are several applications of the magnetophoretic separation using various methods. Details of the applications and characterizations of the magnetophoretic separation for continuous flow configurations studied previously are discussed below.

Several researchers have demonstrated proof-of-concept and prototype operation of magnetic separators that follow the principle of magnetic separation, trap, flow sorter or flow fractionation for a single-phase flow in the background medium. Magnetophoretic fractionation is an important tool in lab-on-a-chip devices deploying micro total analytical systems (μ-TAS). In a microfluidic immunomagnetic flow-fractionation platform, target biological entities (e.g., DNA, protein molecules or biological cells) are selectively bound to functionalized magnetic particles of different magnetophoretic mobility and the bead-analyte conjugates are subsequently separated using a suitably designed magnetic field for downstream processing, e.g., purification, detection [78] or separation [79, 80, 81, 82, 83]. Such devices may be deployed not only in highly selective biosensors but also for rendering point of care diagnostics and personalized medication [84]. Several techniques of microfluidic separation are in use for separating cells, nucleic acids of other biological entities based on the

difference/contrast in their physical properties with respect to the background fluids or the non-target entities in the background fluid. Microfluidic separators have relied on physical manipulation of target moieties using hydrodynamic technique [85], acoustic [86, 87], optical [88, 89], dielectric [90- 94] forces, besides magnetic tweezing [95]. However, such hydrodynamic filtration techniques offer some limitations also, which comprises poor separation resolution [96], an intricate chip design due to microstructures [97], and inadequate isolation markers [98]. Magnetophoretic separation has several merits over other active modes of separation. For example, inertial and acoustic separations do not work well when the density contrast of the target and non-target entities is small. Acoustic waves may also lead to mechanical damage to a living organism, e.g., leading to cell lysis [99]. Likewise, electrophoretic separation entails Joule heating in the fluid and/or charge-induced damage to analyte samples [87,88]. Magnetophoretic separation, on the other hand, uses a static magnetic field, which is not harmful to living species. This aspect is particularly important for biological applications like magnetophoretic cell separation, which needs to be non-invasive. Besides, the magnetic field can penetrate various non-conductive materials like plastic, glass or even living tissue; magnetic particles exhibit stark magnetic contrast with respect to most biological entities. Therefore, biological entities can be manipulated in a microchannel irrespective of the intervening medium once they are biochemically conjugated to magnetic microspheres.

In a trap design, the magnetic particles and bio-conjugated analytes are separated from the host stream and may be collected at the side-wall of the channel [100]. Based on this principle, *Choi et al.* developed a magnetic bead-based, filter less bio-separator with planar electromagnet surfaces for bio-molecule sampling and detecting applications. *Choi et al.*, [13], in another study, designed, fabricated and tested a new planar bio-magnetic bead separator on a glass

chip. The separator is made of micromachined semi-encapsulated spiral electromagnets and fluid channels, which is separately fabricated and then bonded. They tested the device with super-paramagnetic beads of mean diameter 1 μm. While these traps can have high capture efficiency [9], they are better suited for batch operation only. Continuous in-line operation warrants flow sorting devices, where the magnetic particles (and the conjugated moieties) are magnetically deflected/diverted inside the microchannel in a transverse direction (with respect to the flow); the particle trajectories are altered in a way that they are collected in a separate steady outflow stream.

Several sorter designs have been proposed in the literature. While most designs offer bifurcating outlets of the channels [101, 102], some [103] proposed trifurcating microchannel design for on-chip separation of magnetic particles. *Carr et al.*[104] used a magnetic field to build an apparatus for parallel and multiplexed bioassay sorting with a chamber that had the possibility to collect 25 different output fractions. Sorter design offers an effective means of in-line purification and enrichment of magnetic bead-bound analyte [105-107]. *Modak et al.* [108] characterized the separation efficiency in a T-channel sorter and argued that a cascade of such separators can be employed to have multiplicative enrichment of sample. In a notably different configuration, *Kirby et al.* [109] used both centrifugal and magnetophoretic forces on a rotating microfluidic platform (also known as lab-on-a-CD) for separating particles according to their physical properties (e.g., size and magnetization), the distribution of the magnetic field, and the programmable spin speed of the microfluidic chip. *Mizuno et al.*, [42] presented a simple microfluidic system to perform continuous two-parameter cell sorting based on size and surface markers. Immunomagnetic bead-conjugated cells were initially sorted based on size by utilizing the hydrodynamic filtration (HDF) scheme, introduced into individual

separation lanes, and simultaneously focused onto one sidewall by the hydrodynamic effect. They successfully achieved the continuous sorting of JM (human lymphocyte cell line) cells using anti-CD4 immunomagnetic beads and confirmed that accurate size- and surface marker-based sorting has taken place. In addition, the sorting of cell mixtures was performed at purification ratios higher than 90%.

Some works are also found in the literature for increasing the capture efficiency of magnetophoretic separators. Capture efficiency can be increased by increasing the aspect ratio of embedded soft-magnetic elements inside the microchannel or alternatively, by decreasing the spacing between the magnetic elements [110]. A key finding in that study was that the total capture efficiency increased with the addition of the first few elements to the array, but then remains essentially constant as more elements were added. This implies that scale up for high throughput separation can best be realized by parallelizing the process, i.e. by replacing a single channel with a large number of magnetic elements with a parallel arrangement of shorter channels having fewer elements. Separation of magnetically-labeled bioparticles can be enhanced using integrated soft-magnetic elements [111]. The elements were fixed and intersect the carrier fluid (flow-invasive) with their field oriented in the transverse direction to the flow. The bioparticles were magnetized using a bias field to produce a particle capture force. Multiple stair-step elements were used to provide efficient capture throughout the entire flow channel. In contrast to conventional systems, wherein the elements were integrated into the walls of the channel, restricts efficient capture to limited regions of the channel due to the short-range nature of the magnetic force. This severely limits the channel size and hence throughput. Flow-invasive elements overcome this limitation and enable microfluidic bio separation systems with superior scalability. However, the trap and sorter designs are not

capable of fractionating two or more types of magnetic particles and therefore could not offer simultaneous selective isolation of two different types of target analytes from a suspension of non-target entities.

In magnetophoretic separation, the magnetic particles are always attracted towards the region of larger magnetic field strength. As the particles gravitate towards a dipole in a magnetophoretic configuration, the force-field further increases, and the particles eventually get trapped, often in a narrow zone of influence. This can limit the selective separation of magnetic particles of different magnetic mobility. A special class of microfluidic separation that relies on negative magnetophoresis, overcomes this challenge. In this method, nonmagnetic particles are suspended in a magnetic liquid (e.g., ferrofluid), such that these particles migrate towards the regions of lower magnetic field (i.e., away from the dipole) as they move through the separation channel [112]. The technique has been adopted to achieve controlled manipulation [113] and rapid separation [114] of nonmagnetic particles and cells. An additional advantage of this technique is that it enables label-free detection of non-magnetic biological entities since one does not need to "tag" magnetic particles to the biological moieties to impart magnetophoretic mobility [115]. However, magnetophoretic fractionation of more than one moiety from the background fluid without a magnetic label is not possible in this method. *Zhu et al*., [116] extended this technology to combine both positive and negative magnetophoresis based on ferrofluids, which could separate mixtures of magnetic and non-magnetic particles, or even particles whose magnetophoretic mobility differ even marginally. *Cheng et al.,* [117] presented an analytical model that can predict the three-dimensional (3D) transport of non-magnetic particles in magnetic fluids inside a microfluidic channel coupled with permanent magnets. *Zeng et al.,* [20] utilized a pair of permanent magnets to continuously

separate diamagnetic particles and cells in ferrofluid flow through a straight microchannel. The first magnet was placed close to the microchannel for focusing the particle mixture to a single stream without the use of a sheath flow. The second magnet, which was offset from the first magnet and placed farther from the channel, to displace the aligned particles to dissimilar flow paths for a continuous sorting. This idea was demonstrated through the separation of 3 μm and 10 μm-diameter polystyrene particles, where the effects of both flow speed and distance of the magnet are examined. Using the same technology *Tarn et al.*, [118] explored the potential of a microfluidic continuous flow particle separation system based on the repulsion of diamagnetic materials from a high magnetic field. Two particle sizes (5 and 10μm) were examined in two concentrations of $MnCl_2$ (6 and 10%). The larger particles were repelled to a greater extent than the smaller ones, and the effect was greatly enhanced when the particles were suspended in a higher concentration of $MnCl_2$. However, use of ferrofluid as host liquid in a bio-separation application would warrant additional constraint of its biocompatibility, and may also pose limitations in downstream optical or magnetic detection of the separated fractions.

Pamme and Manz [119] developed a continuous magnetophoretic system, where a microsphere suspension containing 2 and 4.5 μm diameter magnetic and 6 μm diameter nonmagnetic (polystyrene) particles were separated into three distinct streams containing predominantly each type of particle alone. Particles escaped through different outlets depending upon their size and the position of the magnet. *Pamme et al.* [120], separated magnetic particles from mixtures of magnetic particles by on-chip free-flow magnetophoresis. In a continuous flow environment, the magnetic particles were deflected from the direction of laminar flow by a perpendicular magnetic field depending on their magnetic susceptibility, size and the fluid flow rate. In this process, particles of 2.8 and 4.5 μm diameters were completely separated from

each other reproducibly. *Liu et al.,* [121] investigated the separation of two types of magnetic particles (4.5 and 2 μm in diameter). They studied the motion of the particles of varying sizes when actuated using an alternating traveling magnetic field produced by four-phase conductors on the chip. Magnetic particles of different sizes migrate with different speeds under the same magnetic field. By carefully choosing the frequency of the magnetic field, different magnetic particles separated in the microfluidic system. *Adams et al.* [122] used micro-fabricated ferromagnetic strips of various designs in a flow channel to separate two different targets moieties into separate fractions from the background non-targeted cells.

Field flow fractionation (FFF) is an advanced version of magnetic sorting where a bi-dispersed or poly-dispersed suspension of particles (or particle-analyte conjugates) can be selectively separated into streams of monodispersed particles, based on their physical and magnetic mobility in the host fluid [123]. FFF offers the advantages of simultaneous separation and measurement, and hence, is useful in biomolecules and cell separation and diagnosis [124] and biosensors [125]. *Modak et al.* [126] numerically studied the separation of the magnetic microspheres of two different sizes in an FFF device under a crossways magnetic field. For variations of particle size, susceptibility, magnetic dipole strengths, positions, fluid viscosity, and flow velocity, they measured the capture efficiency and separation index at the exits. In another study *Modak et al.,* [127] observed how the geometry of a micro-channel affects separation phenomenon in FFF device. *Vickrey et al.,* [64] evaluated the separation capability by defining the theoretical basis of the parameters of force on each particle and normal FFF parameters. There many force fields which can be used to separate the particles in a microchannel but in magnetic FFF, magnetic dipole moment generates in the particles which help in their interaction and separate them due to the magnetic field. This phenomenon was

examined by *Williams et al.* [128]. *Carpino et al.,* [129] found a quadrupole magnetic FFF system as a potential and an influential separation device for magnetic particles.

Split flow thin fraction (SPLITT) is a derivative of the field-flow fractionation (FFF), where the separated particles leave the device generally in three or more co-flowing streams separated in the transverse direction. While this type of separation allows a more compact design (co-flowing outlet streams can be laid over a shorter width instead of bifurcation or branching needed for sorter or FFF designs), SPLITT separators are effective only for separating target moieties from large sized non-target ones (> 1μm, so that its diffusional transport-induced cross contamination to non-designated outlet is minimal). Several researchers have attempted separation of micro-sized particles using the SPLITT device. This technique has widely used in biology, medical, environmental applications [130-136]. Several studies attempted design improvement of magnetic SPLITT devices. *Zhang et al.* [137] developed a general approach to optimize flow-rates in a SPLITT device for particle separation. *Williams et al.* [138] found the influence of small splitter imperfections on the resolution of migrating particles. *Zhang* and *Emerson.* [139] observed the key deviations between the predicted and experimentally observed transport behavior of particles in a SPLITT device. *Fuh et al.* [17] analyzed the performance of a magnetic SPLITT fractionation device for magnetic particles of different susceptibilities. They reported that a SPLITT separator not only invokes design complications, but the device had restricted operational simplicity [140].

One primary challenge in a magnetic SPLITT device is that the transverse separation between the outflowing streams are typically less than 500 μm, which makes the separator vulnerable to cross-contamination if the operating parameters are not chosen accurately. It is therefore very crucial to operate a SPLITT separator at a desirable condition so that the throughput is

maximized and non-specific cross-over is minimized. Researchers have tried to address these practical difficulties by appropriate physical dimensioning of the inlet and outlet splitting planes [140]. *Hoyos et al.* [141] used Halbach array to create a localized magnetic field that can provide an enhanced magnetic selectivity for transverse separation of the magnetic particles [142]. In another study *Hoyos et al.*, developed a continuous magnetic sorting process based on the quadrupole magnetic field centered on an annular flow channel, using the conceptual framework of split-flow thin (SPLITT) fractionation. To eliminate the variability inherent in working with a heterogenous cell population, they developed a set of monodisperse magnetic microspheres of a characteristic magnetization, and magnetophoretic mobility, similar to those of the cells labeled with a magnetic colloid.

2.2 Gap areas

Going through the literature related to microfluidic separation using various configurations, it is observed that there are certain areas in which more studies will be required for better understanding of the phenomena involved. The identified gap areas from the study are as follows.

1. The literature lacks a comprehensive characterization of the operating regimes of a magnetic SPLITT micro separator to separate magnetic particles (and the bio conjugated entities) of different mobilities. It is very crucial to find out the optimum operating regime for a magnetic SPLITT device to selectively isolate the different mobility microspheres simultaneously. Along with the operating parameters it is also very significant to find the optimum channel geometry for the maximum channel effectiveness.

2. While FFF design is less compact, SPLITT designs are more vulnerable to cross-contamination. It is therefore essential to maintain the separation throughput and minimize the non-specific crossover in SPLITT device by appropriately designing the microchannel and the magnetic field. Free flow magnetophoresis can separate different magnetic particles with nonmagnetic particles simultaneously. The existing separation protocols can only perform separation based on the presence or absence of magnetization, and therefore, the simultaneous sorting of multiple targets at high levels of purity, recovery, and throughput remains a challenge. System throughput can also be tuned by changing the channel layout. Although the literature is replete with studies on FFF, SPLITT and free flow magnetophoretic devices, there is no report on integrating features of all the designs to develop a hybrid separator in our knowledge. Both the former three types of designs are found to offer narrow operating windows for which the capture efficiency and separation indices are in an acceptable range. It is intuitive from these prior studies that, operating the FFF or SPLITT or free flow magnetophoretic devices with magnetic and nonmagnetic particles are extremely sensitive to any slightest variation of parameters. Also, the geometry of the device is one influential parameter in separating the target analytes, especially for the nonmagnetic particles; however, this attribute is not investigated thoroughly in the literature. Therefore, it is very important to design a hybrid device that can work combining the FFF, and SPLITT and free flow magnetophoresis and obtain optimum operating parameters and channel geometry for getting maximum isolation.

2.3 Objectives of the thesis

Keeping in consideration the state of art on the research in the field of magnetic particle transport in microfluidic environments, and the aforementioned gap area in relevant research, the present study aims at prescribing a new class of approach for separation of magnetic and nonmagnetic microspheres in Lab on a chip (LOC) devices. The objectives of the present work focus the followings.

1. Isolation of particles from a bi-dispersed suspension of magnetic particle-analyte conjugates into a pair of co-flowing streams in a Magnetic SPLITT device is studied. Herein, a numerical study is carried out for describing the influence of hydrodynamic and magnetic forces on the transport and capture of the microspheres in the device. The device is characterized in terms of capture efficiency and separation indices.
2. Influence of the channel geometry of the SPLITT and FFF devices are also very crucial in separation. The impact of the geometry on capture efficiency and separation index are observed by fixing the operating parameters.
3. A numerical study is carried out for characterizing one hybrid microfluidic device, which works on the principle of split-flow thin (SPLITT) fractionation, field flow fractionation (FFF) and free flow magnetophoresis mechanisms. The objective of the proposed hybrid free flow magnetophoretic device is to separate two different types of magnetic and one type of nonmagnetic particles from each other simultaneously. The impact of magnetic and hydrodynamic forces on transport and separation of the three different types of magnetic and nonmagnetic particles are analyzed in terms of capture efficiency and separation indices for different operating parameters.

4. The microchannel geometry also plays a very significant role in the separation process. The flow passage and the position of the outlets will vary with the variation of microchannel geometry. With the variation of channel layout, the particle trajectories will also vary, which will lead to the variation of capture efficiency and separation index under a fixed operating regime. Therefore, one objective of the present study is to find out the impact of channel geometry on separation, for getting maximized capture efficiency and separation index in the hybrid microfluidic device.

With the above identified objectives, the essential background regarding magnetophoresis has been summarized in chapter three, with an emphasis on the transport behaviour of the magnetic microsphere in a flow and magnetic field. The obtained results for the magnetic and nonmagnetic particle separation are analyzed in various continuous flow configurations in chapter four. Finally, chapter five concludes the thesis summarizing the findings from the work, and proposing the recommendation for future works along with closure remarks.

Chapter three: Methodology

3.1 Background

In this chapter, numerical simulation of four different techniques of magnetophoretic separation of microparticles in flow through microfluidic configurations are carried out. First, the separation technique on split flow thin (SPLITT) fractionation is studied. Secondly, a simple representative case of field flow fractionation (FFF) is studied for comparison with the split flow thin (SPLITT) fractionation. More advanced techniques like, hybrid free flow fractionation leveraging magnetophoresis techniques are studied afterwards. Specific description of each system, studied in the work, is provided in the following sections.

3.2 Configurations of particle tracking in continuous flow

The configurations of the SPLITT, FFF and hybrid free flow fractionation devices used for the study are described in the following section.

Split flow thin fractionation (SPLITT) device

Figure 3.1 shows the schematic diagram of the SPLITT device of length L and width W through which a steady pressure-driven flow is envisaged. The device comprises of three inlets, viz., I_1, I_2 and I_3 and three outlets viz., O_1, O_2 and O_3. The co-flowing inlet or outlet streams are separated by two inlet splitters (IS) and two outlet splitters (OS), respectively. All the splitters have finite thickness ($W/8$) and length ($\sim L/6$). The IS_1 and IS_2 allow parallel streams of liquid;

inlets I_1 and I_2 carry buffer solutions, while I_3 carries a dilute suspension of magnetic microspheres of two different magnetophoretic mobilities. The separating section comprises a flow channel

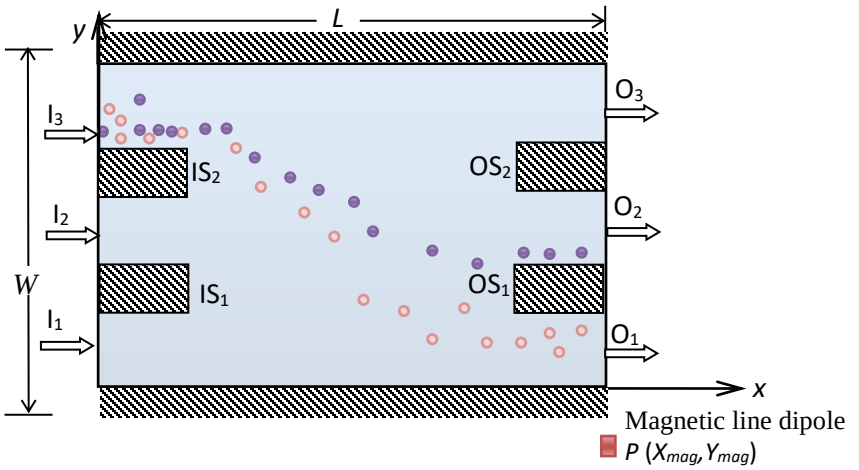

Fig. 3.1: Schematic of magnetophoretic split flow thin (SPLITT) fractionation device. Here, L and W are the channel length and height; the line dipole P is placed at X_{mag} and Y_{mag}; red particles possess larger magnetophoretic mobility than the purple ones). $IS_{1,2}$ and $OS_{1,2}$ denote the inlet and outlet splitters, respectively.

spanning the width W of the channel and a length $2L/3$ where the three streams from the inlet side pass to the outlet ports. A magnetic line dipole is placed at a location (X_{mag}, Y_{mag}) as shown in Fig. 3.1, creating a magnetic field gradient in such a manner that the particles experience a magnetophoretic migration in the transverse direction, collecting at the outlets O_1 and O_2. The third outlet O_3 is designed to flow the buffer and not any particles. With the correct orientation and magnitude of magnetic field, the particles with larger magnetophoretic mobility should exit through the outlet streams O_1 while the other type of particle is expected to separate out through O_2 (Fig 3.1).

Field flow fractionation (FFF) device

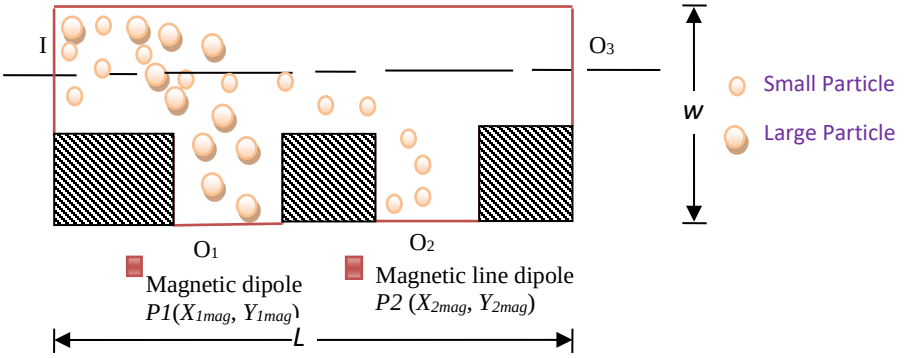

Fig. 3.2 Schematic diagram of a Field Flow Fractionation (FFF) device**.**

Figure 3.2 shows the schematic diagram of the Field Flow Fractionation (FFF) device of length *L* and width *W* through which a steady pressure-driven flow is envisaged. The device comprises of one inlet, viz., I and three outlets viz., O_1, O_2 and O_3. A dilute suspension of magnetic microspheres of two different magnetophoretic mobilities enter the channel from the inlet I. The separating section comprises a flow channel spanning the width *W* of the channel and a length *L* where the stream from the inlet side pass to the outlet ports. Two magnetic line dipole are placed at a location (X_{1mag}, Y_{1mag}) and (X_{2mag}, Y_{2mag}) as shown in Fig. 3.2, creating a magnetic field gradient in such a manner that the particles experience a magnetophoretic migration in the transverse direction, collecting at the outlets O_1 and O_2. The third outlet O_3 is designed to flow the buffer and not any particles. With the correct orientation and magnitude of magnetic field, the particles with larger magnetophoretic mobility should exit through the outlet streams O_1 while the other type of particle is expected to separate out through O_2 (Fig. 3.2).

Hybrid free flow magnetophoretic device

Figure 3.3 illustrate the schematic diagram of the hybrid free flow magnetophoretic separator that has a length *L* and width *W* through which a steady pressure-driven flow is analyzed. The device comprises of two inlets (I_1 and I_2) and three outlets viz., O_1, O_2 and O_3. A homogeneous aqueous buffer suspension carrying three different particle types of equal number density is introduced through inlet$_1$ whereas inlet$_2$ allows only the aqueous buffer solution. For generating a magnetic field gradient in the channel, a magnetic line dipole is positioned at a location (X_{mag}, Y_{mag}) (see Fig. 3.3) in such a manner that the magnetic particles experience a magnetophoretic

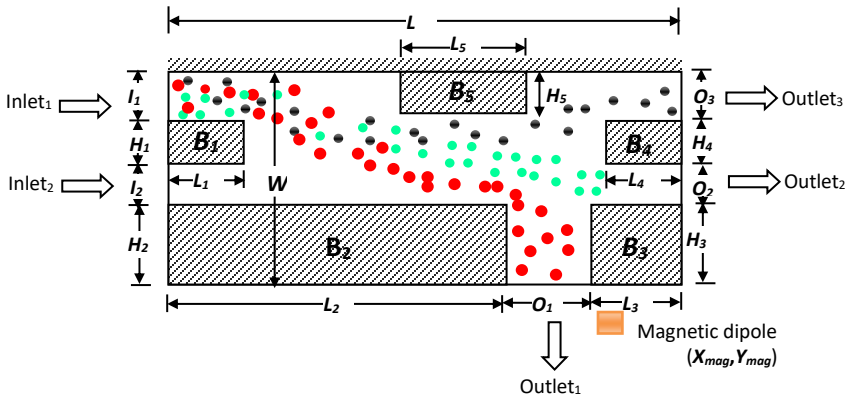

Fig. 3.3: Schematic of magnetophoretic hybrid device and the computational domain; the magnetic dipole *P* is placed at (X_{mag}, Y_{mag}); red dots denote particles having larger magnetophoretic mobility than the turquoise ones; black dots denote nonmagnetic particles; alteration in the flow passage is created by varying the dimensions of the rectangular blocks (solid walls) B_1, B_2, B_3, B_4 and B_5.

movement in the transverse direction, eventually leading them through the outlets (O_1, O_2 and O_3).

3.3 Theoretical formulation for particle transport

Particle trajectory in a fluid medium is influenced by fluidic drag force by the host fluid. When any external force field like magnetic field is applied, particle trajectory is also influenced by the applied external field. Therefore, interplay between the drag and the externally applied

force confirm the mobility of the particle in a single fluid medium. The present section of the chapter, discusses in details about the theoretical formulation for particle trajectory in a single fluid medium under externally applied magnetic field.

3.3.1 Forces on a magnetic particle in the flow

Particles that are transported in a dilute suspension through a microchannel under the influence of a magnetic field experience magnetic body force ($\mathbf{F}_m$), the drag force ($\mathbf{F}_d$) exerted by the fluid (since the particle tends to move with a finite velocity relative to the fluid), the gravitational force ($\mathbf{F}_g$), the thermal Brownian force ($\mathbf{F}_B$) [143]. The equation of motion of a single particle can be cast in the form of Newton's second law as:

$$\left(\frac{4}{3}\pi a^3 \rho_p \frac{d\mathbf{V}_p}{dt}\right) = \left[\mathbf{F}_m + \mathbf{F}_d + \mathbf{F}_g + \mathbf{F}_B\right] \quad \textbf{…..(3.1)}$$

Magnetic force

The magnetic force on a superparamagnetic spherical micro particle, when suspended in a dynamic fluid medium under influence of a magnetic field generated by a line dipole, can be expressed as [144]

$$\mathbf{F}_m = \frac{4}{3}\pi a^3 \mu_0 \chi_{eff} \frac{1}{2}\nabla\left(\mathbf{H}_0.\mathbf{H}_0\right) \quad \textbf{…..(3.2)}$$

$\mathbf{H}_0$ is the local undistorted value of $\mathbf{H}$, μ_0 (= $4\pi \times 10^{-7}$ NA^{-2}) denotes the permeability of free space. The effective magnetic susceptibility χ_{eff} [145] of the particle is deduced from its intrinsic susceptibility χ_i, considering the distortion of the imposed magnetic field due to the existence of the particle itself, such that

$$\chi_{eff} = \frac{\chi_i}{1+(\chi_i/3)} \quad \textbf{…..(3.3)}$$

The magnetic field and its gradient in the microchannel are produced by a line dipole of

strength (P), placed near O_1 (at a location (X_{mag}, Y_{mag}) as shown in Fig. 3.1, 3.2 and 3.3). In a practical bio-MEMS device, such field can be realized practically by embedding pairs of parallel conductors, carrying currents in opposite directions, and buttressing the field by a soft magnetic core. With respect to the virtual origin of the line dipole, the produced magnetic field **H** at any location (r, φ) can be expressed as

$$\mathbf{H} = \frac{P}{r^2}\left(\hat{e}_r \sin\varphi - \hat{e}_\varphi \cos\varphi\right) \qquad \textbf{…..(3.4)}$$

Here it is assumed that a magnetic particle to be a dimensionless point entity. The magnetic force exerted on the particle, when it is under the influence of the line dipole is

$$\mathbf{F}_m = \frac{4}{3}\pi a^3 \mu_0 \chi_{eff} \left(\frac{2P^2 x'}{\left(x'^2 + y'^2\right)^3}\hat{i} + \frac{2P^2 y'}{\left(x'^2 + y'^2\right)^3}\hat{j} \right), \qquad \textbf{…..(3.5)}$$

Where $x' = x - X_{mag}$, $y' = y - Y_{mag}$ denote the positions of a particle w.r.t. the origin of the line dipole.

Fluidic drag force

The viscous drag force can be represented by [63]

$$\mathbf{F}_d = 6\pi a \eta K_{wall}\left(\mathbf{V} - \mathbf{V}_p\right) \qquad \textbf{…..(3.6)}$$

The values of the wall drag coefficient K_{wall} for drag forces parallel and perpendicular to the wall are

$$K_{wall}^{ll} = \left[1 - \frac{9}{16}\Theta\right]^{-1} \text{ , and } \qquad K_{wall}^{\perp} = \left[1 - \frac{9}{8}\Theta\right]^{-1}, \qquad \textbf{…..(3.7)}$$

where, Θ denotes the ratio of the particle diameter to its distance from the wall [146]. However, the other fluid flow mechanisms, like viscoelasticity, capillary effects, and electrokinetic effects may complicate the flow phenomena since their non-linearity increases in small scales.

Gravity force

The gravitational force can be expressed as [147]

$$\mathbf{F}_g = -V\left(\rho_p - \rho\right)\mathbf{g} \qquad \text{…..(3.8)}$$

Where $\mathbf{F}_g$ represents the gravitational force, V, ρ_p, ρ and g represents the volume of the particle, density of particle and fluid, and acceleration due to gravity respectively. If viscosity of the flowing fluid is 0.00089 Pa-S and particle have velocity of 1 mm/s then the fluidic drag force on a micron size microsphere is ~8.4×10^{-12} N. If density of microsphere is 1800 kg/m^3 and fluid is 1000 kg/m^3 then gravitational force on the particle become ~0.033×10^{-15} N. Therefore, gravitational force become very less than drag force, as a result gravitational force can be neglected.

Brownian force

Thermal Brownian force can be expressed as

$$\mathbf{F_B} = \mathbf{R}_d\sqrt{12\pi a\mu k_B T/dt}\,, \qquad \text{…..(3.9)}$$

where R_d is a uniform random number vector whose value is between 0 and 1, k_B the Boltzmann constant, T the absolute temperature and dt is the time interval over which the Brownian force is resolved.

Brownian force become insignificant when particle size exceeds 40 nm [56]. The dimensionless dipole strength

$$P_{M,ND} = \frac{\pi\mu_0 a^3\chi^2\boldsymbol{H}_0^2}{9K_bT} \qquad \text{…..(3.10)}$$

compares the magnetic energy interaction between the particles in an external magnetic field and thermal energy. For example, for a suspension of particles with a = 0.5 μm, χ = 0.1 subjected to a field strength $\mathbf{H}_0$ = 2000 A/m at room temperature, the dimensionless dipole

strength becomes 100, which clearly indicates that the magnetic interactions between particles greatly exceeds the thermal energy, implying that Brownian motion does not play a significant role.

3.3.2 Equation of motion for microparticle transport in continuous flow configuration

A 2 μm diameter polystyrene (density ~ 1800 kg/m^3) particle has very low mass of ~7.5 pg. Due to very small mass of the microsphere, impact of the inertia force on the microsphere is very negligible. The particle inertia force can be ignored for the small particle mass unless the particle acceleration exceeds an unbelievably large value (~1000m/s^2), which is rather unusual for the design of microfluidic channel and the flow regime investigated herein. Among the various other forces described above only drag force and magnetic force play significant role in magnetophoretic transport of microsphere in the present thesis. Therefore, considering the salient forces on a microparticle, Eq. (3.1) can be recasted as

$$\mathbf{V}_{\mathrm{p}} = \mathbf{V} + \frac{1}{6\pi a \mu K_{wall}} \mathbf{F}_{\mathrm{m}} . \qquad \textbf{…..(3.11)}$$

The instantaneous position of any particle can be found by integration of Eq. (3.11) after imposing the initial position of the particle.

The magnetic field and its gradient in the microchannel are produced by a line dipole of strength (P), at a location (X_{mag}, Y_{mag}) as shown in Fig. 3.1, 3.2 and 3.3. In a practical MEMS device such field can be generated by embedding pairs of parallel conductors, carrying currents in opposite directions, and buttressing the field by a soft magnetic core [148]. The instantaneous position of a particle cluster can be computed from integration of the particle velocity, i.e.,

$$x(t) = \int_0^t V_{px} dt + x_0 \qquad \textbf{…..(3.12a)}$$

$$y(t) = \int_0^t V_{py} dt + y_0 \qquad \textbf{…..(3.12b)}$$

Where x_0 and y_0 are the initial position of the particle cluster.

3.3.3 Governing equations

The drag force on particles is influenced by the continuum phase (the host buffer liquid) velocity. Transport of the liquid through the channel follows the conservation of mass and momentum which are expressed as

$$\frac{\partial \rho}{\partial t} + \nabla.\left(\rho \mathbf{V}\right) = 0, \text{ and} \qquad \textbf{…..(3.13)}$$

$$\frac{\partial}{\partial t}\left(\rho \mathbf{V}\right) + \nabla.\left(\rho \mathbf{V}\mathbf{V}\right) = -\nabla p + \nabla.\underline{\underline{\tau_{\upsilon}}} - \varpi \mathbf{F}_{\mathrm{d}}, \qquad \textbf{…..(3.14)}$$

where $\underline{\underline{\tau_v}}$ denotes the viscous stress tensor, expressed as

$$\underline{\underline{\tau_{\upsilon}}} = \mu\left[\left(\nabla \mathbf{V}\right) + \left(\nabla \mathbf{V}\right)^{\mathrm{T}}\right] - \frac{2}{3}\mu\left(\nabla.\mathbf{V}\right)\underline{\underline{\mathrm{I}}}. \qquad \textbf{…..(3.15)}$$

The last term in Eq. (3.14), originates from the reaction of the viscous drag force $\mathbf{F}_{\mathrm{d}}$ (on the particle by the fluid, as evaluated from Eq. (3.6)), while ϖ denotes the local particle density [149].

3.3.4 Boundary conditions

The fluid enters the computational domain in a plug flow velocity profile. The length of the computational domain for all the channels are assumed to be sufficient for achieving a fully developed flow, while a pressure boundary condition is imposed at the exit. At all the walls no-slip boundary condition is assumed.

The boundary conditions considered for the different parameters at the known locations of the computational domain can be summarized as

(i) For the SPLITT device (Fig. 3.4(a)):

At inlets (I_1, I_2 and I_3) (x=0)

$u = U_{av}, v = 0$

At bottom wall (y=0, x=0 to L)

$u = 0, v = 0$

At top wall (y=W, x=0 to L)

$u = 0, v = 0$

At all the walls of every bock (B1, B2, B3 and B4)

$u = 0, v = 0$

At outlets (O_1, O_2 and O_3)

$\upsilon = 0, p = p_0$

(ii) For the FFF device (Fig. 3.4(b)):

At inlet I_1 (x=0): $u = U_{av}, v = 0$

At outlets O_3 (x=L): $v = 0, p = p_0$

O_1 and O_2 (see Fig 3.4): $u = 0, p = p_0$

At top wall (y=W): $u = 0, v = 0$

At all the walls of every block constituting the bottom wall of the channel (B1, B2 and B3):

$u = 0, v = 0$

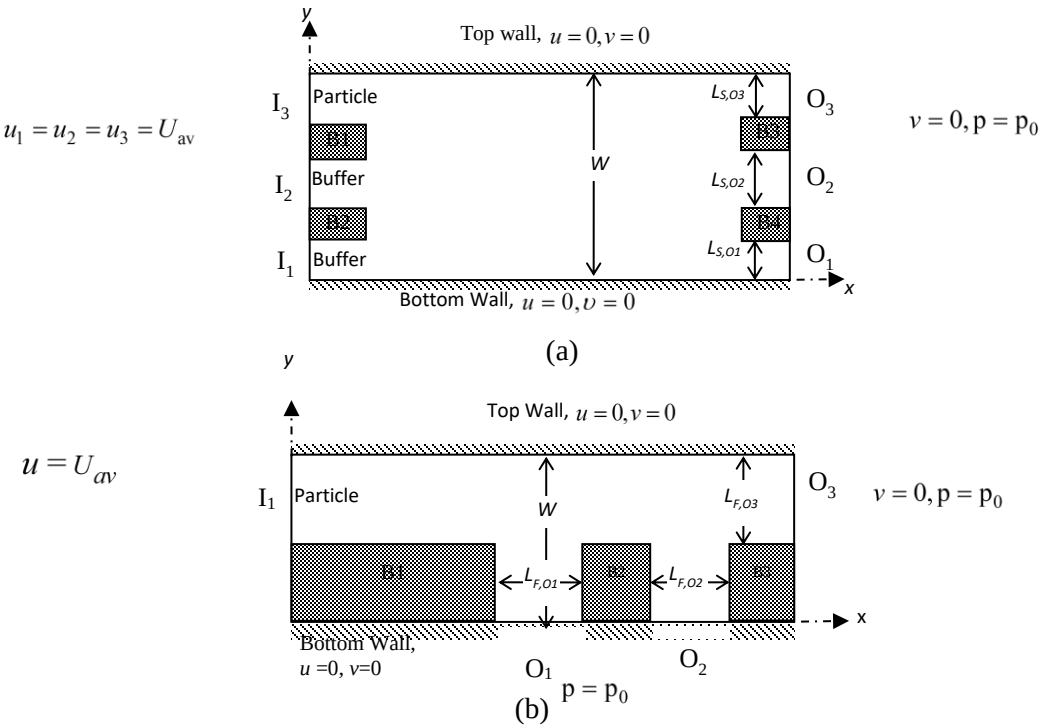

Fig. 3.4 Schematic showing the boundary conditions of (a) SPLITT device and (b) FFF device.

(iii) For the hybrid free flow magnetophoretic device (Fig. 3.5):

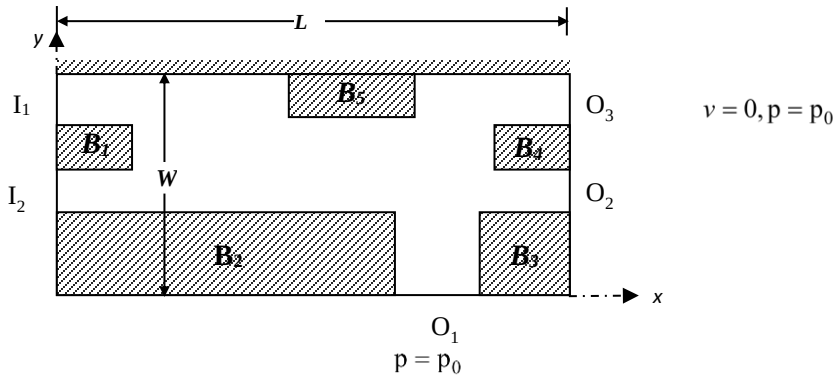

Fig. 3.5 Schematic showing the boundary conditions of the hybrid free flow magnetophoretic device.

At inlets (I_1 and I_2) (x=0)

$u = u_{av}, v = 0$

At the walls (every wall of block 1,2, 3 and 4)

$u = 0, v = 0$

At top wall (y=W)

$u = 0, v = 0$

At bottom outlet (O_1) and

$u = 0, p = p_0$

The outlets at right side (O_2, O_3)

$v = 0, p = p_0$

3.4 Numerical Technique

Particle-laden flow inside the micro-channel is solved using a Eulerian-Lagrangian approach. A numerical code based on SOLA [150], an explicit finite-difference technique, has been developed to solve the coupled mass and momentum equations for the liquid phase. A staggered grid is used to describe the field variables like velocity, pressure and fluid properties. The axial and transverse velocities are specified at the scalar cell faces, while the pressure is specified at the cell-centers. A single layer fictitious cell is used as boundary cells of the fluid region. Considering the low Reynolds number involved in the flow (also verified during the simulations), the highest cell Peclet number ($\rho u \Delta x/\mu$) is well below than 1. Therefore, the diffusion terms and the advection terms are discretized by central differencing scheme [151]. Although the final solutions are sought under a steady state, Eulerian-Lagrangian solutions for the continuum and the dispersed phases are advanced through a sequence of time marching and iteration, until the flow field and the particle trajectories of two consecutive time steps converge. Both the stability criteria and the Courant-Friedrich-Lewy criteria have been satisfied to calculate the time increment for solving the continuum phase; the time increment

ensures that a fluid element never cross a single cell in one-time step. Lagrangian tracking of the particles in the flow-field has been used to solve the dispersed phase (homogeneously distributed suspension of magnetic microspheres). The particles entering through the inlet at a flux of N_{part} (for each particle type) are modeled as a finite number of discrete particle clusters (of each particle type) entering every dt_L second. Trajectory of each particle cluster is traced by time integration of instantaneous velocity for each particle type in a "frozen" continuum flow field. The integration time step dt_L is so chosen that a particle does not move by more than 1% of the scalar cell residing at a particular time step. Number of particles in each such type of cluster can be computed from:

$$N_C = \left(N_{part} / k_n\right) \times \left[\left(W/4 \times 1\right) \times dt_L\right] \qquad \textbf{…..(3.16)}$$

First the fluid phase is solved for a steady velocity profile using the Eulerian approach, and then particle tracking is done in a 'frozen' flow-field. Calculation of the momentum interaction between the particles and the fluid requires evaluation of particle density Λ at each location within the domain. The location of each cluster of particles is calculated at every time plane of Lagrangian tracking. Based on the instantaneous positions of the particle clusters, the number $N_{i,j}$ of such particle clusters present in each vector cell (used in the Eulerian solution of the flow field) is calculated (see the schematic in Fig. 3.6). Thus, in the discretized form of momentum equation, the particle number density in the computational cell (i,j) is evaluated as

$$\Lambda_{i,j} = \frac{N_c N_{i.j}}{\Delta x_i \Delta y_j}. \qquad \textbf{…..(3.17)}$$

Once the total reaction of drag force in a vector cell (i,j) is calculated by summing the drag forces on all the particles residing in the cell, the fluid phase is solved again to account for the

particle-to-fluid interaction. Particle tracking is done once again in the modified flow field. The iterative process of solving the fluid and dispersed phases continues until the largest difference in the magnitude of drag forces at each cell computed in two successive iterations falls below a preset convergence criterion.

A non-uniform Cartesian mesh system with hyperbolic size distribution is deployed. The grid clustering ratio and mesh size are chosen adequately to resolve the sharp velocity gradients near the walls and close to the location of the magnetic dipole where particle velocity becomes large.

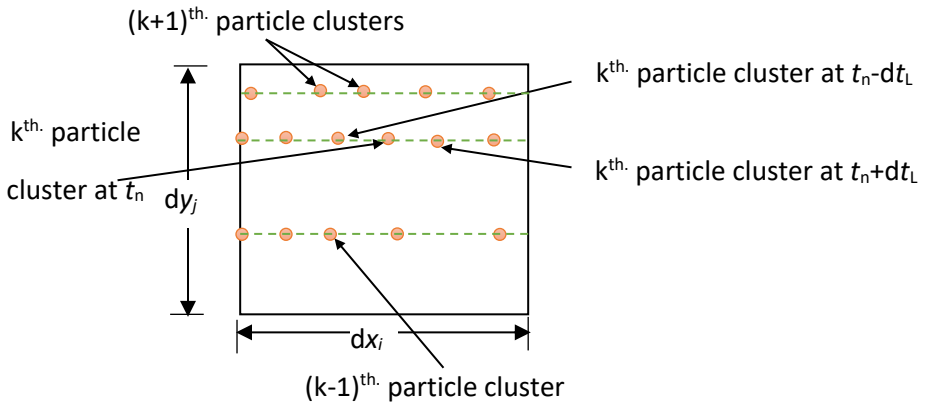

Fig. 3.6: Basis of computing Λ (particle number density). Total number $N_{i,j}$ of particle clusters residing in the $(i, j)^{th.}$cell can be computed by Lagrangian tracking of all the particle clusters. After knowing the value of $N_{i,j}$, Λ can be calculated from Eq. (3.17).

3.4.1 Solution Methodology

The governing equations are solved using explicit finite difference technique in the SOLA method of incompressible fluid flow solution. The algorithm of solution is as follows:

(i) The entire data of the physical dimensions of the computational area and the input conditions (e.g. inlet fluid flow, fluid properties, particle flow rate, and particle properties) are specified.

(ii) The numerical mesh is generated and the variables are initialized.

(iii) Following the stability and CFL criteria the time increment is computed.

(iv) The momentum conservation equations with appropriate boundary conditions are used for advancing the velocity field.

(v) The continuity equation is used for the corrections of the velocity and pressure fields.

(vi) Steps from iii to v are repeated, till the convergence of the fluid phase variables is achieved.

(vii) Solution for the particle trajectories using Lagrangian tracking and computation of the momentum exchange between the phases is carried out.

(viii) Solution of Lagrangian particle phase and Eulerian liquid phase in sequence are repeated, with updating the interphase source terms till convergence is achieved.

3.4.2 Discretization Scheme

The explicit finite differencing technique is used for discretizing the transient transport equations. The fluid properties such as density, viscosity is calculated at the cell faces by linear interpolation between the corresponding property values at the adjacent cell centers (as shown in Fig. 3.7). The source term is considered to be constant throughout the volume of each cell. The discretized form of continuity and momentum equation for the control volume around $u_{i,j}$ can be expressed as:

Continuity equation:

$$\frac{u_{i,j} - u_{i-1,j}}{dx_s(i)} + \frac{v_{i,j} - v_{i,j-1}}{dy_s(j)} = 0 \qquad \textbf{…..(3.18)}$$

U-momentum equation:

$$\frac{u_{i,j}^{n+1}-u_{i,j}^{n}}{\Delta t}+\frac{\left[\left(\frac{\left(u_{i+1,j}^{n}+u_{i,j}^{n}\right)^{2}}{2}\right)-\left(\frac{\left(u_{i,j}^{n}+u_{i-1,j}^{n}\right)^{2}}{2}\right)\right]}{dx_v(i)}+\frac{\left[\left[\left(\frac{u_{i,j+1}^{n}\frac{dy_s(j)}{2}+u_{i,j}^{n}\frac{dy_s(j+1)}{2}}{dy_v(j)}\right)\times\left(\frac{v_{i+1,j}^{n}\frac{dx_s(i+1)}{2}+v_{i,j}^{n}\frac{dx_s(i)}{2}}{dx_v(i)}\right)\right]-\left[\left(\frac{u_{i,j}^{n}\frac{dy_s(j-1)}{2}+u_{i,j-1}^{n}\frac{dy_s(j)}{2}}{dy_v(j-1)}\right)\times\left(\frac{v_{i+1,j-1}^{n}\frac{dx_s(i+1)}{2}+v_{i,j-1}^{n}\frac{dx_s(i)}{2}}{dx_v(i)}\right)\right]\right]}{dy_s(j)}=$$

$$-\frac{1}{\rho}\frac{p_{i+1,j}^{n}-p_{i,j}^{n}}{dx_v(i)}+\nu\left[\frac{\left(\frac{u_{i+1,j}^{n}-u_{i,j}^{n}}{dx_s(i+1)}\right)-\left(\frac{u_{i,j}^{n}-u_{i-1,j}^{n}}{dx_s(i)}\right)}{dx_v(i)}+\frac{\left(\frac{u_{i,j+1}^{n}-u_{i,j}^{n}}{dy_v(j)}\right)-\left(\frac{u_{i,j}^{n}-u_{i,j-1}^{n}}{dy_v(j-1)}\right)}{dy_s(j)}\right] \qquad \textbf{.....(3.19)}$$

V-momentum equation:

$$\frac{v_{i,j}^{n+1}-v_{i,j}^{n}}{\Delta t}+\frac{\left[\left(\frac{\left(v_{i,j+1}^{n}+v_{i,j}^{n}\right)^{2}}{2}\right)-\left(\frac{\left(v_{i,j}^{n}+v_{i,j-1}^{n}\right)^{2}}{2}\right)\right]}{dy_v(j)}+\left[\frac{\left[\left(\frac{u_{i,j+1}^{n}\frac{dy_s(j+1)}{2}+u_{i,j}^{n}\frac{dy_s(j)}{2}}{dy_v(j)}\right)\times\left(\frac{v_{i+1,j}^{n}\frac{dx_s(i)}{2}+v_{i,j}^{n}\frac{dx_s(i+1)}{2}}{dx_v(i)}\right)\right]-\left[\left(\frac{u_{i-1,j+1}^{n}\frac{dy_s(j+1)}{2}+u_{i-1,j}^{n}\frac{dy_s(j)}{2}}{dy_v(j)}\right)\times\left(\frac{v_{i,j}^{n}\frac{dx_s(i-1)}{2}+v_{i-1,j}^{n}\frac{dx_s(i)}{2}}{dx_v(i-1)}\right)\right]}{dx_s(i)}\right]=$$

$$-\frac{1}{\rho}\frac{p_{i,j+1}^{n}-p_{i,j}^{n}}{dy_v(j)}+\nu\left[\frac{\left(\frac{v_{i+1,j}^{n}-v_{i,j}^{n}}{dx_v(i)}\right)-\left(\frac{v_{i,j}^{n}-v_{i-1,j}^{n}}{dx_v(i-1)}\right)}{dx_s(i)}+\frac{\left(\frac{v_{i,j+1}^{n}-v_{i,j}^{n}}{dy_s(j+1)}\right)-\left(\frac{v_{i,j}^{n}-v_{i,j-1}^{n}}{dy_s(j)}\right)}{dy_v(j)}\right] \qquad \textbf{…..(3.20)}$$

The above equations can be directly used for the evolution of $u_{i,j}^{n+1}$, and $v_{i,j}^{n+1}$ provided the other variables in the discretized equations are at nth time level. This excludes the pressure terms in the equation, which should be at (n+1)th time level. In absence of pressure terms at (n+1)th time step, it is required to use the pressure terms of the nth time level to solve the velocity. But, as the velocity and pressure at the same time level are to correspond, the solution with the pressure of the previous time level only yields a provisional or approximate value of the velocity ($\tilde{u}_{i,j}^{n+1}$). Therefore,

$$\frac{\partial u}{\partial t}+[\text{CONVX+CONVY}]=-\frac{1}{\rho}\frac{\partial P}{\partial X}[\text{DIFFX+DIFFY}]$$

$$\frac{\tilde{u}_{i,j}^{n+1}-u_{i,j}^{n}}{\Delta t}=-\frac{1}{\rho}\frac{p_{i+1,j}^{n}-p_{i,j}^{n}}{dx_v(i)}+[\text{DIFFX+DIFFY}]^{n}-[\text{CONVX+CONVY}]^{n}$$

$$\tilde{u}_{i,j}^{n+1} = u_{i,j}^{n} - \Delta t \frac{1}{\rho} \frac{p_{i+1,j}^{n} - p_{i,j}^{n}}{dx_v(i)} + \Delta t \ [\text{DIFFX+DIFFY}]^n - \Delta t \ [\text{CONVX+CONVY}]^n \quad \textbf{....(3.21)}$$

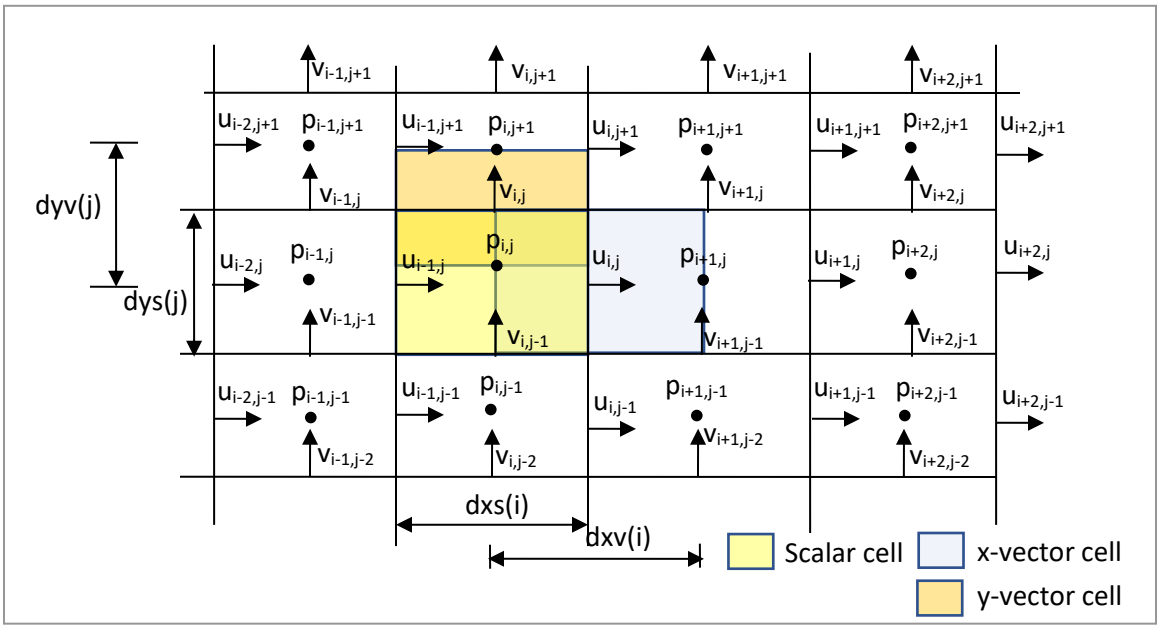

Fig. 3.7 Shows the velocity and pressure at the cell faces and centers respectively.

The continuity and momentum equations are solved for the time (t_n+δt) by explicit method, using the estimate of the pressure, velocity over the computational domain at the n^{th} time-step, t_n. While the x- and y-momentum equations allow for updating the values of u and v with time, the pressure p cannot be updated through time-marching, as the continuity equation does not have a transient term for the incompressible flow. The resulting velocity field for the advanced time (t_n+ δt) does not, for obvious reason, satisfy the continuity equation, since the pressure field assumed in the momentum equations is not correct. The required pressure correction could only be done through the continuity equation, which did not contain any pressure term. The pressure correction needs to be done iteratively by imposing the constrain of the zero-mass divergence. For each cell, the mass divergence

$$\Delta_{i,j} = \frac{\Delta t}{\beta\rho}\left[\frac{1}{dx_v(i)dx_s(i)} + \frac{1}{dx_v(i)dx_s(i-1)} + \frac{1}{dy_v(j)dy_s(j)} + \frac{1}{dy_v(j)dy_s(j-1)}\right]\delta p_{i,j} \quad \textbf{.....(3.22)}$$

is computed using the most recently corrected values of the velocities. The pressure correction,

$$\delta p_{i,j} = \frac{\beta \Delta_{i,j}}{\frac{\Delta t}{\rho}\left[\frac{1}{dx_v(i)dx_s(i)} + \frac{1}{dx_v(i)dx_s(i-1)} + \frac{1}{dy_v(j)dy_s(j)} + \frac{1}{dy_v(j)dy_s(j\text{-}1)}\right]}, \quad \textbf{…..(3.23)}$$

required to set the absolute value of $\Delta_{i,j}$ below a small pre-assigned number (.001 in this case), which is calculated from the equation where, β is an over-relaxation factor that was used to accelerate the convergence. The value of β can vary between 1.0 and 2.0, however a value around 1.8 is recommended for better convergence.

The change in pressure within a cell is used to correct the associated *x*-velocity components at the scalar cell faces as follows:

$$u_{i,j} = \tilde{u}_{i,j} + \frac{\Delta t}{\rho dx_v(i)}\left[p_{i,j} - \tilde{p}_{i,j}\right] = \tilde{u}_{i,j} + \frac{\Delta t}{\rho dx_v(i)}\delta p_{i,j} \quad \textbf{…..(3.24)}$$

$$u_{i-1} = \tilde{u}_{i-1,j} - \frac{\Delta t}{\rho dx_v(i\text{-}1)}[p_{i,j} - \tilde{p}_{i,j}] = \tilde{u}_{i-1,j} - \frac{\Delta t}{\rho dx_v(i\text{-}1)}\delta p_{i,j} \quad \textbf{…..(3.25)}$$

Where the symbol ~ denotes the incorrect field variable.

Similarly, for the *v*-velocities we can get the relationship between the correct and provisional values in terms of the pressure correction term as:

$$v_{i,j} = \tilde{v}_{i,j} + \frac{\Delta t}{\rho dy_v(j)}\delta p_{i,j} \quad \text{and} \quad v_{i,j-1} = \tilde{v}_{i,j-1} - \frac{\Delta t}{\rho dy_v(j-1)}\delta p_{i,j} \quad \textbf{…..(3.26)}$$

The cell pressure is also corrected as

$$p_{i,j} = \tilde{p}_{i.j} + \delta p_{i,j}$$

Once the entire flow at the $t_n+\delta t$ time-step is made to satisfy the mass continuity equation, and a correct pressure field is obtained, these values of velocity and pressure are used again to solve the field variables for the next time-step. Thus, the solution is made to proceed in time until

the ratio $\frac{\left|(\text{variable})^{n+1}-(\text{variable})^{n}\right|}{\delta t}$ for all the field variables fall below the preset convergence criteria.

The time increment has to be chosen correctly in order to have numerical stability in the solution since the method implements an explicit finite difference technique. The time increment is governed by two limitations: namely the Courant-Friedrichs-Lowy (CFL) condition and the restriction on the basis of grid Fourier number.

According to the CFL criteria, the fluid elements cannot move more than one cell in either direction in one-time increment. Therefore, the time increment must satisfy the condition for governing equation and species concentration equation.

$$\Delta t \langle \min\left[\frac{1}{2v\left\{\frac{1}{dx_s(i)^2}+\frac{1}{dy_s(j)^2}\right\}}, \frac{dx_v(i)}{u_{i,j}}, \frac{dy_v}{u_{i,j}}\right] \quad \text{and} \qquad \textbf{…..(3.27)}$$

$$\Delta tsp \langle \min\left[\frac{1}{2D\left\{\frac{1}{dx_s(i)^2}+\frac{1}{dy_s(j)^2}\right\}}, \frac{dx_v(i)}{u_{i,j}}, \frac{dy_v(j)}{v_{i,j}}\right] \text{ for all i, j.} \qquad \textbf{…..(3.28)}$$

Typically, the time increment is chosen as to be one third to one fourth of the minimum cell transit time. However, under cases where there are additional source terms in the equation, the time increment may have to be further reduced.

3.4.3 Grid independence test

The numerical results have been tested for their independence of the grid sizes that have been selected for discretization of the governing equations. A non-uniform grid (shown in Fig. 3.8), based on a hyperbolic mesh size distribution, is used to resolve the sharp gradients near the

walls and close to the location of the magnetic dipole. Simulations are performed with different mesh sizes to obtain grid independent results for both the fluid flow and the particle trajectories.

The following grid distributions have been chosen for the different configurations, based on the grid independence test as shown in Fig. 3.8. Following a grid independence study, a 150×90 mesh configuration is chosen for the present simulations.

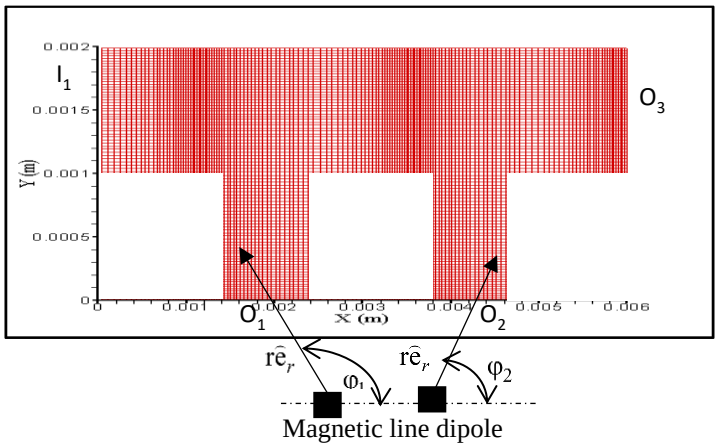

(a)

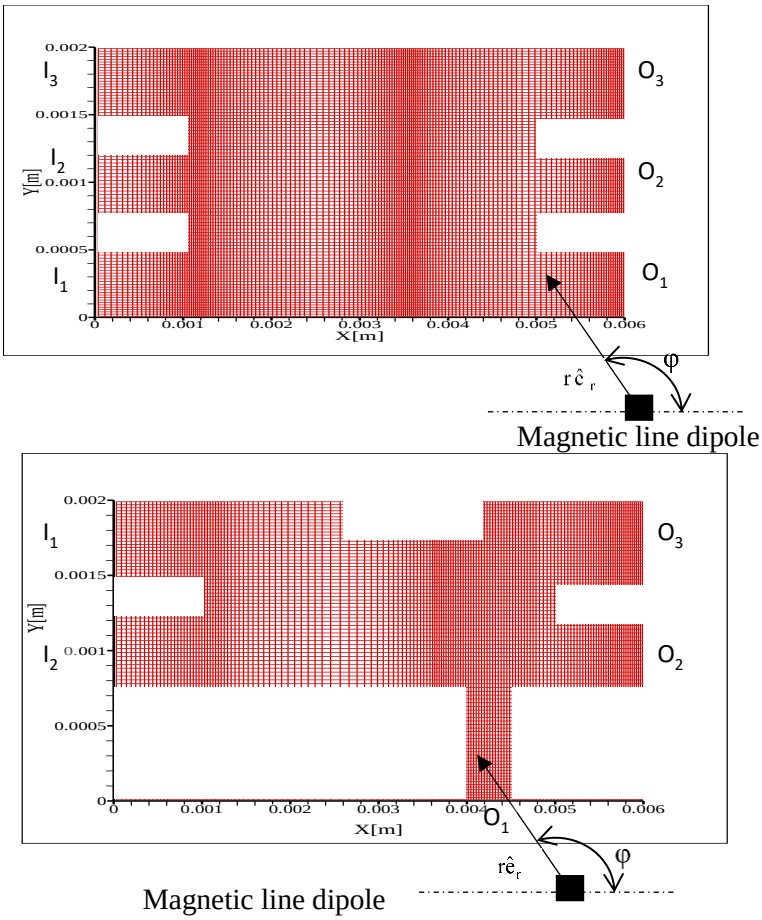

Fig. 3.8: Grid structure for the flow simulations for the (a) FFF, (b) SPLITT and (c) hybrid free flow magnetophoretic devices.

3.4.4 Solution Steps

The numerical code is executed in the following sequence.

(i) All the data related to the physical dimensions of the computational domain, the inlet fluid flow, the inlet fluid properties, the inlet particle cluster flow, the inlet particle properties and convergence criteria are fed into the code.

(ii) The numerical mesh in the channels are then set up and the variables are initialized.

(iii) The time increment for the $(n+1)^{th}$ time-step, δt, is computed following the stability criteria as described earlier.

(iv) The discretized continuity and momentum conservation equations are then solved to obtain the corresponding field variable at the $(n+1)^{th}$ time step, using the field variables and fluid properties obtained at the n^{th} time step and appropriate boundary conditions.

(v) The velocity and pressure fields are corrected through the continuity equation.

(vi) The particle trajectories are subsequently solved.

(vii) The gradients of field variables (velocity, concentration) are computed to check the convergence.

(viii) The properties values are calculated for the increased time step.

(ix) The time step is advanced as in (iii) and step (iv) onwards are repeated.

(x) At suitable intervals of time, the field variables are sorted in output files.

(xi) The entire procedure is continued iteratively until a steady state converged solution is obtained.

(xii) Finally, the flow velocity, particle velocity, particle tracking, electromagnetic force and field are calculated at the steady state.

3.5 Validation

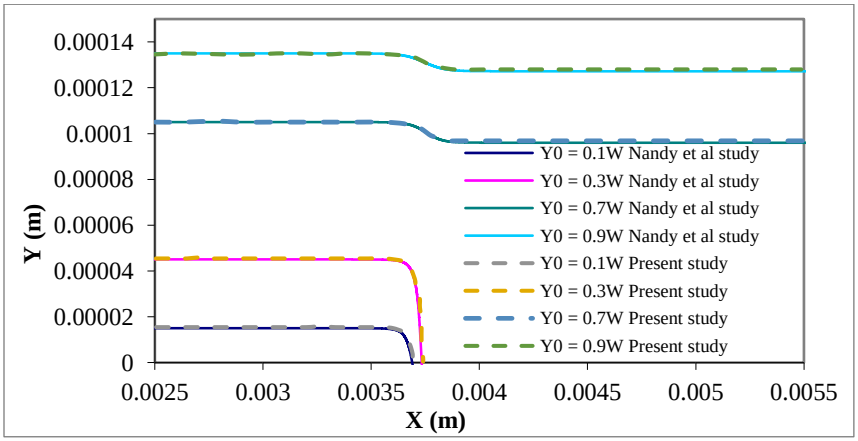

Fig. 3.9 Particle trajectories from different initial positions (x_0, y_0) mapped from the present numerical code (dashed line) and the analytical results (continuous line) obtained by Nandy et al. [8].

Particle trajectories are mapped using the present code and compared with the particle trajectories obtained by Nandy et al.[8] (as shown in Fig. 3.9) for validating the numerical code. For comparing the particle trajectory results, operating parameters were considered following Nandy et al. [8] (a = 1 μm, χ_{eff} = 1.0, μ = 8.9 × 10^{-4} Pa-s, u_0 = 0.01 m/s, W = 150 μm, L = 0.0055 m, X_{mag} = 3.75 mm, Y_{mag} = -0.00003 mm). Nandy et al.[8] assumed a fully developed flow profile in their study, and a one-way particle–fluid interaction. For comparing the particle trajectory results, a fully developed velocity profile with a very dilute particle loading (N_{part} = 10 $m^{-2}s^{-1}$) at the inlet is assumed for the study. Figure 3.9 shows the comparison of four particle clusters trajectories which are released from y = 0.1W, 0.3W, 0.7W and 0.9W. Figure confirms that the particle trajectory of the present simulation well matches with the study of Nandy et al.[8].

Chapter four: Results and Discussions

4.1 Background

Particle trajectory and their capture in SPLITT fractionation device is first discussed, followed by a comparison between the SPLITT and FFF for a given range of operating parameters. Finally, a hybrid and free flow magnetophoretic devices are also characterized numerically for prescribing the optimum operating regime. The following section of the chapter discusses in details about the particle trajectories and their capture efficiency and separation index values obtained from simulations carried out under different devices for under externally applied magnetic field.

4.2 Operating regime for the Split flow thin (SPLITT) fractionation device

4.2.1 Flow field

Particle trajectory in the SPLITT device is a strong function of the velocity distribution of the fluid and hence the flow profile within the microfluidic separator is first investigated. Because of the mutual particle-fluid momentum coupling (through the fluid drag and its reaction), the flow is expected to be influenced by not only the pressure gradient (which causes the flow), but also the magnetophoretic mobility of the particle and the imposed magnetic field. The salient operating parameters that can influence the particle trajectory are the magnetic dipole strength (P), particle diameter (a) and magnetic susceptibility (χ), fluid viscosity (μ) and flow velocity (U_{av}). A base case is chosen initially to represent a sample description of particle transport and separation (see Table 4.1); subsequently the device performance is also analyzed

over a wider range of the operating parameters (see Table 4.1) to arrive at the optimal operating conditions.

Table 4.1: Base values and ranges of variation of operating parameters for the study of particles trajectory

Parameters	Base value (unit)	Ranges of variation (unit)
L	0.006 m	Not varied
W	0.002 m	Not varied
ρ	1000 kg/m^3	Not varied
U_{av}	0.0106 m/s	0.004–0.1 m/s
μ	0.001Pa-s	0.0003-0.0036 (Pa-s)
a_1	2 µm	0.5–3.0 µm
a_2	1.3 µm	0.2–1.9 µm
$\chi_{eff,1}$ *and* $\chi_{eff,2}$	0.1	0.025-0.25
P	4 Am	0.2–6.6 Am

The dipole position is X_{mag}= 6 mm, Y_{mag}= −1.5 mm (i.e., at 1.5 mm below the bottom wall) for all the cases studied. Figure 4.1 (a) describes the velocity profile of fluid at base values for different parameters. Axial variations of velocity magnitude throughout the channel along three imaginary lines AA′, BB′ and CC′, passing through *y = 0.25, 1.0 and 1.75* mm (i.e., along the mid-planes of $I_1 – O_1$, $I_2 – O_2$ and $I_3 – O_3$, respectively) are reported in Fig 4.1(b). Figure 4.1(a) shows that the fluid streams entering through the three inlets with plug profiles morph into fully developed profiles within a length of x = 0.7 mm. The mid-plane velocities of the three inlet streams assume a maximum value of ~0.016 m/s at a location of x = 0.7 mm. Beyond x = 1 mm, the three streams mix; the velocity is reduced due to increased flow area (as the inlet splitter plates IS_1 and IS_2 are no longer present). Streams entering through I_1 and I_3 are found to focus towards the central stream (Fig. 4.1(a)), leading to increased flow velocity along the central stream (I_2-O_2). This is corroborated by the axial variation of velocities in Fig. 4.1(b);

the velocities along the lines AA′ and CC′ are found to dip in the common flow area to a minimum value of ≈ 0.0055 m/s, while that along BB′ increases to a maximum value of 0.012 m/s. The downward deflection of the stream I_3 is particularly significant for the particle trajectories. It is intuitive that the particles (released from I_3) would move in a downward direction - thus experiencing greater magnetic force that helps in their transverse transport.

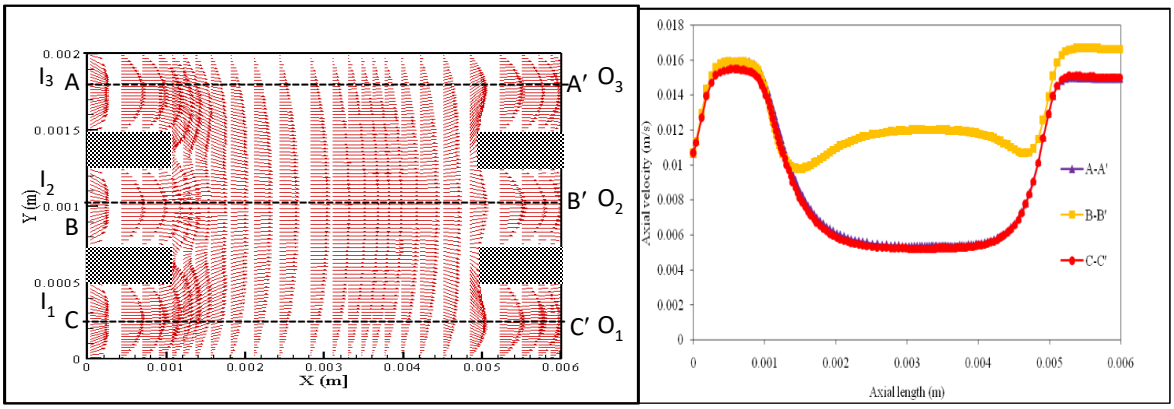

(a) (b)

Fig. 4.1 (a) Host fluid velocity profile, and (b) the axial variation of axial velocity throughout the channel along AA′, BB′, and CC′ for the base case operation (see Table 4.1).

Velocity field in the early part of the separator section (1 mm ≤ x ≤ 2.5 mm) gradually approaches parallel flow producing a nearly parabolic axial velocity profile at x = 3 mm. Beyond x = 4.0 mm, velocity profile again changes at the upstream of the outlet splitter plates OS_1 and OS_2 where the influence of flow splitting in the three outlets begins to generate transverse velocity components. Because of the wall shear in the separator section, a larger fraction of the flow takes place through the middle section of the channel; average flow velocity at the upstream ends of O_1 and O_3 are therefore smaller than that ahead of O_2, and the outflow through O_2 exceeds the outflow through O_1 or O_3. Fig. 4.1(b) clearly indicates that the peak velocity at the mid-plane of O_2 (0.0166 m/s) is higher than the same at O_1 and O_3 (0.01495

m/s for each). This also explains the fact that despite having the same flow rates at the three inlets (average flow velocity in each of them is 0.0106 m/s), the flow rates at the outlets differ.

4.2.2 Particle Trajectory

Figure 4.2 shows the simulated trajectories of 100 large (radii a_1 = 2 µm, denoted by red lines) and 100 small (radii a_2 = 1.3 µm, green lines) magnetic particle clusters that are released uniformly from the inlet I_3 (i.e., $0.0015 \leq y \leq 0.002$ m) through SPLITT flow devices for the base operating parameters (see Table 4.1). The number of particles in each cluster is so chosen that a particle influx rate for each type particle is maintained as 5×10^5 $m^{-2}s^{-1}$. From the particle trajectories in Fig. 4.2 it is observed that the outlet O_1 captures 68 large particle clusters (along with 4 small particles clusters) while the O_2 captures 68 small particles clusters (with 9 large particles clusters mingled with it). The remaining clusters of large particles are trapped on the outlet splitter wall OS_1 intervening O_1 and O_2, and small ones collect at the upper wall of OS_2.

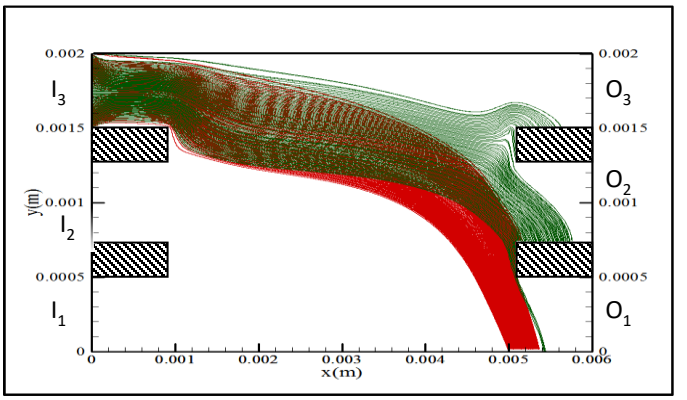

Fig. 4.2 Particle trajectories in the magnetophoretic SPLITT device for the base case as shown in Table 4.1.

The larger particles experience higher magnetophoretic velocity than the smaller particles do. General trend of the particle trajectories indicates that initially, when the particles are far away from the dipole, they tend to move along the flow streamlines as the fluid drag dominates over

the magnetic force. But as the particles are advected towards the outlets, magnetic force becomes dominant over the drag force. Due to the difference in magnetophoretic mobility of the two types of particle clusters, they develop different transverse velocities. This coupled with the axial velocity of the flow and relative positions of the outlets segregate the particle clusters into outlet different regions of the flow.

4.2.3 Capture Efficiency and Separation Index

Having mapped the flow field and particle trajectories in the separator, the performance of the device is evaluated under the base operating condition. The performance parameters are defined following the target objective of the device, which is to separate the two different particle clusters in the streams flowing through their designated outlets. For a given combination of different operating parameters (e.g., P, a, U_{av}, χ_{eff}, and μ), not every particle entering the microchannel escape through the designated outlets. For example, it can be counted from Fig. 4.2 that 68 of the 100 particle clusters of larger mobility are collected at the (either trapped in the wall of or flowing out through) outlet O_1 while 68 of the 100 smaller clusters are collected at (trapped or flowing out through) the outlet O_2. It is worth noting that the collection of particles on the left (vertical) faces of the outlet splitters and on the channel wall at the upstream of the outlet splitters (i.e., $x < 5.1$ mm) are not accounted in computing the performance parameters. Therefore, the efficacy of the device in separating a fraction of the incoming particles at the designated outlet is quantified in terms of Capture Efficiency (CE), which is defined as,

$$CE_1 = \frac{\text{Number of particle clusters of larger mobility collected at } O_1}{\text{Number of particle clusters of larger mobility entering the separator}} \text{ and} \qquad \textbf{…..(4.1)}$$

$$CE_2 = \frac{\text{Number of particle clusters of smaller mobility collected at } O_2}{\text{Number of particle clusters of smaller mobility entering the separator}}$$

In the above metric, the SPLITT device (Fig. 4.2) records CE_1 = 68% and CE_2 = 68%. However, the overall device performance is not reflected in the *CE* figures alone. It may be noticed that the outlet O_1 collects 4 clusters of smaller magnetophoretic mobility, besides the 68 clusters of larger mobility. Same situation arises for the outlet O_2, where 9 clusters of larger mobility are also mixed with the 68 clusters of smaller mobility. Therefore, the extent (or purity) of separation is not perfect (i.e., 100%) at both the outlets. The purity of separation is, therefore, best quantified by separation index (*SI*) at both the outlets, defined as:

$$SI_1 = \frac{\text{Number of captured particle clusters of larger mobility collected at } O_1}{\text{Total number of particle clusters collected at } O_1}, \text{ and} \qquad \textbf{…..(4.2)}$$

$$SI_2 = \frac{\text{Number of captured particle clusters of smaller mobility collected at } O_2}{\text{Total number of particle clusters collected at } O_2}$$

Therefore, it ensues from Fig. 4.2 that the two outlets of the SPLITT device record separation indices of SI_1 = 94% and SI_2 = 88%.

4.2.3.1 Effects of operating parameters on *CE*

It has been shown before [108] that the particle trajectories depend on the operating parameters e.g., the dipole strength, particle size and susceptibility, fluid viscosity and velocity. Hence, the capture efficiency and separation index are also expected to be functions of these operating parameters [108]. The trajectory of magnetophoretic motion of a particle in the pressure-driven flow ensues from a competition between the drag force ($\mathbf{F}_d \sim 6\pi a\mu U_{av}$) and the magnetic force ($\mathbf{F}_m \sim 4/3\pi a^3 \chi_{eff} P^2$) [8]. Intuitively, the ratio of magnetic force to drag force, represented by a group variable $\Pi = (a^2 \chi P^2/\mu U_{av})$, is expected to influence the capture efficiency and separation index of the device. Figure 4.3 shows the variations of CE_1 and CE_2 as functions of $\Pi_1 = (a^2 \chi_{eff,1} P^2/\mu U_{av})$ and $\Pi_2 = (a^2 \chi_{eff,2} P^2/\mu U_{av})$, respectively. Every parameter of the two group variables have been changed individually within the parametric range shown in Table 4.1,

keeping all others parameters constant at their base values. All the points in the plots showing variations of CE_1 with Π_1 (Fig. 4.3(a)) and CE_2 with Π_2 (Fig. 4.3(b)), obtained by varying each of the parameters P, χ, a, μ and U_{av}, are found to merge with each other. Figure 4.3(a) shows that CE_1 remains nearly zero until Π_1 exceeds a threshold value of 1.4×10^{-7} A^2m^5/N, when the lowermost particles (cluster) of larger magnetophoretic mobility gets marginally captured at the outlet O_1. For $\Pi_1 > 1.4\times10^{-7}$ A^2m^5/N (i.e., for an increased P, a or χ_{eff} or decreased μ or U_{av}) a greater magnetic influence on the particles causes a greater number of clusters of larger mobility to collect at O_1 (see Fig. 4.3(a)). The base case (corresponding to the operating parameters described in Table 4.1) corresponds to $\Pi_1 = 4.0\times10^{-7}$ A^2m^5/N for which $CE_1 = 68\%$ was observed. This increasing trend continues until CE_1 shows a maximum (73%) at $\Pi_1 = 4.4\times10^{-7}$ A^2m^5/N (denoted as $\Pi_{1,peak}$ in Fig. 4.3(a)). Beyond $\Pi_{1,peak}$, more and more particles get trapped on the lower wall of the separator ahead of the outlet O_1 due to the increased magnetic attraction. This progressively reduces the number of particle clusters that are collected at the outlet O_1. Finally, the CE_1 value drops down to zero beyond $\Pi_1 = 9.6\times10^{-7}$ A^2m^5/N, when none of the clusters of larger magnetophoretic mobility are collected at O_1.

Likewise, CE_2 also exhibits an increasing trend at low Π_2 values (see Fig. 4.3(b)), peaking at $\Pi_2 = 1.53\times10^{-7}$ A^2m^5/N (denoted in Fig. 4.3(b) as $\Pi_{2,peak}$), and then declining at higher Π_2. For the particle clusters of lower mobility, the collection port (O_2) is located closer to the original particle stream. Therefore, the CE_2 peak is observed at a lower value of Π_2 (than the Π_1 for the CE_1 peak). Beyond $\Pi_{2,peak}$, the value of CE_2 decreases monotonically, since the magnetic force in this regime overwhelms the fluid drag, pulling a larger number of the particle clusters below O_2, so that they are either collected at O_1 or on the lower wall. The base case of operating parameters (see Table 4.1) corresponds to $\Pi_2 = 1.69\times10^{-7}$ A^2m^5/N falls in this regime. Finally,

beyond $\Pi_2 \approx 4.6\times10^{-7}$ A^2m^5/N, CE_2 drops down to zero, when none of the smaller particles is collected at O_2. It is evident from Fig. 4.3 that one would prefer to operate the device such that the Π_1 and Π_2 values are close to their optimum values that produce the highest CE_1 and CE_2. From Fig. 4.3 it is apparent that the ratio ($\Pi_{1,peak} / \Pi_{2,peak}$) is approximately 2.86, while that chosen as the base case (Table 4.1) is approximately 2.36.

While the operating ranges of both the group variables Π_1 and Π_2 can be simultaneously controlled by altering P, μ or U_{av}, the ratio Π_1 / Π_2 (= r_m) can be tuned close to the optimum value ($\Pi_{1,peak} / \Pi_{2,peak}$) by suitable choice of the individual properties of the particles (i.e., particle diameter and effective susceptibilities). It implies that by varying the particle properties (i.e., a and χ_{eff}) in a selective manner their relative mobilities are so influenced that r_m attains the optimum value $\Pi_{1,peak}/ \Pi_{2,peak}$. These two properties can be grouped as

$$\beta^* = a^2 \chi_{eff}, \qquad \textbf{…..(4.3)}$$

for a particular particle type.

The other three variables in the definition of Π (i.e., P, μ and U_{av}) has been separately clubbed together as

$$\gamma = P^2/ (\mu U_{av}), \qquad \textbf{…..(4.4)}$$

such that,

$$\Pi_1 = \gamma\beta^*_1, \text{ and } \Pi_2 = \gamma\beta^*_2. \qquad \textbf{…..(4.5)}$$

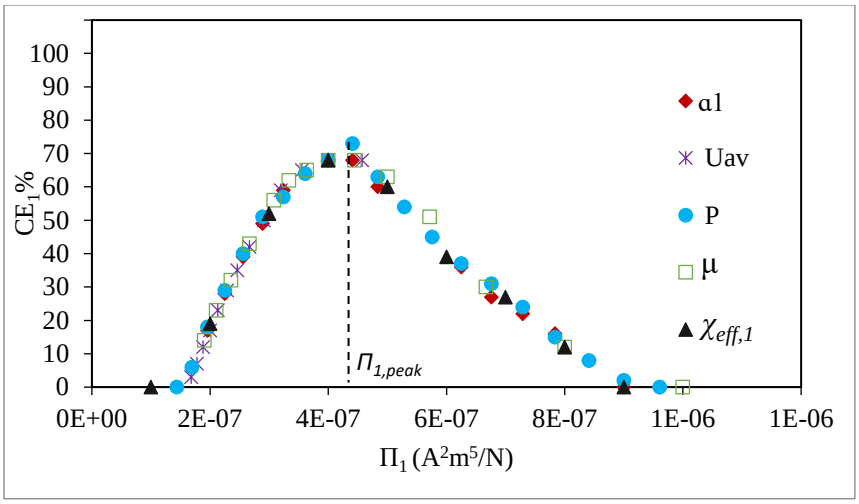

(a)

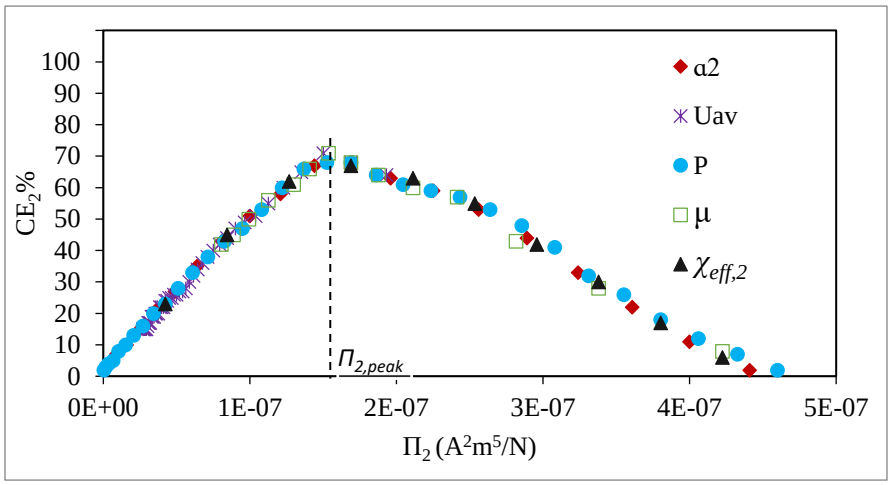

(b)

Fig. 4.3 Particle capture efficiencies (a) CE_1 as a function of Π_1 $(a_1^2\chi_{eff,1}P^2)/(\mu U_{av})$ and (b) CE_2 as a function of Π_2 $(a_2^2\chi_{eff,2}P^2)/(\mu U_{av})$ for the SPLITT device. Results show that all the parametric plots collapse on a single curve, representing how CE values depend upon different parameters (dipole strength P, magnetic susceptibility χ, particle size a, fluid viscosity μ and fluid velocity U_{av}).

4.2.3.2 Effects of operating parameters on *SI*

It may be worth noticing that the capture efficiency of a particle type depends solely on how the operating parameters influence the trajectory of the specific particle type. However, the separation index for a particular particle type would also depend on the trajectories of the other particle type. Figures 4.4(a) and (b) show the variations in the separation indices for the two

types of particle clusters plotted as functions of the group variables Π_1 and Π_2, respectively. Unlike the plots for the *CE*s, the *SI* vs Π plots do not collapse on single curve for variation of all the five parameters. However, the *SI* vs Π plots obtained by varying the constituent parameters of γ nearly merge (see Figs. 4.4(a) and (b)). Figure 4.4(a) shows that for $1.68\times 10^{-7} < \Pi_1 < 3.64\times10^{-7}$ A^2m^5/N (with β^*_1 and β^*_2 corresponding to the base values described in Table 4.1), only the particles with larger mobility would reach the outlet O_1 leading to SI_1 = 100%. At larger values of Π_1, attributed either to an increased P or a decreased U_{av} or μ, SI_1 decreases monotonically due to the premature capture of the larger-mobility particle clusters before their designated outlet. This is also aggravated by the unwanted carry-over of the lower-mobility particles in O_1 (see inset (C1) of Fig. 4.4(a)).

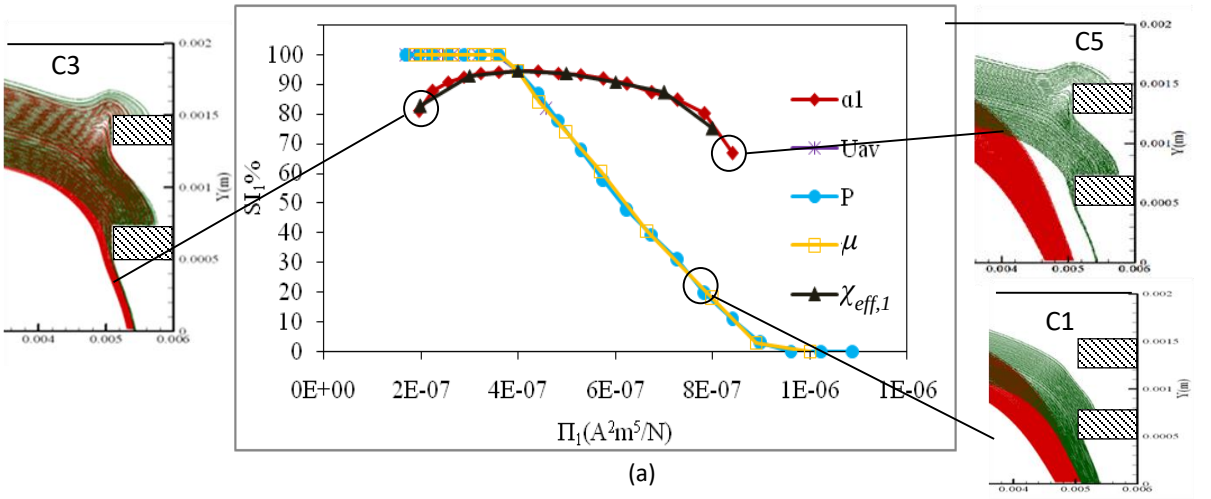

(a)

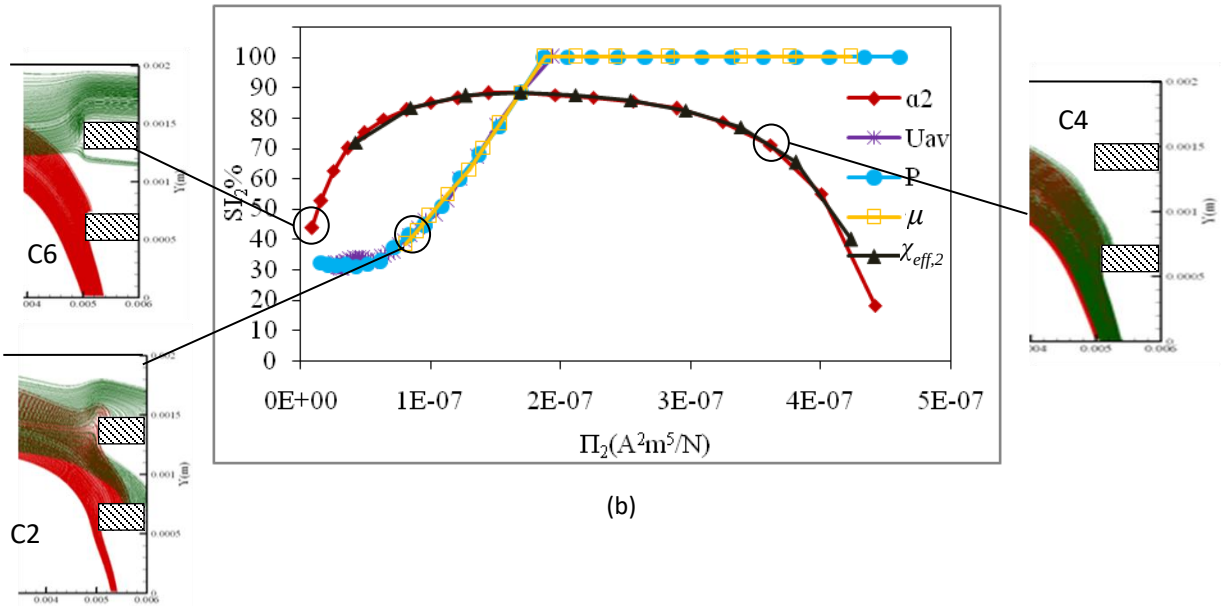

Fig. 4.4 Particle separation indices (a) SI_1 as a function of Π_1 ($=\beta^*_1\gamma$) and (b) SI_2 as a function of Π_2 ($=\beta^*_2\gamma$). *SI* plots are segregated nearly to two basic trends: one for the constant β^* (i.e., varying γ) case and the other for constant γ (i.e., varying β^*) case. Here, $\beta^* = a^2\chi_{eff}$ and $\gamma = P^2/(\mu U_{av})$.

For the particles of lower mobility, Fig. 4.4(b) show that the SI_2 value is initially low due to partial carryover of the higher-mobility particles at O_2 (see inset (C2) of Fig. 4.4(b) for the corresponding particle trajectories). At larger Π_2 values, the unwanted carry-over of larger mobility particles to the outlet O_2 decreases (as more of them are diverted to O_1), while the capture of smaller-mobility particles at O_1 goes up (resulting in a decline of SI_1). Beyond $\Pi_2 = 1.88\times10^{-7}$ A^2m^5/N, no larger-mobility particle enters the outlet O_2 and the $SI_2 = 100\%$ persists at the highest range of Π_2 considered for the study. The situation differs when the particle property parameter β^*, i.e., a and χ_{eff} are varied selectively. For example, an increase of a_1 or $\chi_{eff,1}$ leads to an increase of Π_1 over its base value but at the same time the corresponding Π_2 remains at its base value; thus it increases the r_m. Therefore, the plots of SI_1 vs Π_1 (Fig. 4.4(a)) with varying a_1 and $\chi_{eff,1}$ (while keeping the other parameters constant at their base values) differ from the previous three plots (obtained by varying P, μ or U_{av}). The same trend is

observed for the SI_2 vs Π_2 plots (Fig. 4.4(b)) for varying a_2 and $\chi_{eff,2}$, which differ from the corresponding plots under varying P, μ or U_{av}. Both Figs. 4.4(a) and (b) show that the SI vs Π plots nearly overlap when a and χ_{eff} are varied, giving a wide range of Π where SI values exceed 70%. On either side of this region, the SI values flag. In Fig. 4.4(a), the drooping trend of SI_1 at the lower Π_1 regime (e.g., $2\times10^{-7} < \Pi_1 < 4.0\times10^{-7}$ A^2m^5/N) can be explained from the fact that as Π_1 decreases, r_m approaches unity; as the mobility contrast between the particles diminishes, they become harder to segregate (see inset (C3) of Fig. 4.4(a) where $r_m \sim 1.18$; the corresponding CE and SI figures can be found in Table 4.2). The same effect (of decreased SI_2 with r_m approaching unity) is observed when Π_2 is on the higher side (e.g., $2.5\times10^{-7} < \Pi_2 < 4.4\times10^{-7}$ A^2m^5/N) because of increased a_2 or $\chi_{eff,2}$ (see inset (C4) of Fig. 4.4(b)). For 7×10^{-7} $A^2m^5/N < \Pi_1$ resulting from an increase of a_1 or $\chi_{eff,1}$ beyond the base value, the SI_1 drops (Fig. 4.4(a)) as fewer number of larger mobility particles are captured at O_1. Inset (C5) of Fig. 4.4(a) shows a condition where only 8 numbers of larger mobility particle clusters are captured at O_1 (the remaining are collected prematurely on the separator wall); 4 number of smaller mobility clusters (same as observed in the base case, Fig. 4.2) are still collected at the same outlet, bringing down the SI_1 from the base value (see Table 4.2). Similar situation arises for $\Pi_2 < 1.7\times10^{-7}$ A^2m^5/N in Fig. 4.4(b) (for smaller values of a_2 or $\chi_{eff,2}$); the magnetic force gets weaker such that fewer number of smaller-mobility clusters are collected at O_2 while the same (as in the base case) number of larger mobility particles are still collected alongside (see inset (C6) of Fig. 4.4(b)); this brings down the SI_2 value at the lower Π_2 regimes. Thus, while Fig. 4.3 suggests that the CE figures are best represented by the group variable Π, it is evident from Fig. 4.4 that the SI values are better represented as function of the product of the group variables γ and β^*; the SI vs Π plots clearly separate into two basic trends: one for constant β

(i.e., varying γ) and the other for constant γ (i.e., varying β^*). Both Figs. 4.3 and 4.4 serve as the basis for selection of particle properties (i.e., β^*_1 and β^*_2) and the operating parameters (i.e., γ) so as to operate the SPLITT device in the regime of best possible capture efficiencies and separation indices for both the particle types.

Table 4.2: Parameters for different insets (C1, C2, C3, C4, C5, C6) shown in Fig. 4.4 a and b.*

		C1	C2	C3	C4	C5	C6
P (A-m)		4	4	4	4	4	4
a_2 (μm)		1.3	1.3	1.3	1.9	1.3	0.3
a_1 (μm)		2	2	2	2	2.9	2
$\chi_{eff,1}$		0.1	0.1	0.05	0.1	0.1	0.1
$\chi_{eff,2}$		0.1	0.1	0.1	0.1	0.1	0.1
μ (Pa-s)		0.0005	0.0019	0.001	0.001	0.001	0.001
U_{av} (m/s)		0.01067	0.01067	0.01067	0.01067	0.01067	0.01067
Π_2 (A^2m^5/N)		3.38×10^{-7}	8.89×10^{-8}	1.69×10^{-7}	3.61×10^{-7}	1.69×10^{-7}	9.0×10^{-9}
Π_1 (A^2m^5/N)		8.0×10^{-7}	2.1×10^{-7}	2.0×10^{-7}	4.0×10^{-7}	8.4×10^{-7}	4.0×10^{-7}
r_m		2.36	2.37	1.18	1.10	5.32	44.44
O_1	N_{11}	12	23	19	68	8	80
	N_{21}	55	0	4	71	4	0
	CE_1 (%)	12	23	19	68	8	80
	SI_1	18	100	83	49	67	100
O_2	N_{12}	0	61	60	9	0	9
	N_{22}	8	45	68	22	68	7
	CE_2 (%)	8	45	68	22	68	7
	SI_2	100	42	53	71	100	44

* Note: N_{ij} = Number of $i^{th.}$ particles collected at $j^{th.}$ outlet, where i=1, and 2 denote particles with larger and smaller mobilities respectively, and j denotes the outlet (j= 1 for O_1 and j=2 for O_2)

4.2.3.3 Influence of β^* and γ on the SI

In order to identify the influence of individual group parameters β^* and γ on the separation indices under the base condition (i.e., $\Pi_1 = 4.0\times10^{-7}$ A^2m^5/N and $\Pi_2 = 1.69\times10^{-7}$ A^2m^5/N), SI_1 and SI_2 are plotted as functions of γ in Fig. 4.5. The values of β^*_1 and β^*_2 are accordingly varied (shown in the secondary x axis in Fig. 4.5) to maintain the fixed values of Π_1 and Π_2. It is evident from the plots that at small values of γ (i.e., large β^*_1 and β^*_2), the SI_1 increases and SI_2 decreases sharply with increase in γ. The separation indices assume nearly constant values (SI_1~ 94% and SI_2 ~88%) beyond $\gamma \sim 3.03\times10^5$ A^2m^3/N. Separation indices of the SPLITT device for $\gamma < 3.03\times10^5$ A^2m^3/N is vulnerable to any small deviation of the operating parameters, and therefore, should be avoided for reliable performance of the device. Also, the fact that SI_1 is greater than SI_2 for the regime of constant SI (i.e., $\gamma > 3.03\times10^5$ A^2m^3/N) has another implication: if out of the two target moieties to be separated, one demands a better purity of the separated streams, it needs to be functionalized with the magnetic particles having larger magnetophoretic mobility.

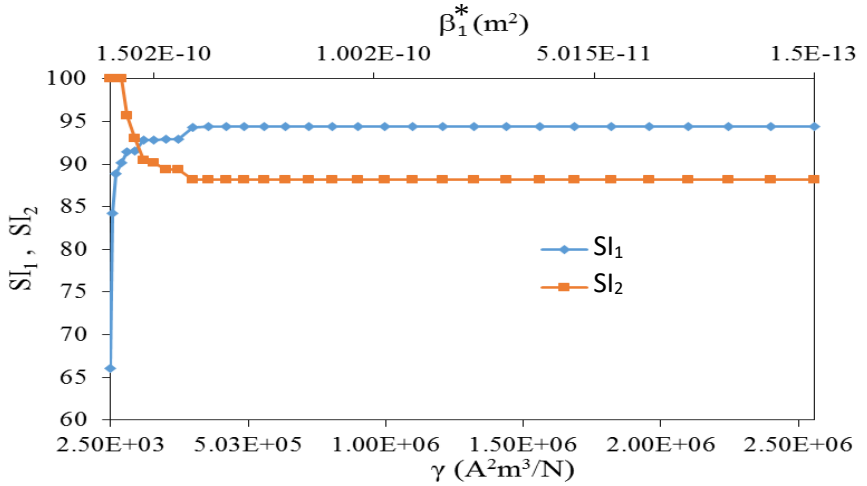

Fig. 4.5 Variation of SI_1 and SI_2 as functions of γ for $\Pi_1 = 4.0\times10^{-7}$ A^2m^5/N and $\Pi_2 = 1.69\times10^{-7}$ A^2m^5/N (corresponding to the base values). The corresponding β^*_1 (= 2.37 β^*_2) is plotted along the secondary x axis.

The foregoing analysis optimizes the operating parameters of a standard SPLITT configuration to achieve a desirable range of capture efficiencies and separation indices. It is important to note that these performance parameters of the SPLITT device would also be influenced by the geometry of the device, e.g., the position, spacing and widths of the outlets, shape and positions of the separator plates, dipole position, etc. Therefore, complete design specification of SPLITT device would also warrant, over and above the present analysis, a detail study on the influence of the geometric parameters, which is left as future exercise.

4.3 Influence of geometry of channel on SPLITT device performance and comparison with the same for an FFF device

The salient difference in the FFF and SPLITT devices exists in the geometry of the outlet plane. While in FFF, the designated outlets for larger and smaller particles lay on the lower wall of the channel, for SPLITT device the two outlets occupy the main flow outlet (at $x = L$). Varying the relative dimensions of the individual outlets, therefore, offer avenues for altering the performance of both FFF and SPLITT devices. In this section, the influence of outlet flow channel widths for a SPLITT and FFF device is compared. The throughputs of the different sized particles through respective outlets are observed for different outlet dimensions. Heights of the outlet one, two and three of the SPLITT device are represented by $L_{S,O1}$, $L_{S,O2}$ and $L_{S,O3}$ respectively (see Fig. 3.4). Salient operating conditions (which partly differs from those used for the SPLITT devices so far) for the SPLITT and FFF devices are summarized in Table 4.3.

Table 4.3. The base values of different parameters of the present study for FFF and SPLITT device.

Parameters	Values	Parameters	Values
a_1 (μm)	1	μ (Pa-s)	0.001
a_2 (μm)	2	U_{av}(m/s)	0.014
$\chi_{eff,1}$	0.1	X_{mag} (m)	0.002
$\chi_{eff,2}$	0.1	Y_{mag} (m)	-0.002
ρ (kg/m^3)	1000		

4.3.1 SPLITT Device

Since the relative heights of the outlet ports alter the fluid fractionation (fraction of flow coming out from a particular device in a specific outlet) in the channel, is found that the outlet heights become one influencing parameter in capture efficiency and separation index. $L_{S,O1}$, $L_{S,O2}$ and $L_{S,O3}$ are varied keeping total outlet height constant ($L_{S,O1} + L_{S,O2} + L_{S,O3} = 0.15$ mm). Figure 4.6 shows how the capture efficiency is varied with increase and decrease of $L_{S,O1}$, $L_{S,O2}$

and $L_{S,O3}$. Figure 4.6(a) shows with increase $L_{S,O1}$, CE_1 increases but CE_2 decreases. Whereas, it is also noticed from the results that with increase $L_{S,O2}$, CE_2 increase but CE_1 decrease. From these two results it is observed that at some value of $L_{S,O1}$ and $L_{S,O2}$, CE_1 and CE_2 is maximum. Here one behaviour of the particles is noticed that is CE_1 is increasing more rapidly than CE_2. This is

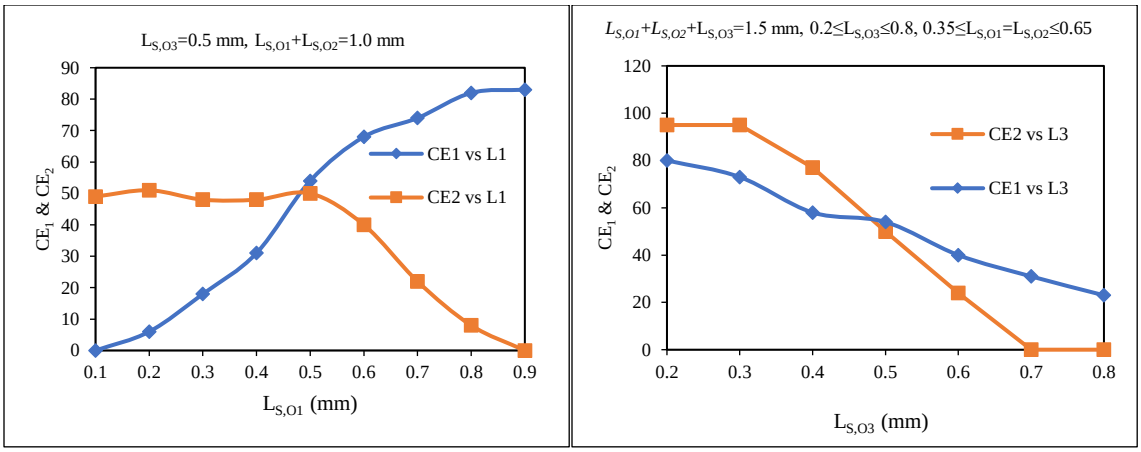

(a) (b)

Fig. 4.6 Variation of CE_1 and CE_2 with variation of length of (a) outlet1, $L_{S,O1}$, (b) outlet3, $L_{S,O3}$.

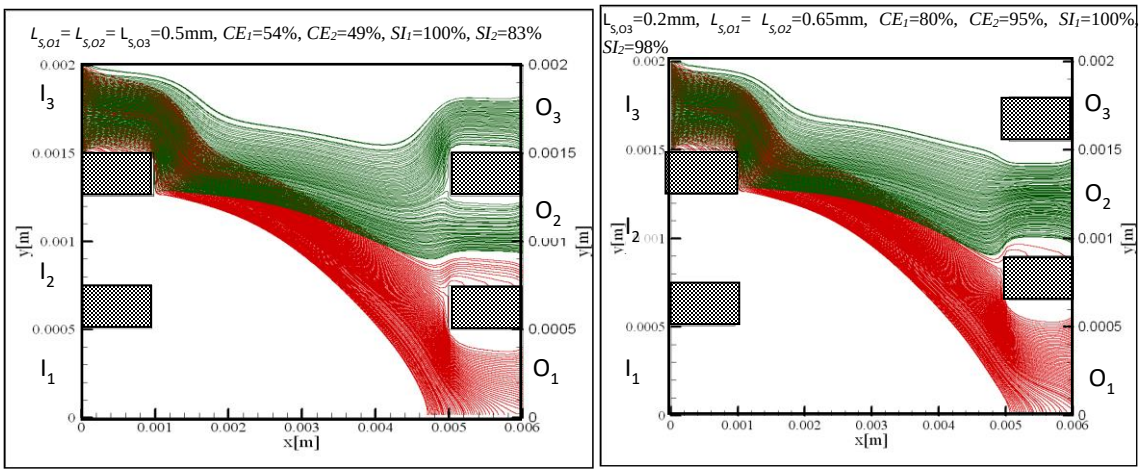

(a) (b)

Fig. 4.7 Variation of particle trajectories for different channel outlet length (a) $L_{S,O1} = L_{S,O2} = L_{S,O3}$=0.5 mm (b) $L_{S,O3}$=0.2 mm, $L_{S,O1} = L_{S,O2}$ =0.65 mm.

because some smaller particles are escaping through $L_{S,O3}$ continuously. Figure 4.6(b) shows with increase in $L_{S,O3}$, CE_1 and CE_2 both decreases. At the same time, with variation of $L_{S,O1}$ and $L_{S,O2}$ equally, CE_1 and CE_2 increases. This is because when $L_{S,O3}$ increases then $L_{S,O1}$ and $L_{S,O2}$ decreases proportionately. Therefore, particles do not get sufficient space for escaping through $L_{S,O1}$ and $L_{S,O2}$. From Fig. 4.7 it can be seen that with increase $L_{S,O1}$, $L_{S,O2}$ and decrease $L_{S,O3}$, CE_1 and CE_2 increases. In this figure it is noticed that with increase $L_{S,O1}$ and $L_{S,O2}$ more number of particles are escaping through the respective outlets. As a result, CE_1 is increased from 54 to 80 % and CE_2 from 49 to 95 % similarly SI_1 remains constant at 100 % at both the cases and SI_2 increases from 83 to 98 %. From the above results it is found that at $L_{S,O3}$ = 0.2 mm and $L_{S,O1}$ = $L_{S,O2}$ = 0.65 mm the maximum CE_1(80 %) and CE_2 (95 %) can be obtained with very high SI_1(100 %) and SI_2 (98 %) also.

4.3.2 FFF device

It is observed that as length of outlet1 ($L_{F,O1}$) is increased, initially CE_1 increased but this increasing trend tapered off beyond $L_{F,O1}$ = 1.6 mm. As more flow is diverted through the outlet 1 for an increased $L_{F,O1}$, more particles (even the smaller ones) escape through outlet1, thus pushing up the CE_1. However, CE_2 decreases with increasing $L_{F,O1}$ as more of the smaller particles start to be collected in outlet 1 leading to a decrease in CE_2. SI_1 is also affected because of this unwanted escape of the small particles through outlet 1 (see Figs. 4.8 and 4.9 (a)). The reverse trend (increasing CE_2 and decreasing CE_1) is observed with increase of $L_{F,O2}$ as the flow (and resulting drag) would tend to carry even some of the larger particles to outlet 2. From Fig. 4.9 (a) it may be observed that for $L_{F,O1}$ = 1.8 mm, $L_{F,O2}$ = 0.6 mm one gets very high CE_1 (= 94 %) and SI_2 (100 %), but CE_2 (45 %) and SI_1 (88 %) are lower. On the other hand, Fig. 4.9(b) shows that CE_1 88 %, CE_2 81 %, SI_1 100 %, SI_2 100 %. Between the

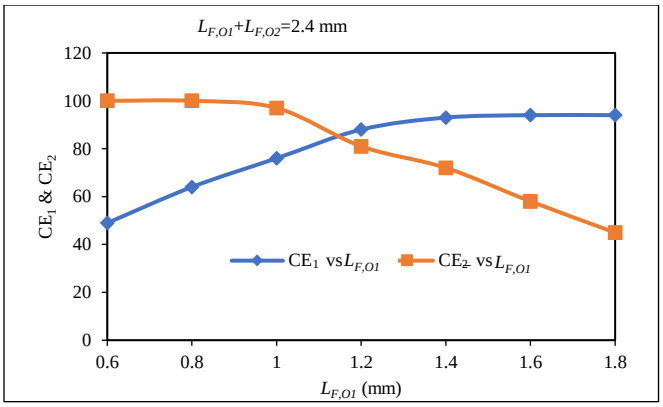

Fig. 4.8. Variation of CE_1 and CE_2 with length of outlet O_1, $L_{F,O1}$ when $L_{F,O1}$+ $L_{F,O2}$ = 2.4 mm.

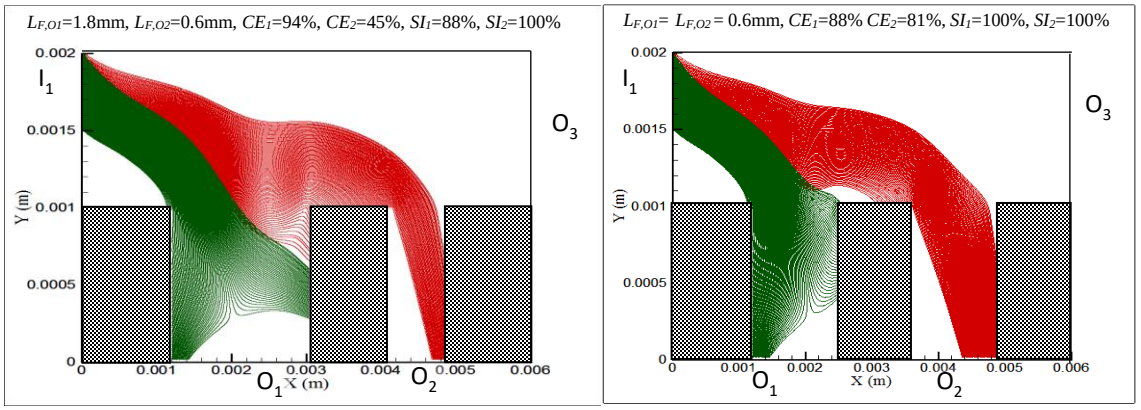

(a) (b)

Fig. 4.9 Particle trajectories in different outlet length (a) $L_{F,O1}$ = 1.8 mm, $L_{F,O2}$ = 0.6 mm and (b) $L_{F,O1}$ = $L_{F,O2}$ = 0.6 mm.

two cases described in Fig. 4.9 the FFF device will yield an overall better performance for $L_{F,O1}$ = $L_{F,O2}$ = 0.6 mm. The choice of operating conditions (the length ratios for the outlets) would also depend on the relative importance of collecting larger number of particles vis a vis collecting them unmixed.

4.4 Influence of operating regime in particle separation in hybrid free flow magnetophoretic microfluidic device

Having characterized the flow and particle separation in a SPLITT device in detail, and carrying out a brief comparison between the performances of FFF and SPLITT device under different outflow channel dimensions, we now aim at characterizing the performance of a magnetophoretic hybrid free flow magnetophoretic microfluidic device having two inlets and three outlets for immunomagnetic isolation of three different species from a continuous flow. The hybrid device works on the principle of split-flow thin (SPLITT) fractionation, field flow fractionation (FFF) mechanisms and free flow magnetophoresis. Transport of the magnetic particles in the microchannel has been predicted and influence of the salient operating parameters on the performance of the separator is studied by characterizing the particle trajectories, and their capture and separation indices. Finally, an optimum operating regime is identified that yields the maximum capture efficiency and separation index.

Table 4.4: Base values and the range of the operating parameters (a_1 and a_2 are magnetic, while a_3 is nonmagnetic particle)

Parameters	Base value (unit)	Ranges of variation (unit)
L (m)	0.006	Not varied
W (m)	0.002	Not varied
ρ (kg/m^3)	1000	Not varied
U_{av} (m/s)	0.01	0.003-0.023
μ (Pa-s)	0.001	0.0003-0.0013
a_1 (μm)	2	1.1-3.7
a_2 (μm)	1	0.1-1.8
a_3 (μm)	0.5	0.05-0.6
$\chi_{eff,1}$	0.1	0.01-0.34
$\chi_{eff,2}$	0.1	0.01-0.34
P (Am)	4	0.5-3.0
X_{mag} (mm)	6	Not varied
Y_{mag} (mm)	–1.5	Not varied

N_{part} ($m^{-2}s^{-1}$)	5×10^5	Not varied

4.4.1 Particle tracking

Figure 4.10 depicts the particle trajectory of 100 number of large (of diameter 2 μm and represented by red lines) and small (of diameter 1 μm and represented by cyan lines) magnetic and one type of nonmagnetic (of diameter 0.5 μm and represented by black lines) particles at base operating regime as shown in Table 4.4. The particles of each type are released inside the microchannel through I_1 (i.e., $0.0015 \leq y \leq 0.002$ m). For maintaining the particle influx rate of 5×10^5 $m^{-2}s^{-1}$ inside the channel of each type of particle, the number of particles in each cluster is so chosen. Inside the channel, particles are influenced by the fluidic drag and magnetic force. The results show that all the 100 number of large magnetic particles along with 8 out of 100 number of small magnetic particles are captured at O_1 (see Fig. 4.10). Among the rest of the small magnetic particles, 81 particles are captured at O_2 and the remaining 11

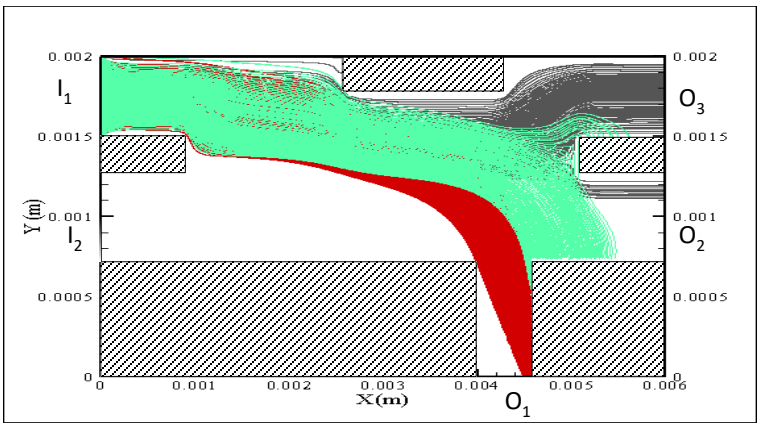

Fig 4.10 Particle trajectory of two different types magnetic microspheres (Red and turquoise ones) and one nonmagnetic microsphere (Black) inside the device at base operating regime as shown in Table 4.4.

particles are captured at O_3. Inside the 100 number of nonmagnetic particles, 16 are captured at O_2 and remaining are captured at O_3. Since the sizes of the magnetic particles are different,

the mobility of the particles varies due to magnetic and fluidic drag forces. Also, non-magnetic particles are only influenced by the drag force. The drifting velocity of the particles vary, which results in particles of different types being captured through a single outlet. This implies that a mixture of large and few small magnetic particles are captured at O_1 and a mixture of the nonmagnetic and small magnetic particles are captured at O_2 and O_3 as shown in Fig. 4.10.

4.4.2 Separation of magnetic and nonmagnetic microspheres

Figure 4.10 shows the trajectory of three different types of microspheres in the microfluidic device under the base operating regime. The basic objective of the present study is to separate three different types of particles simultaneously through their designated outlets i.e. large magnetic particles through O_1, small magnetic particles through O_2 and the nonmagnetic particles through O_3. Depending upon the drifting velocity obtained by the particles, they try to escape through non-designated outlets as shown in Fig. 4.10. Therefore, the device performance is characterized here by capture efficiency (*CE*) i.e., the ratio of number of particle clusters (large magnetic, small magnetic and nonmagnetic) collected at their designated outlets (i.e., O_1, O_2 and O_3, respectively) to the number of the corresponding particle clusters that has entered into the channel. Thus,

$$CE_1 = \frac{\text{Number of particle clusters of larger mobility collected at } O_1}{\text{Number of particle clusters of larger mobility entering the separator}}$$

$$CE_2 = \frac{\text{Number of particle clusters of smaller mobility collected at } O_2}{\text{Number of particle clusters of smaller mobility entering the separator}} \qquad \textbf{…..4.6}$$

$$CE_1 = \frac{\text{Number of particle clusters of nonmagnetic collected at } O_3}{\text{Number of particle clusters of nonmagnetic entering the separator}}$$

In the above format of *CE*, the microfluidic device record 100% CE_1, 81% CE_2 and 83% of CE_3 as can be viewed from Fig. 4.10, for base operating conditions. This suggests that all the incoming particles of the three type are not escaping through their designated outlets, as Fig. 4.10 shows that 8 small magnetic particles with large magnetic particles are escaping through O_1, 16 nonmagnetic particles with 81 small magnetic particles are escaping through O_2 and 11 small magnetic particles with 84 nonmagnetic particles are escaping through O_3. Therefore, the extent of the purity of separation is not perfect at the outlets (O_1, O_2 and O_3). In separating three different type particles, one unavoidable circumstance is the intermixing of different type particles during escaping through separate outlets. Total performance of the microfluidic device cannot only be justified by only *CE* due to the intermixing phenomenon. For a complete characterization of such type device, it is also very crucial to know the extent of intermixing of the particles in the outlets. Which can be achieved by considering the separation index (*SI*) for each type of particles. To quantify how good the purity of the separated streams is, separation index (*SI*) of the device is also evaluated as follows:

$$SI_1 = \frac{\text{Number of captured particle clusters of larger mobility collected at } O_1}{\text{Total number of particle clusters collected at } O_1}$$

$$SI_2 = \frac{\text{Number of captured particle clusters of smaller mobility collected at } O_2}{\text{Total number of particle clusters collected at } O_2} \qquad \textbf{…..4.7}$$

$$SI_3 = \frac{\text{Number of captured particle clusters of nonmagnetic collected at } O_3}{\text{Total number of particle clusters collected at } O_3}$$

The extent of the intermixing for Fig. 4.10 can be expressed as SI_1 = 93%, SI_2 = 83% and SI_3 = 88%.

4.4.2.1 Effect of operating parameters on *CE*

In the free flow magnetophoresis inside the hybrid microfluidic device for a pressure driven background flow configuration, trajectory of magnetic particles depends upon magnetic ($\mathbf{F}_m \sim 4/3\pi a^3 \chi_{eff} P^2$) and fluidic ($\mathbf{F}_d \sim 6\pi a \mu U_{av}$) force whereas, the trajectory of nonmagnetic particles depends only upon fluidic force ($\mathbf{F}_d \sim 6\pi a \mu U_{av}$). Hence capture efficiency (*CE*) and separation index (*SI*) becomes a function of the magnetic and fluidic force. Therefore, a group variable Π ($= a^2 \chi P^2/\mu U_{av}$) consisting of the magnetic and drag force, expected to be a function of *CE* and *SI* for the magnetic particles. Whereas *CE* and *SI* for the nonmagnetic particles are expected to be a function of fluidic group variable ξ {$=(a_3 \mu U_{av})$}, as they do not respond to the magnetic parameters.

Figure 4.11 (a) expresses the variation of CE_1 versus Π_1 ($= a_1^2 \chi_1 P^2/\mu U_{av}$). Inside the group variable, every parameter is varied keeping other parameters at their base values, as shown in Table 4.4. From Fig. 4.11 (a) it is observed that curves for the variations of every parameter are merging with each other. Figure 4.11 (a) also depicts that when the Π_1 exceeds the value of 1.8×10^{-8} A^2m^5/N, the value of *CE* also starts to increase above its near-zero value, as a gradual increase in the marginal capture of larger magnetophoretic mobility particle begins at O_1. Π_1 increases with an increase in either a, P or χ_{eff}, that leads to an increase in particle magnetophoretic mobility. Otherwise, Π_1 increases with any decrease in either U_{av} or μ, and

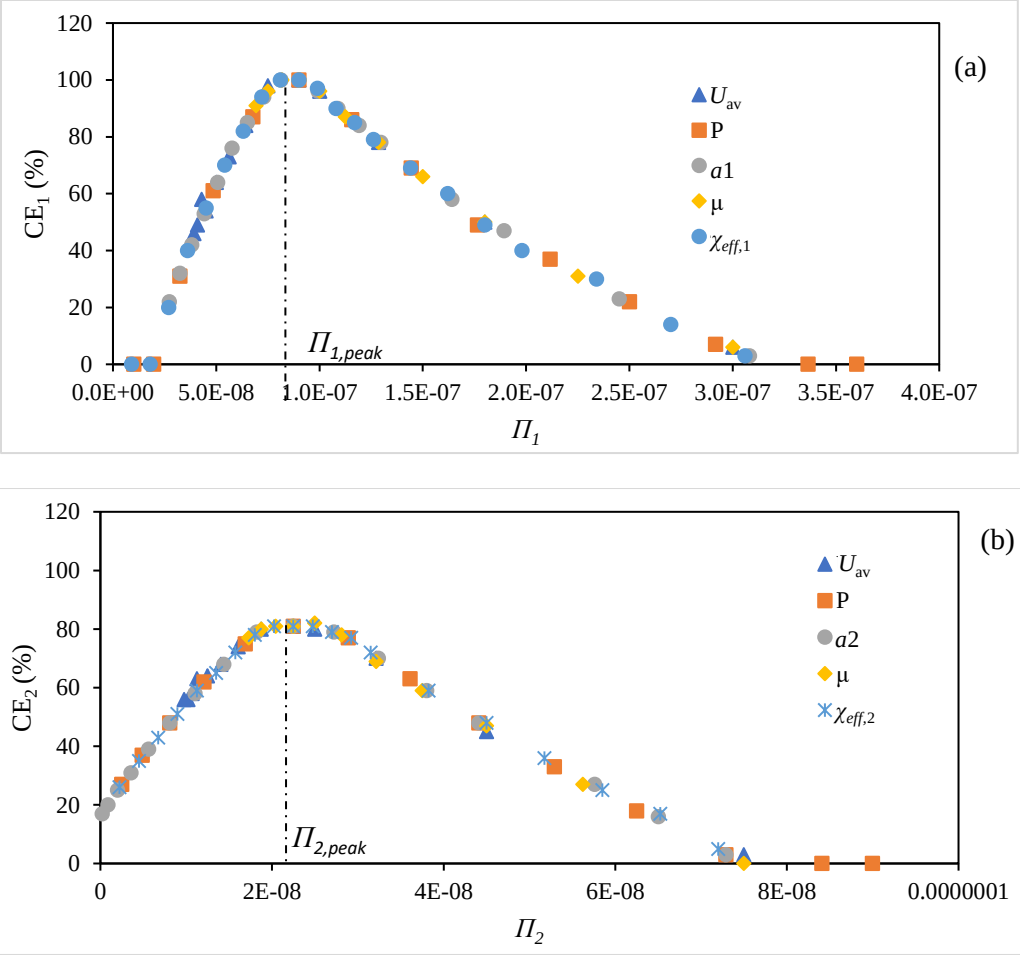

Fig. 4.11: (a) Large magnetic particle and **(b)** small magnetic particle capture efficiency, CE_1 and CE_2 as a function of Π_1 {=$(a_1^2\chi_{eff,1}P^2)/(\mu U_{av})$} and Π_2 {=$(a_2^2\chi_{eff,2}P^2)/(\mu U_{av})$} respectively for the microfluidic device. Results confirmed that CE values depend upon different magnetic and fluidic operating parameters (dipole strength P, magnetic susceptibility χ, particle size a, fluid viscosity μ and fluid velocity U_{av}), since all the parametric plots collapse on a single curve.

that decrease the particle fluidic influence which leads to a greater number of large particles get captured at O_1 (see Fig. 4.11 (a)). This increasing trend continues until the maximum value of CE_1 (100%) is reached when the value of $\Pi_{1,peak}$ is 8.1×10^{-8} A^2m^5/N. Beyond this value of $\Pi_{1,peak}$, CE_1 decreases as a greater number of large magnetic particles get captured before O_1 due to increased magnetic influence or decreased fluidic influence. This trend ends at Π_1 =

3.364×10^{-7} A^2m^5/N, when CE_1 drops down to zero, due to non-capture of large magnetic particles at O_1.

Figure 4.11 (b) shows the variation of CE_2 with a variation of Π_2 ($= a_2^2\chi_2P^2/\mu U_{av}$). The trend of the curve in Fig. 4.11 (b) is similar to that of Fig. 4.11 (a), initially CE_2 increases and then decreases beyond $\Pi_{2,peak}$. Maximum CE_2 is observed when $\Pi_{2,peak}$ is 2.25×10^{-8} A^2m^5/N. After $\Pi_{2,peak}$, CE_2 decreases because when fluid velocity or fluid viscosity increases, a greater number of small magnetic particle try to escape through O_3 otherwise, they try to escape through O_1, when P, a or χ_{eff} is increased. Finally, the decreasing trends end beyond the Π_2 value of $\approx 8\times10^{-8}$ A^2m^5/N, when no small magnetic particle get captured at O_2. From Fig. 4.11 (a) and (b) it is also observed that $\Pi_{1,peak} > \Pi_{2,peak}$, this may be because of the position of O_2. From Fig. 4.11 (a) and (b), it is evident that the user would prefer to operate the device such that the value of Π remain close to the Π_{peak}.

Figure 4.12 shows the variation of CE_3 for the nonmagnetic particles with a variation of fluidic group variable ξ $\{=(a_3\mu U_{av})\}$. The nonmagnetic particles are not be influenced by the magnetic force since it has no intrinsic magnetic property. As a result, there are no effect of P and χ_{eff} on CE_3. Intuitively, a group variable ξ $\{=(a_3\mu U_{av})\}$ is considered here without any magnetic parameter, as nonmagnetic particles are influenced only by drag force ($\mathbf{F}_d \sim 6\pi a\mu U_{av}$). As the magnetic dipole is placed transverse to the flow direction, outside the channel, the magnetic particles try to cross the streamlines towards the magnetic dipole. Whereas, the nonmagnetic particles try to travel along the streamlines, as a result, there are no cross-stream migration of the nonmagnetic particles from the streamlines. They try to follow the streamlines of the fluid

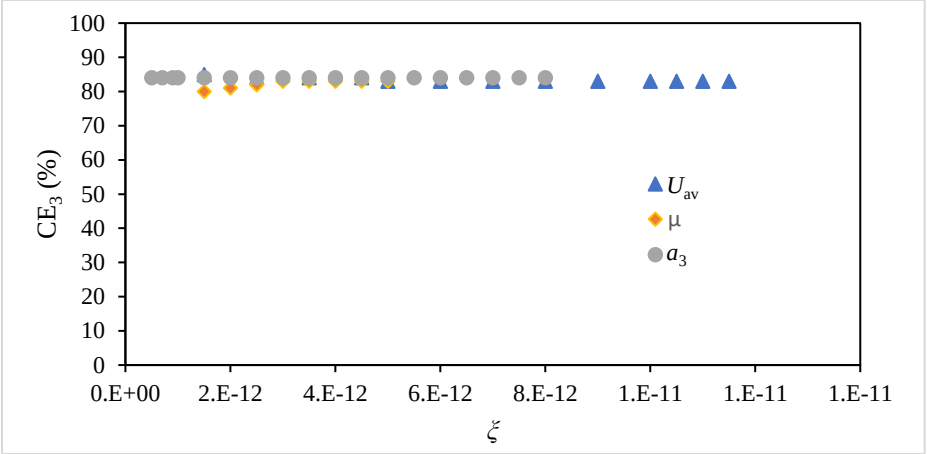

Fig. 4.12 Depicts nonmagnetic particle capture efficiency CE_3 as a function of ξ $\{=(a_3 \mu U_{av})\}$ for the microfluidic device. Results show that all the fluidic parametric plots collapse on a single curve, showing, how *CE* values depend upon different operating parameters (particle size a, fluid viscosity μ and fluid velocity U_{av}).

flow and also try to escape through O_3 not affected by the magnetic force. From Fig. 4.12 it can be observed that CE_3 is nearly invariant with ξ and its value is 83%, not 100%, this is due to the presence of an obstacle at the path from I_1 to O_3 (can be seen in Fig. 3.3) which results in escaping of 17 number of nonmagnetic particles through O_2.

4.4.2.2 Effect of operating parameters on *SI*

The capture efficiency of a particle depends upon its own trajectory only, whereas the separation index of the particle depends also on the trajectories of all other types of particles. Figure 4.13 (a) and (b) represents the variation of SI_1 and SI_2 with Π_1 *and* Π_2 respectively. From Fig. 4.13 (a) and (b) it is observed that all of the curves are not merging into a single one, unlike the *CE* curves in Fig. 4.11, when individual operating parameters are varied keeping the other parameters at their base values. For the *SI* curves, two different trends are found in Fig. 4.13 (a) and (b), one is for magnetic particle size (a) and particle magnetic susceptibility (χ_{eff}) and another is for other operating parameters (P, U_{av} and μ). Therefore, from these trends, two

different group variables can be defined as β^* ($=a^2\chi_{eff}$) and γ ($=P^2/U_{av}\mu$) so that Π can be expressed as

$$\Pi = \beta^*\gamma \qquad \textbf{…..(4.8)}$$

Figure 4.13 (a) and (b) show that the constituent parameters of the two-group variables merge with each other. From Fig. 4.13 (a) it is noticed that up to the value of 7.5×10^{-8} A^2m^5/N for Π_1, SI_1 remains at 100% as only large magnetic particles get captured at O_1, for the curve of γ variation for a constant β_1^* ($=4.0\times10^{-13}$ m^2). Beyond that value of Π_1, SI_1 decreases, due to the escape of other types of particles through O_1. This is because, as the U_{av} and μ increases, Π_1 decreases and drag force increases, which results in an increasing number of the small particles are being captured at O_2 instead of O_1, increasing the SI_1. When P increases Π_1 also increases, which results in an increase in the influence of magnetic force on the magnetic particles and a greater number of small particles get captured at O_1.

From Fig. 4.13 (b) it is observed that when the value of Π_2 increases beyond 4.9×10^{-9} A^2m^5/N, SI_2 increases for the curve of γ variation. This is because when P increases, large magnetic particles, which was initially captured at O_2 would now try to escape through O_1. This results in an increase in SI_2. When U_{av} and μ decrease, Π_2 increases, and the large magnetic particles, which previously captured at O_2 now are captured at O_1. This trend of the curve remains the same until Π_2 reaches the value of 2.025×10^{-9} A^2m^5/N, when maximum SI_2 is obtained at 83%. Beyond that value of Π_2, SI_2 again decreases. This is because, with a decrease in U_{av} and μ and an increase in P, small magnetic particles try to escape through O_1 with large magnetic particles. Since the trajectory of the nonmagnetic particles remains almost unchanged throughout the variations, therefore the relative impacts of their trajectories on SI_1 and SI_2 remain unchanged.

When the parameters of the other group variable β^*, i.e. a and χ_{eff} , are varied, its situation differs from the situation of γ variation. For instance, when the two-parameter a and χ_{eff} increases, Π_1 and Π_2 also increase, as a result ratio of $\Pi_1/\ \Pi_2$ increases. Therefore, in the Fig. 4.13 (a), plot of β^*_1 (varying a_1 and $\chi_{eff1,}$ keeping the other parameters constant at their base values) differ from the plot of γ (obtained by varying P, μ or U_{av}). Similar phenomenon observed in the plots of SI_2 vs Π_2 during variation of a_2 or $\chi_{eff,2}$, in comparison to the plots of γ. In Fig. 4.13 (a) and (b) it is noticed that both the curve for β^* during variation of a and χ_{eff} merge with each other.

Therefore, Fig. 4.11 recommends that the *CE* figures can be represented by the group variable Π, whereas Fig. 4.13 suggests that the *SI* values are better represented as a function of the product of the group variables β^* and γ for the magnetic particles. Since the *SI* vs Π plots clearly discrete into two basic trends: one for constant γ (i.e., varying β^*) and the other for

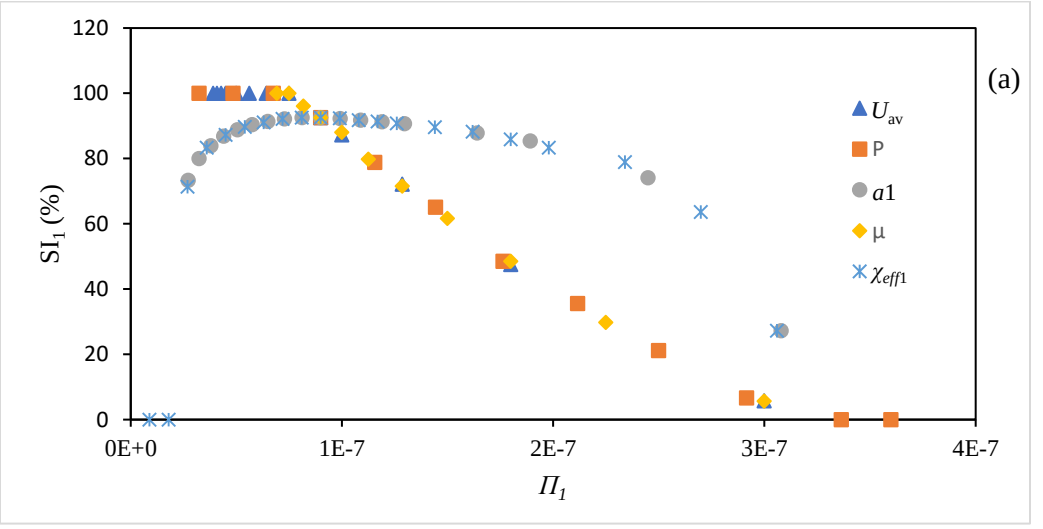

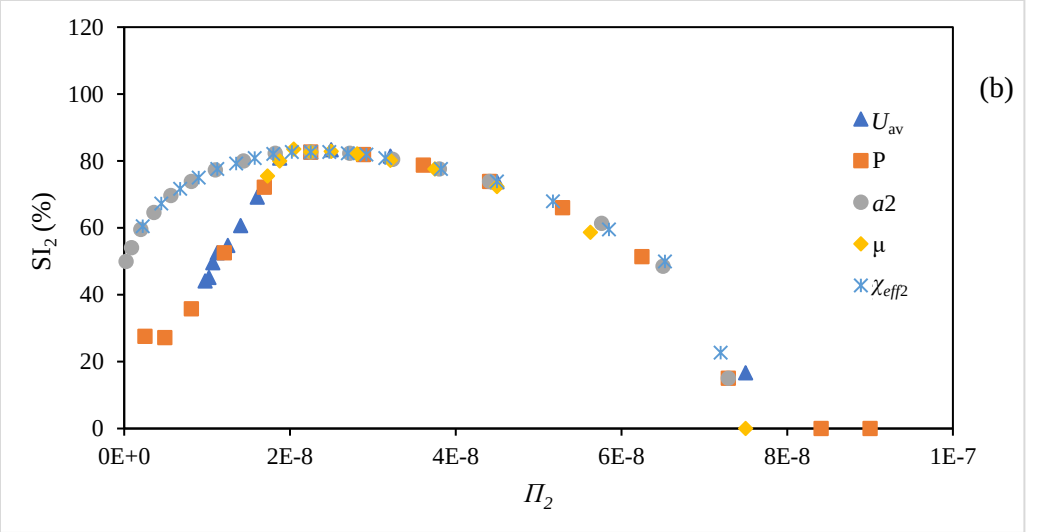

Fig. 4.13 (a) Large and **(b)** small magnetic particle separation index SI_1 and SI_2 as a function of Π_1 and Π_2. Results clearly separate out two basic trends as one for β^* ($=a^2\chi_{eff}$) and the other is γ ($=P^2/U_{av}\mu$).

constant β^* (i.e., varying γ). Both Figs. 4.11 and 4.13 serve as the basis for selection of the magnetic particle properties and the operating parameters (i.e., β^*) so as to operate the microfluidic device in the regime of best possible capture efficiencies and separation indices for both the magnetic particle types.

Figure 4.14 shows the variation of SI_3 with ξ. Here also all the individual parameters are varied keeping other parameters at their base values. Like Fig. 4.13, here also two different trend of *SI* curve is obtained, one is for U_{av} and μ, and the other one is for a. Since nonmagnetic particles does not react in magnetic field, influence P and χ are neglected for the present study. When a_3 is varied other parameters remain at their base values. With increase of a_3, ξ increases and drag force on the particles also increases, which influence only the nonmagnetic particles to escape from the device by following the streamlines of the fluid flow, therefore, no change in

SI_3 is observed. Whereas, when U_{av} and μ increases ξ increases, which influence the trajectories of magnetic and nonmagnetic particles, as a result SI_3 varies. With increase in U_{av} and μ drag

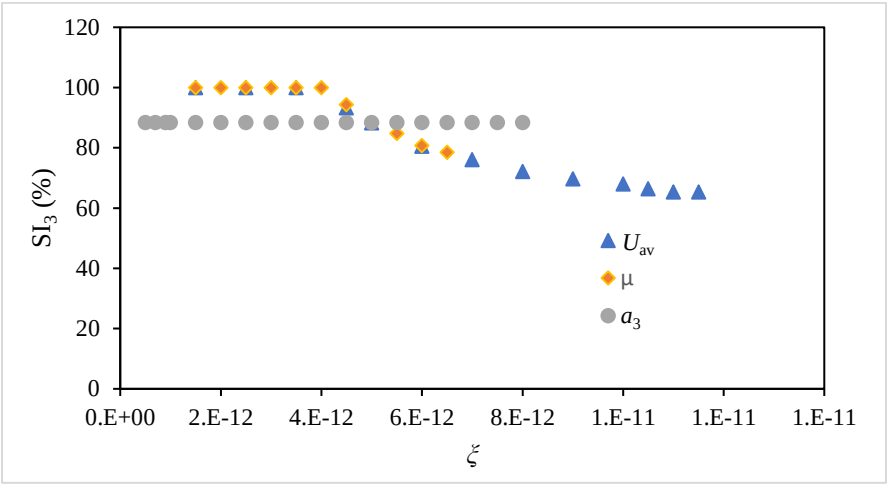

Fig. 4.14 Smallest nonmagnetic particle separation index SI_3 as a function of ξ. Results clearly separate out two basic trends as one for a_3 and the other is for γ^* ($=U_{av}\mu$).

force on the magnetic particles increases, meanwhile the influence of magnetic force on the magnetic particles remain unchanged. Which results in small magnetic particles, previously try to escape through O_2, now escape through O_3 decreasing the SI_3. From Fig. 4.14 it is observed that up to the value of 4.0×10^{-12} $Pam^2$of ξ, SI_3 remains at its maximum value (100%), after which it is decreases.

In comparison to Fig. 4.13, where two different group variables (β^* and γ) obtained from the result (based on the curves merged for individual parametric variation), here a and $\gamma^*(=U_{av}\mu)$ can be considered due to same reasons. Where γ^* is function of U_{av} and μ. Therefore, ξ can be expressed as

$$\xi = a\gamma^* \qquad \textbf{……..(4.9)}$$

4.5 Influence of channel geometry on separation of the hybrid free flow magnetophoretic microfluidic device

Having characterized the particle separation in the hybrid free flow magnetophoretic microfluidic device for getting the optimum operating parameters, now objective is to observe the influence of channel geometry on the performance of the magnetophoretic hybrid device. Transport of the magnetic and nonmagnetic particles in the microchannel are predicted based on the influence of the channel geometry and also noticed the impact of channel geometry on the performance of the separator in terms of capture efficiency and separation index. Finally, an optimum channel geometry is identified that yields the maximum capture efficiency and separation index.

4.5.1 Particle transport for the base case

Simulations are conducted for a given set of particle and flow parameters (see Table 4.5), while the salient device geometry is chosen as described in Table 4.6 (see also Fig. 3.3). Figure 4.15 shows trajectories of 100 large (2 μm radius, denoted by red lines) magnetic particle clusters, 100 small (1 μm radius, denoted by cyan lines) magnetic particle clusters and 100 nonmagnetic (0.5 μm radius, denoted by black lines) particle clusters released from Inlet I_1 (i.e. $0.0015 \leq y \leq 0.002$ m). Initially, at the entry region of the channel all three types of particle clusters primarily experience the fluid drag force, as the magnetic force is relatively weak there due to large distance from the dipole. As the particles are advected downstream nearer to the line dipole, magnetic particles experience stronger magnetic force in the transverse direction, and the particles begin to show deviation towards the dipole.

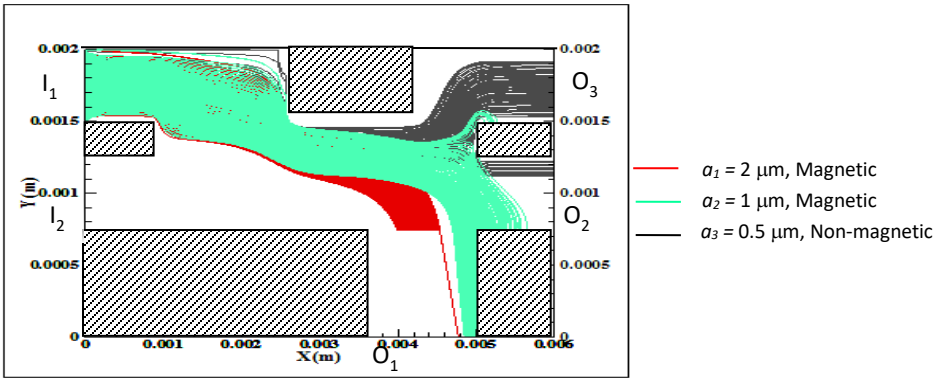

Fig. 4.15 Particle trajectories in the magnetophoretic hybrid free flow magnetophoretic device for the base case (Tables 4.5 and 4.6).

Larger magnetic particles exhibit higher magnetophoretic mobility than the smaller ones. On the contrary, the nonmagnetic particles experience only the drag force and therefore, they follow the streamlines. Because of the combined drag and magnetic force fields, the particles are fractionated at their designated outlets. It is evident from Fig. 4.15 that 4 large and 49 small clusters of magnetic particles are captured in the outlets O_1 and O_2 receives 42 small magnetic particle clusters along with 19 nonmagnetic ones. Outlet O_3 receives 80 number of nonmagnetic particle clusters along with 9 clusters of small magnetic particles.

Table 4.5: Values of the fluid and particle parameters considered for the study

	Fluid and Particle Parameters							
	a_1(µm)	a_2(µm)	a_3(µm)	P (A-m)	μ (Pa-s)	χ_1	χ_2	U_{av}(m/s)
Values	2	1	0.5	1.7	0.001	0.1	0.1	0.016

Table 4.6: Geometrical parameters considered for the study*

Parameters	Base values (mm)	Range (mm)	Parameters	Base values (mm)	Range (mm)
H_1	0.25	0.25-0.5	L_1	1.0	Constant
H_2	0.75	0.75-0.5	L_2	4.5	3.5-5.1
H_3	0.75	0.75-0.5	L_3	1.0	0.4-2.0
H_4	0.25	0.25-0.5	L_4	1.0	Constant
H_5	0.45	0-0.45	L_5	1.6	Constant

* H_i and L_i denote the height and length of different sections of the channel; I_i and O_i denote the inlet and outlet dimensions as indicated in Fig. 3.3. Overall device dimension: L= 6 mm and H= 2 mm; the line dipole P (Fig. 3.3) is placed at X_{mag}= 5 mm and Y_{mag} = – 0.7 mm.

4.5.2 Capture Efficiency and Separation Index

The intended performance of the device is to collect the maximum number of particle clusters in their designated outlets with very little intermingling; larger magnetic particle clusters should be collected at outlet O_1 and the smaller should collect at outlet O_2, while the nonmagnetic particles are designated to outlet O_3. Therefore, the performance of the device for separating the incoming particles at their designated outlets can be quantified in terms of Capture Efficiency (*CE*), as explained in Eq. 4.6.

Intermingling of different particles is practically unavoidable, leading to the possibility of collection of a few clusters of particles other than the designated ones at a particular outlet. Therefore, the performance of the device cannot be justified with *CE* alone. To quantify how good the purity of the separated streams is, separation index (*SI*) of the device is also evaluated from Eq. number 4.7. As an extension to previous work, here it is intended to realize the effect of channel geometry on the capture efficiency (*CE*) and separation index (*SI*). In the previous study a wide parametric variation carried out in terms of a group variable Π (= $(a^2\chi P^2/\mu U_{av})$). Here main focus is the effect of the key channel dimensions on the device performance, while all the parameters are kept at their base value (as listed in Table 4.5).

4.5.2.1 Effect of channel geometry

Figure 3.3 shows the schematic diagram of the hybrid device with the channel dimensions. Layout of the flow passage can be altered by adjusting the relative locations and widths of the inlets and outlets. The objective of the present study is to identify how these salient design parameters can influence *CE* and *SI* of the device. In the present simulation, the variation is achieved by changing the transverse dimensions of the blocks B_1, B_2, B_3, B_4 and B_5, and the

longitudinal dimensions of the blocks B_2 and B_3 (see Fig. 3.3). The total length (L) and width (H) of the separator chip and the dipole position (X_{mag}, Y_{mag}) are, however, kept fixed at their base values throughout the simulation. Figure 4.16 describes the effect of variation of the flow passage area (i.e., channel volume per unit depth) on the device performance. Starting from the base configuration (Table 4.6 and Fig. 4.15) the heights of blocks B_2 (H_2) and B_3 (H_3) are simultaneously decreased in steps of 500 μm and those of B_1 (H_1) and B_4 (H_4) are equally increased, keeping the widths of the inlet I_2 and outlet O_2 unchanged. This way, the flow passage is progressively dilated; at the same time the separation between the dipole and the flow passage decreases. As can be seen from Figs. 4.15, 4.16(a) and (b), nonmagnetic particle clusters, which experience only drag force (and therefore follow the streamlines emanating from inlet I_1), are directed through O_3. With increased H_1 and H_4 a greater number of streamlines from I_1 passes through O_3. As a result, CE_3 increases slightly with the passage area (Fig. 4.16(c)). At the same time, due to decrease of H_2 and H_3 the lower bound of the flow passage is pushed down. This leads more number of small magnetic particles, which previously passed out through O_2, to now escape through O_1 (see Figs. 4.16(a) and (b)). This results in a reduction of CE_2 and SI_2 (Fig. 4.16(c) and (d)). Also, due to increased H_4, and reduction in H_3, trajectories of the large magnetic particles deviate downward, thereby trapping most of those particles on the wall of B_2. The base value of O_1 is so chosen that 4 clusters of large magnetic particles escape through O_1. Lowering the values of H_2 and H_3 further aggravates the situation. The values of CE_1 and SI_1 decrease to zero below a flow passage area of 6.83×10^{-6} m^2.

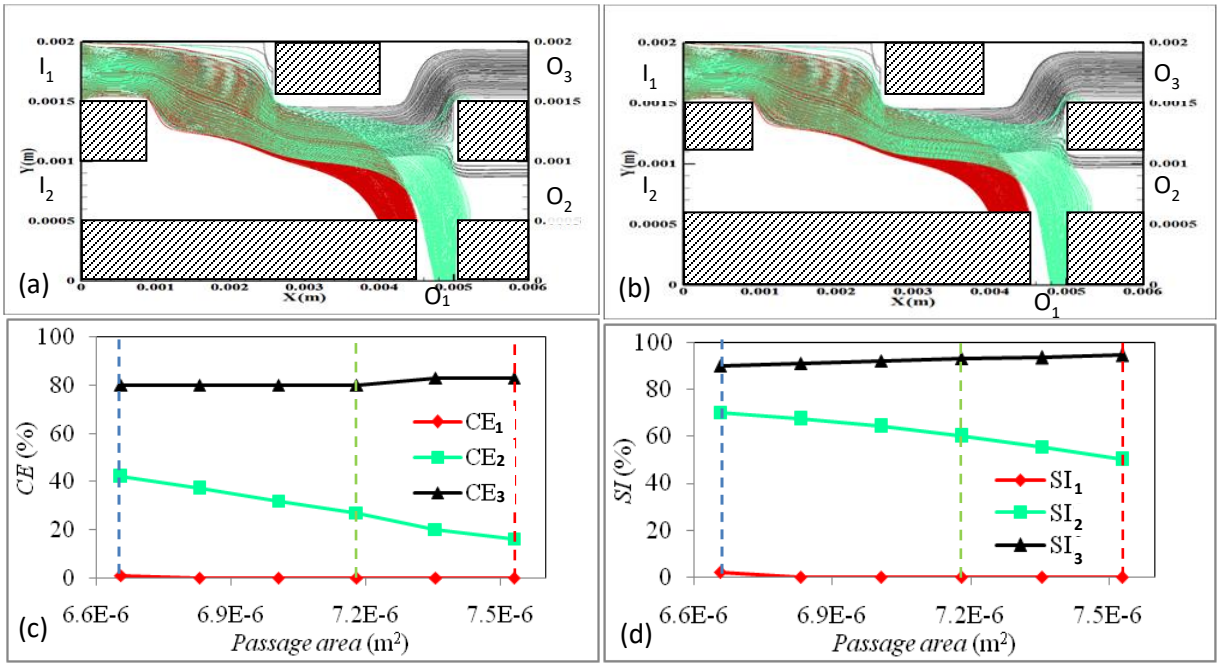

Fig. 4.16 Particle trajectories for (a) $H_1 = H_4 = 0.0005$ m and $H_2 = H_3 = 0.0005$ m, and (b) $H_1 = H_4 = 0.0004$ m and $H_2 = H_3 = 0.0006$ m. Variation of *CE* (c) and *SI* (d) with the passage area of the channel. Area of the passage is increased by simultaneously reducing the heights of blocks B_2 (H_2) and B_3 (H_3) in steps of 500 μm and increasing those of B_1 (H_1) and B_4 (H_4) equally. Vertical dotted lines denote the base case (blue), case-a (red) and case-b (green).

Figure 4.17 shows the variation of *CE* and *SI* due to the change of the position of O_1. This is achieved by simultaneously increasing L_2 and decreasing L_3, or vice versa, by equal magnitude, so that O_1 remains constant. Figures 4.17(a) and (b) show the particle trajectories for L_2 = 0.0041 m and 0.0035 m, respectively. When L_2 is decreased from its base value of 0.0045 m to 0.0041 m (accordingly, L_3 is increased from 0.001 m to 0.0014 m), the outlet O_1 is shifted upstream by 400 μm. Under this condition, most of the large magnetic particles are found (Fig. 4.17(a)) to collect at the outlet O_1, yielding a large CE_1 (~84%) and SI_1 (90%). At the same time, with decreased L_2 more of the smaller magnetic particles, which were transported to the outlet O_1 in Fig. 4.15, now collect at the outlet O_2. This leads to an increased CE_2 over the base case. When L_2 is decreased further to 0.0035 m (see Fig. 4.17 (b)), some of the large particles skip the outlet O_1 and collect at outlet O_2. This reduces both CE_1 and SI_2 as compared to the

case of Fig. 4.17 (a). The trajectories of nonmagnetic particles in Figs. 4.17 (a) and (b), and their corresponding *CE* and *SI* values do not alter much from the base case. Figures 4.17 (c) and (d) graphically show the influence of L_2 on *CE* and *SI*, where a peak of CE_1 at $L_2 = 0.004$ m is observed yielding $CE_1 = 97\%$ and $SI_1 = 100\%$. On either sides of $L_2 = 0.004$ m CE_1 decreases; while SI_1 remains close to 100% for smaller value of L_2 and decreases sharply for L_2>0.004 m. Figure 4.17 (b) also shows that CE_2 remains high (~ 100%) for L_2<0.004 m and decreases monotonically at higher L_2. CE_3 and SI_3 are found almost constant – with increase or decrease of position of O_1 there is no effect on CE_3 and SI_3 because nonmagnetic particles only follow streamlines from I_1. In the subsequent section of the paper, we choose $L_2 = 0.004$ m, since it simultaneously offers high values of *CE* and *SI* for all the three types of particles.

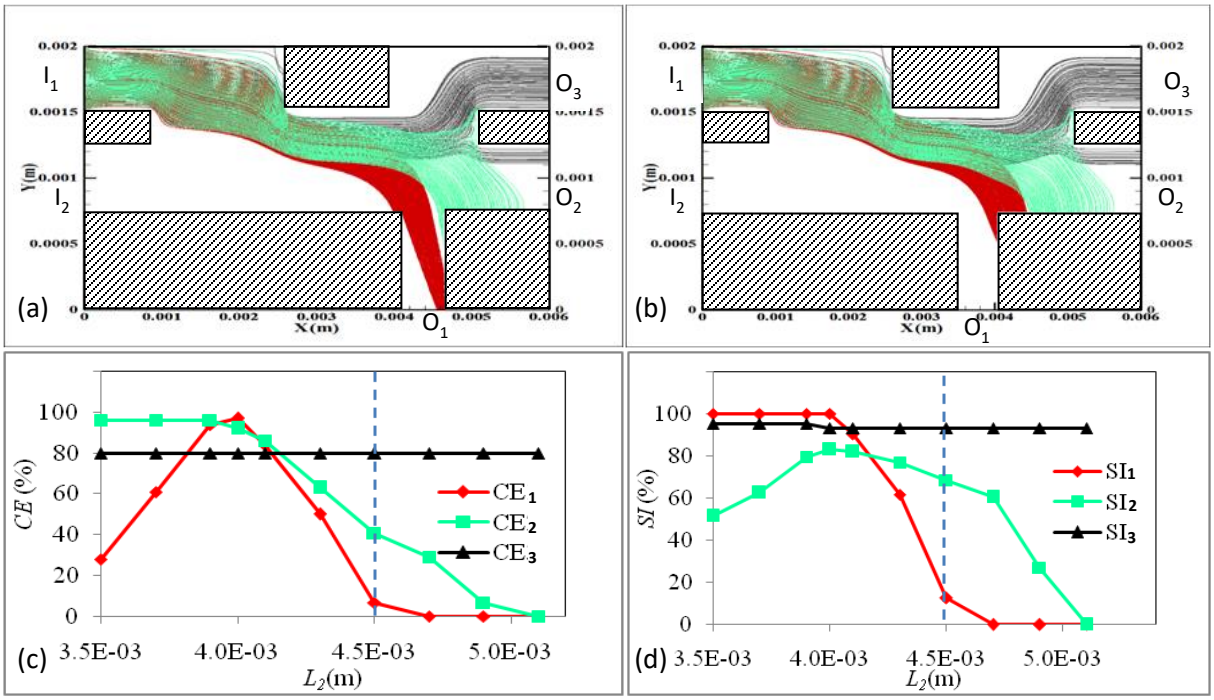

Fig. 4.17 Particle trajectories for (a) $L_2 = 0.0041$ m and (b) $L_2 = 0.0035$ m. Variation of *CE* (c) and *SI* (d) with the position of the O_1 (shown in terms of L_2). Vertical dotted lines denote the base case.

Once the optimum position of the O_1 is found, we next evaluate the influence of the relative widths of the other two outlets on the performance of the separator. Figure 4.18 shows how *CE* and *SI* vary with the outlet widths O_2 and O_3 while their combined width remains constant – thus an increase in O_2 (with respect to the base case) is accompanied by an equal decrease in O_3. L_2 and L_3 are chosen at their optimized values of 0.004 m, and 0.0015 m, while all other dimensions remain as per Table 4.6. Figures 4.18(a) and (b) show the particle trajectories for O_3 = 350 and 700 μm, respectively (base value of O_3 is 500 μm). The corresponding trends of *CE* and *SI* are plotted in Figs. 4.18 (c) and (d). Comparing the trajectories of Figs. 4.18 (a) and (b) with Fig. 4.15, it is apparent that the particle separation between the O_2 and O_3 is largely influenced by the flow fractionation. With increased O_3, more of the nonmagnetic particles try to escape through O_3; CE_3 gradually increases and eventually saturates at 100% (Fig. 4.18 (c)). However, with increased O_3 (and accompanying reduction of O_2) more clusters of the smaller magnetic particles also tend to flow out through it. This leads to a reduction in CE_2 and SI_3. Similarly, for low value of O_3, more clusters of nonmagnetic particles are collected through O_2, resulting in a reduction in CE_3 and SI_2. These relative widths of O_2 and O_3 do not seem to affect trajectories of the large magnetic particles. As a result, CE_1 and SI_1 remain constant, close to their optimized values observed from Fig. 4.17. From the plots of Figs. 4.18 (c) and (d), we choose O_3 = 520 μm and O_2 = 480 μm as the best performance point (marked by the blue vertical dotted lines in the figures).

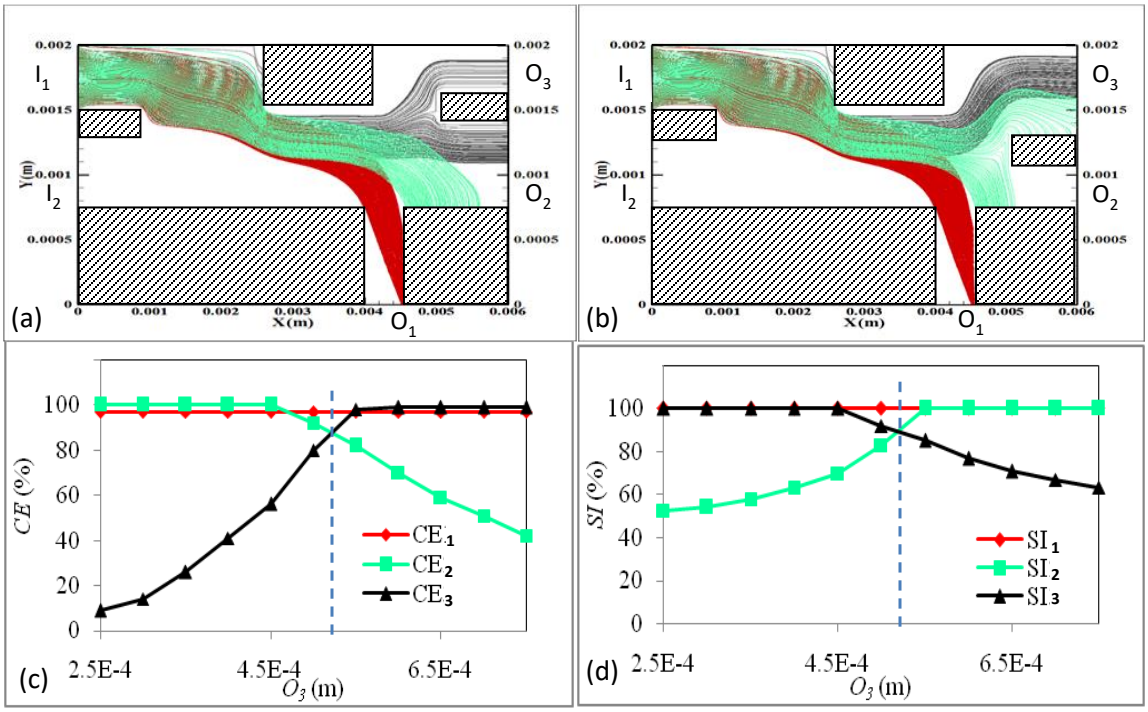

Fig. 4.18 Particle trajectories for (a) O_3 = 0.00035 m, O_2 = 0.00065 m and (b) O_3 = 0.0007 m, O_2 = 0.0003 m. L_2 (= 0.004 m) and L_3 (= 0.0015 m) are chosen from the optimum values observed in Fig. 2.14. Variation of *CE* (c) and *SI* (d) with the relative widths of outlets O_2 and O_3.

Finally, the influence of the width of the block B_5 is evaluated with the other geometries corresponding to the optimum condition observed in Figs. 4.18 (c) and (d) marked by the blue dotted lines. Figure 4.19 shows the variation of *CE* and *SI* with variation of H_5. Figure 4.19(a) shows that both CE_1 and CE_2 increase with H_5. As the height of the block B_5 increases, both types of magnetic particles (large and small) are diverted closer to the dipole. This increases the average magnetic force on them, enhancing the particle capture. The optimized channel geometry in Fig. 4.18 is obtained for H_5 = 450 µm, for which the largest values of *CE* and *SI* are also observed in Fig. 4.19. The plots also show a nearly invariant CE_3 in Fig. 4.19 – nonmagnetic particles are not affected by magnetic field, therefore, bringing them closer to the magnetic field (by increasing H_5) does not eventually alter their capture efficiency. The SI_1 remains saturated at ~100% throughout the range of H_5, indicating no trace of the smaller

particles in O_1. For the conditions investigated in Fig. 4.19, the optimum value of H_5 is found to be 450 µm.

Table 4.7: Optimum values of the geometrical parameters

Parameters	Values (mm)	Parameters	Values (mm)	Parameters	Values (mm)
H_1	0.25	L_1	1.0	I_1	0.5
H_2	0.75	L_2	4.0	I_2	0.5
H_3	0.75	L_3	1.5	O_1	0.5
H_4	0.25	L_4	1.0	O_2	0.52
H_5	0.45	L_5	1.6	O_3	0.48

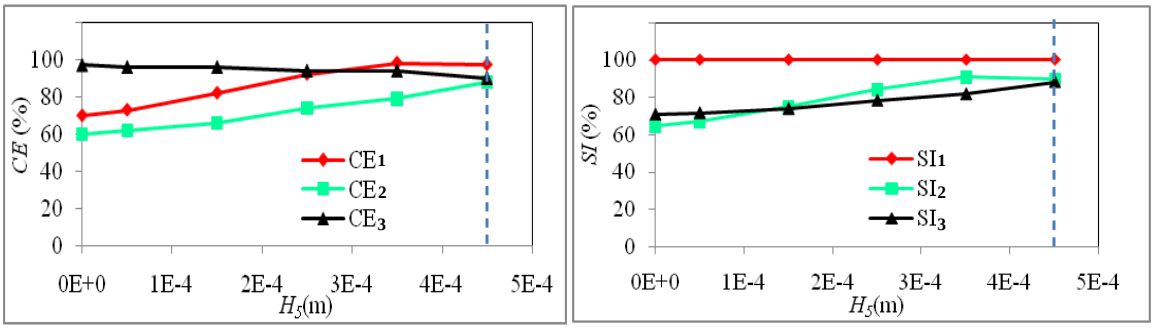

(a) (b)

Fig. 4.19 Variation of *CE* (a) and *SI* (b) with H_5. Vertical dashed lines denote the best configuration for the range of study described in Table 4.7.

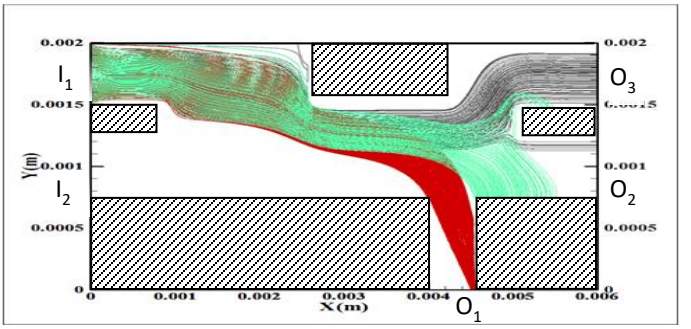

Fig. 4.20 Particle trajectory at optimized channel geometry.

Table 4.7 summarizes the optimized geometry for the hybrid separator while the particle trajectory for the optimized channel geometry is shown in Fig. 4.20. The optimum

configuration yields CE_1 = 97%, SI_1 = 100%, CE_2 = 88%, SI_2 = 90%, CE_3 = 90%, SI_3 = 88%. These are significantly higher than the previously reported capture efficiencies in FFF [126] and SPLITT (section 4.2) configurations. It is important to note that this optimized device performance is achieved with a lower dipole strength (P =1.7 A-m) as compared to the previously used dipole strength (P = 4 A-m). Thus, the hybrid separator clearly offers a better collection and separation performance, and at the same time offers separation of three different types of particles.

Chapter five: *Conclusion and scope of future work*

5.1 General conclusions

In the present thesis, the transport and separation of magnetic and nonmagnetic microspheres are characterized numerically in terms of various operating and geometric parameters. The transport and separation phenomenon of the microspheres are prescribed for different single-phase fluid flow configurations at microscale. Different types of microfluidic separation techniques are considered in the present thesis such as magnetic Field-flow Fractionation (FFF), Split-Flow Thin Fractionation (SPLITT), Hybrid microfluidic fractionation, and Free flow magnetophoresis. Separation of the superparamagnetic microspheres and nonmagnetic microspheres are characterized in terms of Capture Efficiency (*CE*) and separation index (*SI*) for each particle type. The transport and separation of the magnetic and nonmagnetic microspheres are prescribed numerically using a Eulerian-Lagrangian model of dispersed flow. After an extensive parametric study of the particle separation the following conclusions are arrived at:

- ✓ **Operating regime for the Split flow thin (SPLITT) fractionation device**

  Magnetophoretic separations of magnetic microspheres having two different magnetic mobilities have been investigated in microfluidic Split Flow Thin Fractionation (SPLITT). The magnetic and flow parameters were varied for a given geometrical configuration.

- The capture efficiencies CE_1 and CE_2 for the two types of particles are found to vary exclusively as functions of $\Pi_1=(a^2\chi_{eff,1}P^2/\mu U_{av})$ and $\Pi_2=(a^2\chi_{eff,2}P^2/\mu U_{av})$, respectively.

- Within the operating regime investigated, both CE_1 and CE_2 exhibit an increasing trend at low Π, peaking at an intermediate value and then declining at higher Π. Outside the operating regime, the CE values are found to be negligible.

- For the particle clusters of lower mobility, the collection port (O_2) is located closer to the original particle stream. Therefore, the CE_2 peak is observed at a lower value of Π_2 than the Π_1 for the CE_1 peak.

- Unlike the plots for the CEs, the SI vs Π plots do not collapse on single curve for variation of all the five parameters. However, the variation of separation index for each particle type can be grouped in terms of a common parameter $\gamma = P^2/U_{av}\mu$ (which influences the trajectories of both the particle types) and the particle-specific parameter $\beta^* = a^2\chi$ (which influences each particle type independently). SI values are better represented as function of the product of γ and β^*; the SI vs Π plots clearly separates into two basic trends ─ one for constant β^* (i.e., varying γ) and the other for constant γ (i.e., varying β^*).

✓ **Influence of geometry of channel on SPLITT device performance and comparison with the same for an FFF device**

Magnetophoretic separations of magnetic microspheres having two different magnetic mobilities has been investigated in microfluidic Split Flow Thin Fractionation (SPLITT) and Field Flow Fractionation (FFF) device configurations. The outlet lengths in both the devices are varied to

investigate their impacts on capture efficiency and separation index for a given operating (flow and magnetic) conditions.

- Among the two outlets for collecting two different types of particles, when length of one outlet increases, *CE* of the corresponding outlet increases, whereas, *CEs* of the remaining outlets decrease. The trend is similar for both FFF and SPLITT configurations.
- Between the two devices, the FFF yields an overall better performance when the designated outlet widths are same for the given operating conditions. The choice of operating conditions (the length ratios of the outlets) also depends on the relative influence of colleting larger number of particles vis-à-vis collecting them unmixed.

✓ **Influence of operating parameters on separation in hybrid free flow magnetophoretic microfluidic device**

- Like in SPLITT device, the capture efficiencies CE_1 and CE_2 for the two types of magnetic particles are found to vary exclusively as functions of Π_1 ($=a_1^2\chi_{eff,1}P^2/\mu U_{av}$) and Π_2 ($=a_2^2\chi_{eff,2}P^2/\mu U_{av}$), respectively for the hybrid free flow magnetophoretic device.

- Within the operating regime investigated, both CE_1 and CE_2 increase with Π_1 and Π_2 at their low values, attain maxima at intermediate values of Π and eventually drop down to zero at higher Π.

- The capture efficiency CE_3 for the non-magnetic particles remained insensitive to its radius, flow velocity and fluid viscosity.

- The SI_1 and SI_2 vs Π plots do not collapse on single curve for variation of all the five parameters. The variation of separation index for each particle type can be grouped in terms of a common parameter $\gamma = P^2 / U_{av}\mu$ (which influences the trajectories of both the particle types) and the particle specific parameter $\beta^* = a^2\chi$ (which influences each particle type independently).

- Unlike the plots for the CE_3, the SI_3 vs ξ plots do not collapse on single curve for variation of all the three parameters. However, the variation of separation index for the non-magnetic particle type, can be grouped in terms of a common parameter $\gamma^* = U_{av}\mu$ (which influences the trajectories of both the particle types) and the particle size a_3. SI_3 values are better represented as function of the product of γ^* and a_3; the SI_3 vs ξ plots for the non-magnetic particle type clearly separates into two basic trends ─ one for constant γ^* (i.e., varying a) and the other for constant a (i.e., varying γ^*).

✓ **Influence of channel geometry on separation in hybrid free flow magnetophoretic device**

The numerical study identifies the optimum channel geometry for best performance of the hybrid free flow magnetophoretic device to separate biological entities on a microfluidic platform practically for BioMEMS applications. Both *CE* and *SI* of the device are found to be strongly affected by the channel geometry. The effect of each salient geometrical parameters of the separator on *CE* and *SI* offers the design bases for the best device performance. For the optimized channel geometry reported here, higher *CE* and *SI* values are obtained even with relatively lower dipole strength than those observed in our previously reported studies on FFF and SPLITT configurations. The proposed hybrid magnetic separator, therefore, offers an improved design for immunomagnetic separation for biomedical applications.

The thesis provides a detailed study of magnetophoretic separation in different continuous flow configurations. The conclusions are obtained from the study can be used in developing the design bases for practical magnetophoretic bio-separator.

5.2 Recommendations for future work

In the present work, the impact of magnetic particle-particle interaction on separation has been neglected from the present study, since the particle suspension considered here is dilute. However, for denser particle suspensions, inter-particle interaction, can have an impact on particle trajectory and fluid flow. Different models of particle-particle interaction [152] may be considered as a future extension of the work. Besides, all the studies carried out in the present thesis pertains to pressure driven flow. The same can be extended for electroosmotic flow (EOF) and combined EOF and pressure-driven flows.

The studies on magnetophoretic separation carried out in the present thesis is entirely carried out computationally. The findings need to be validated experimentally in a future work. Based on the current simulations results, proof-of-concept microfluidic platform may be fabricated and experiments may be carried out in future. Also, different types of studies are carried out for separation in single-phase fluid flow configurations. Interesting phenomenon can be observed for magnetophoretic particle extraction in two phase flow configurations. Thus, the present computational model offers an appropriate platform for embarking on the several theoretically rich and practically useful future works.

5.3 Closing remarks

The microfluidic system consists of a series of basic mechanisms: a method of introducing reagents and samples (probably as fluids); methods to manipulate these fluids throughout the channel, and for combining and mixing them; and various other applications (such as detectors, separators for most microanalytical work etc.). A continuous effort is being given for developing and improving the manufacturing techniques to produce low-cost microfluidic devices in increasing quantities and making economically feasible, for using such devices as disposable items. A significant aspect of the commercial development of microfluidics is the development of advanced technology for fabricating the microfluidic devices. Therefore, it is necessary to develop advanced manufacturing processes for rapid and mass reproducible production of microfluidic devices. In this regard two particularly important contributions have been the application of soft lithography technique in PDMS as a method for fabricating microfluidic devices [153] and also, the development of a simple process of fabricating pneumatically activated mixers, valves and pumps using the same procedures [154]. Another challenge in developing the magnetophoretic microfluidic separator will be to fabricate the chip-embedded micro-electromagnets and their energization accessories. Silicon-based technology has been shown effective in fabrication of microelectromagnets [155]. The advanced manufacturing technologies make possible the fabrication of microfluidic devices, that can test new ideas in a time period much shorter (typically less than 2 days from design to working device) than by using silicon technology (typically, for non-specialists, a month or more). Low-cost, paper or polymer-based open surface microfluidic platforms are also emerging in a big way, since they have drastically reduced production cost and time [156].

Therefore, microfluidics with new methods of fabrication has been successfully able to exploit certain fundamental differences between the physical properties of fluids moving in macro and micro scale channels [157]. The advancements in microfabrication techniques permit for further reducing the lab-on-a-chip devices from micron to nanometre regime. Meanwhile, much of the non-traditional physics is still to be exposed and many thrilling applications of lab-on-a chip devices are yet to be exploited.

References

[1] Manz A, Graber N, Widmer H M, Miniaturized total chemical analysis systems: A novel concept for chemical sensing, Sens Actuators B Chem, 1990; 1: 244.

[2] Whitesides G M, The origins and the future of microfluidics, Nature, 2006; 442: 368.

[3] Yager P, Edwards T, Fu E, Helton K, Nelson K, Tam MR, Weigl BH, Edwards T, Fu E, Helton K, Nelson K, Tam MR, Weigl BH, Microfluidic diagnostic technologies for global public health, Nature. 2006; 442: 412–418

[4] Yetisen AK, Paper-based microfluidic point-of-care diagnostic devices, Lab on a Chip, 2013; 13: 2210–2251.

[5] Berthier J and Silberzan P, Microfluidics for Biotechnology, Artech House, Boston, 2006.

[6] Li PCH, Microfluidic Lab-on-a-Chip for Chemical and Biological analysis and discovery, Taylor & Francis Group, Boca Raton, 2006.

[7] Robert D, Pamme N, Conjeaud H, Gazeau F, Iles A, Wilhelm C, Cell sorting by endocytotic capacity in a microfluidic magnetophoresis device, Lab Chip, 2011; 11: 1902–10.

[8] Nandy K, Chaudhuri S, Ganguly R, Puri IK, Analytical model for the magnetophoretic capture of magnetic microspheres in microfluidic devices, J Magn Magn Mater, 2008; 320: 1398–405.

[9] Sinha A, Ganguly R, Puri IK. Magnetic separation from superparamagnetic particle suspensions, J Magn Magn Mater, 2009; 321: 2251–2256.

[10] Clarke C and Davies S, Metastasis research protocols, 2001; 336.

[11] Hirschbein BL, Brown DW, Whitesides GM, Magnetic separations in chemistry and biochemistry, CHEMTECH, March, 1982; 172–179.

[12] Dunlop EH, Feiler WA, Mattione MJ, Magnetic separation in biotechnology, Biotechnology Advances, 1984; 2: 63–74.

[13] Choi JW, Liakopoulos T M, Ahn C H, An on-chip magnetic bead separator using spiral electromagnets with semi-encapsulated permalloy, Biosens Bioelectron, 2001; 16: 409– 416.

[14] Verbruggen B, Leirs K, Puers R, Lammertyn J, Selective DNA extraction with microparticles in segmented flow, Microfluid Nanofluid, 2015; 18: 293-303.

[15] Iacob Gh, Ciochina Al D, Bredetean O, High gradient magnetic separation ordered matrices, European Cells and Materials, European Cells and Materials, 2002; 3: 167-169.

[16] Kim S, Han S-I, Park M-J, Jeon C-W, Joo Y-D, Choi I-H, Han K-H, Circulating Tumor Cell Microseparator Based on Lateral Magnetophoresis and Immunomagnetic Nanobeads, Anal Chem, 2013; 85: 2779−2786.

[17] Fuh CB, Lai JZ, Chang CM, Particle magnetic susceptibility determination using analytical split-flow thin fractionation, J Chromat A, 2001; 923: 263–270.

[18] Deng T, Prentiss M, Whitesides G M, Fabrication of magnetic microfiltration systems using soft lithography, Appl Phys Lett, 2002; 80: 461-463.

[19] Xia N, Hunt T P, Mayers B T, Alsberg E, Whitesides G M, Westervelt R M, Ingber D E, Combined microfluidic-micromagnetic separation of living cells in continuous flow, Biomed Microdevices, 2006; 8: 299–308.

[20] Zeng J, Deng Y, Vedantam P, Tzeng TR, Xuan X, Magnetic separation of particles and cells in ferrofluid flow through a straight microchannel using two offset magnets, J Magn Magn Mater, 2013; 346: 118–123.

[21] Puri IK, Ganguly R, Particle transport in therapeutic magnetic fields, Annu. Rev Fluid Mech, 2014; 46: 407–40.

[22] Gijs MAM, Lacharme F, Lehmann U, Microfluidic Applications of Magnetic Particles for Biological Analysis and Catalysis, Chem Rev, 2010; 110: 1518–1563.

[23] Gosling JP, Immunoassays: A Practical Approach.: Oxford University Press 2000

[24] Price NDJ C P, Principles and Practice of Immunoassay. Macmillan reference Ltd., 1997.

[25] Wu AH, A selected history and future of immunoassay development and applications in clinical chemistry, Clin Chim Acta, 2006; 369: 119 –124.

[26] Alefantis T, Grewal P, Ashton J, Khan AS, Valdes JJ, Del Vecchio VG, A rapid and sensitive magnetic bead-based immunoassay for the detection of staphylococcal enterotoxin B for high-through put screening, Mol Cell Probes, 2004; 18: 379-82.

[27] Degen IL, Kutsenok BS, Zhuravleva EA, Eglit EI, Ortop Travmatol Protez, 1977; 3: 67–70.

[28] Arruebo M, Fern´andez-Pacheco R, Ibarra MR, Santamar´ıa J, Magnetic nanoparticles for drug delivery, J Nano Today, 2007; 2: 22–32.

[29] Gillies GT, Ritter RC, Broaddus WC, Grady MS, Howard MA III, McNeil RG. Magnetic manipulation instrumentation for medical physics research, Rev Sci Instrum, 1994; 65: 533–45.

[30] Veiseh O, Gunn JW, Zhang M, Design and fabrication of magnetic nanoparticles for targeted drug delivery and imaging, Adv. Drug Delivery Rev, 2010; 62: 284–304.

[31] Jiang S, Win KY, Liu S, Teng CP, Zheng Y, Han M, Surface-functionalized nanoparticles for biosensing and imaging-guided therapeutics, Nanoscale, 2013; 5: 3127–3148.

[32] Yavuz CT, Mayo JT, Yu WW, Prakash A, Falkner JC, Yean SJ, Cong LL, Shipley HJ, Kan A, Tomson M, Natelson D, Colvin VL, Low-field magnetic separation of monodisperse Fe_3O_4 nanocrystals, Science, 2006; 314: 964–967.

[33] Yavuz CT, Prakash A, Mayo JT, Colvin VL, Magnetic Separations: From Steel Plants to Biotechnology, Chem Eng Sci, 2009; 64: 2510–2521.

[34] Mohanty S, Baier T, Schönfeld F, Three-dimensional CFD modelling of a continuous immunomagnetophoretic cell capture in BioMEMs, Biochem Eng J, 2010; 51: 110–116.

[35] Pongsritasana T, Wongratanacheewin S, Prasertcharoensuk V, Sermswan RW, Isolation of Fetal Nucleated Red Blood Cell from Maternal Blood using Immu-nomagnetic Beads for Prenatal Diag-nosis, Asian Pacific Journal of Allergy and Immunology, 2006; 24: 65-71.

[36] Schneider T, Karl S, Moore LR, Jeffrey, Chalmers JJ, Zborowski M, Sequential CD34 cell fractionation by magnetophoresis in a magnetic dipole flow sorter, Analyst, 2010; 135: 62–70.

[37]Sivagnanam V, Song B, Vandevyver C, Bünzli JCG, Gijs MAM, Selective Breast Cancer Cell Capture, Culture, and Immunocytochemical Analysis Using Self-Assembled Magnetic Bead Patterns in a Microfluidic Chip, Langmuir, 2010; 26: 6091–6096.

[38] Vašíček J, Parkányi V, Ondruška L, Makarevich A, Chrenek P, The potential use of magnetic activated cell sorting for elimination of rabbit apoptotic spermatozoa, Slovak J Anim Sci, 2010; 43: 205-209.

[39] Lee SHS, Hatton TA, Khan SA, Microfluidic continuous magnetophoretic protein separation using nanoparticle aggregates, Microfluid Nanofluid, 2011; 11: 429–438.

[40] Wang Y, Ye Z, Ping J, Jing S, Ying Y, Development of an aptamer-based impedimetric bioassay using microfluidic system and magnetic separation for protein detection, Biosens Bioelectron, 2014; 59: 106–111.

[41] Otieno BA, Krause CE, Latus A, Chikkaveeraiah BV, Faria RC, Rusling JF, On-line protein capture on magnetic beads for ultrasensitive microfluidic immunoassays of cancer biomarkers, Biosens Bioelectron, 2014; 53: 268–274.

[42] Mizuno M, Yamada M, Mitamura R, Ike K, Toyama K, Seki M, Magnetophoresis-Integrated Hydrodynamic Filtration System for Size- and Surface Marker-Based Two-Dimensional Cell Sorting, Anal Chem, 2013; 85: 7666−7673.

[43] Shibin He, Xu Yu, Xiangwu Wang, Junjun Tan, Shihan Yan, Pu Wang, Bi-Hai Huang, Zhi-Ling Zhang and Lijia Li, Fast magnetic isolation of simple sequence repeat markers in microfluidic channels, Lab Chip, 2014; 14: 1410.

[44] Pamme N, Continuous flow separations in microfluidic devices, Lab Chip, 2007; 7: 1644-1659.

[45] Huang LR, Cox EC, Austin RH and Sturm JC, Continuous particle separation through deterministic lateral displacement, Science, 2004; 304: 987-990.

[46] VanDelinder V and Groisman A, Separation of plasma from whole human blood in a continuous cross-flow in a molded microfluidic device, Anal Chem, 2006; 78: 3765-3771.

[47] Carlo DD, Irimia D, Tompkins RG and Toner M, Continuous inertial focusing, ordering, and separation of particles in microchannels, Proc Natl Acad Sci USA, 2007; 104: 18892.

[48] Zhang XL, Cooper JM, Monaghan PB and Haswell SJ, Continuous flow separation of particles within an asymmetric microfluidic device, Lab Chip, 2006; 6: 561.

[49] Ramji S, Pushpavanam S, Liquid-liquid extraction in laminar two-phase stratified flows in capillary microchannels, Chemical Engineering Science, 2019; 195: 242-249.

[50] Giddings JC, A New Separation Concept Based on a Coupling of Concentration and Flow Nonuniformities, J Sep Sci 1966; 1: 123.

[51] Carpino F, Doctor of Philosophy report in clinical and bioanalytical chemistry at the cleveland state university, 2008.

[52] Gale BK and Sant HJ, Nanoparticle analysis using microscale field flow fractionation, SPIE Proceedings, 2007; 6465.

[53] Giddings JC, The conceptual basis of field-flow fractionation, J Chem Educ 1973; 50: 667.

[54] Caldwell KD, Cheng ZQ, Hradecky P and Giddings JC, Separation of human and animal cells by steric field-flow fractionation, Cell Biophysics, 1984; 6: 233-251.

[55] Giddings JC, Hyperlayer Field-Flow Fractionation, Sep Sci Technol, 1983; 18: 765-773.

[56] Furlani EP, Sahoo Y, Analytical model for the magnetic field and force in a magnetophoretic microsystem, J Phys D Appl Phys, 2006; 39: 1724–1732.

[57] Williams PS, Lee S, Giddings JC, Characterization of hydrodynamic lift forces by field-flow fractionation. Inertial and near-wall lift forces, Chem Eng Comm, 1994; 130: 143-166.

[58] Sunok Oh, Kang D, Ahn S-M, Simpson RJ, Lee B-H, Moon MH, Miniaturized asymmetrical flow field-flow fractionation: Application to biological vesicles, J Sep Sci 2007; 30: 1082-1087.

[59] Kang D, Moon MH, Hollow fiber flow field-flow fractionation of proteins using a microbore channel, Anal Chem, 2005; 77: 4207-4212.

[60] Kim WS, Park YH, Shin JY, Lee DW, Lee S, Size determination of diesel soot particles using flow and sedimentation field-flow fractionation, Anal Chem, 1999; 71: 3265-3271.

[61] Park MR, Kang da Y, Chmelik J, Kang N, Kim JS, Lee S, Different elution modes and field programming in gravitational field-flow fractionation: Effect of channel angle, J Chromatogr A, 2008; 1209: 206-211.

[62] Edwards TL, Gale BK, Frazier AB, A microfabricated thermal field-flow fractionation system, Anal Chem, 2002; 74: 1211-1216.

[63] Gale BK, Srinivas M, Cyclical electrical field flow fractionation, Electrophoresis, 2005; 26: 1623-1632.

[64] Vickrey T M and Garcia-Ramirez J A, Magnetic field-flow fractionation: theoretical basis, Sep Sci Technol, 1980; 15: 1297–1304.

[65] Davis JM, and JC Giddings, Feasibility study of dielectric field-flow-fractionation, Sep Sci and Tech, 1986; 21: 969-989.

[66] Williams PS, Particle Trajectories in Field-Flow Fractionation and SPLITT Fractionation Channels, Sep Sci Technol, 1994; 29: 11-45.

[67] Fuh CB, Myers MN, Giddings JC, Centrifugal SPLITT fractionation: new technique for separation of colloidal particles, Ind Eng Chem Res, 1994; 33: 355-362.

[68] Giddings JC, A System Based on Split-Flow Lateral-Transport Thin (SPLITT) Separation Cells for Rapid and Continuous Particle Fractionation, Sep Sci Technol, 1985; 20: 749-768.

[69] Springston SR, Myers MN, Giddings JC, Continuous particle fractionation based on gravitational sedimentation in split-flow thin cells, Anal Chem, 1987; 59: 344-350.

[70] Gao Y, Myers MN, Barman BN, Giddings JC, Continuous fractionation of glass microspheres by gravitational sedimentation in split-flow thin (SPLITT) cells, Part. Sci Technol, 1991; 9: 105-118.

[71] Giddings JC, Continuous Particle Separation in Split-Flow Thin (SPLITT) Cells Using Hydrodynamic Lift Forces, Sep Sci Technol, 1988; 23: 119-131.

[72] Fuh CB, Giddings JC, Isoelectric Split-Flow Thin (SPLITT) Fractionation of Proteins, Sep Sci Technol, 1997; 32: 2945-2967.

[73] Giddings JC, Optimization of Transport-Driven Continuous SPLITT Fractionation, Sep Sci Technol, 1992; 27: 1489.

[74] Williams PS, Levin S, Lenczycki T, Giddings JC, Continuous SPLITT fractionation based on a diffusion mechanism, Ind Eng Chem Res, 1992; 31: 2172-2181.

[75] Gubala V, Harris LF, Ricco AJ, Tan MX, and Williams DE, Point of Care Diagnostics: Status and Future, Anal Chem, 2012; 84: 487–515.

[76] Gao W, Emaminejad S, Nyein HYY, Challa S, Chen K, Peck A, Fahad HM, Ota H, Shiraki H, Kiriya D, Lien D-H, Brooks GA, Davis RW, Javey A, Fully integrated wearable sensor arrays for multiplexed in situ perspiration analysis, Nature, 2016; 529: 509-514.

[77] Branda˜oa D, Lie´banab S and Pividori MI, Multiplexed detection of foodborne pathogens based on magnetic particles, New Biotechnol, 2015; 32: 511-520.

[78] Hejazian M, Li W, Nguyen N-T, Lab on a chip for continuous-flow magnetic cell separation, Lab Chip, 2015; 15:959–970.

[79] Lee W, Kwon D, Chung B, Jung GY, Au A, Folch A, and Jeon S, Ultrarapid Detection of Pathogenic Bacteria Using a 3D Immunomagnetic Flow Assay, Anal Chem, 2014; 86: 6683−6688.

[80] Lee J-J, Jeong KJ, Hashimoto M, Kwon AH, Rwei A, Shankarappa SA, Tsui JH, and Kohane DS, Synthetic Ligand-Coated Magnetic Nanoparticles for Microfluidic Bacterial Separation from Blood, Nano Lett, 2014; 14: 1−5.

[81] Pivetal J, Toru S, Robin MF, Haddour N, Cecillon S, Dempsey NM, Bouchiat FD, Simonet P, Selective isolation of bacterial cells within a microfluidic device using magnetic probe-based cell fishing, Sensors and Actuators B, 2014; 195: 581–589.

[82] Yuan D, Chen L, Li M, Xia H, Zhang Y, Chen T, Xia R, Tang Q, Gao F, Mo X, Liu M, Bi F, Isolation and characterization of circulating tumor cells from human gastric cancer patients, J Cancer Res Clin Oncol, 2015; 141: 647-660.

[83] Shen Z, Hou N, Jin M, Qiu Z, Wang J, Zhang B, Wang X, Wang J, Zhou D and Li J, A novel enzyme-linked immunosorbent assay for detection of Escherichia coli O157:H7 using immunomagnetic and beacon gold nanoparticles, Gut Pathogens, 2014; 6: 14.

[84] Ganguly R, Puri IK, Microfluidic transport in magnetic MEMS and BioMEMS, WIREs Nanomedicine & Nanobiotechnology, 2010; 2: 382–399.

[85] Wu Z, Chen Y, Wang M, Chung AJ, Continuous inertial microparticle and blood cell separation in straight channels with local microstructures, Lab Chip, 2016; 16: 532–542.

[86] Devendran C, Gralinski I, Neild A, Separation of particles using acoustic streaming and radiation forces in an open microfluidic channel, Microfluid Nanofluid, 2014; 17: 879–890.

[87] Laurell T, Petersson F, and Nilsson A, Chip integrated strategies for acoustic separation and manipulation of cells and particles, Chem Soc Rev, 2007; 36: 492–506.

[88] Lee KH, Kim SB, Lee KS Sung HJ, Enhancement by optical force of separation in pinched flow fractionation, Lab Chip, 2011; 11: 354–357.

[89] Milne G, Rhodes D, MacDonald M and Dholakia K, Fractionation of polydisperse colloid with acousto-optically generated potential energy landscapes, Opt Lett, 2007; 32: 1144–1146.

[90] Li M, Li S, Cao W, Li W, Wen W, Alici G, Improved concentration and separation of particles in a 3D dielectrophoretic chip integrating focusing, aligning and trapping, Microfluid Nanofluid, 2013; 14: 527–539.

[91] Li M, Li S, Li W, Wen W, Alici G, Continuous manipulation and separation of particles using combined obstacle- and curvature-induced direct current dielectrophoresis, Electrophoresis, 2013b; 34: 952–960.

[92] Kadaksham J, Singh P, Aubry N, Dielectrophoresis induced clustering regimes of viable yeast cells, Electrophoresis, 2005; 26: 3738–3744.

[93] Das D, Al-Rjoub MF, Heineman WR and Banerjee RK, Efficient capture of magnetic microbeads by sequentially switched electroosmotic flow—an experimental study, J Micromech Microeng, 2016; 26: 055013.

[94] Das D, Al-Rjoub MF, Banerjee RK, Enhanced Capture of Magnetic Microbeads Using Combination of Reduced Magnetic Field Strength and Sequentially Switched Electroosmotic Flow— A Numerical Study, Journal of Biomechanical Engineering, 137: 051008-1.

[95] Ganguly R, Sinha A, Puri IK, Magnetic particle-based microfluidics. Microfluidics and Nanofluidics Handbook, Volume Two: Fabrication, Implementation and Applications, CRC Press, Taylor and Francis, 2012; 433–483.

[96] Wang X, & Papautsky I, Size-based microfluidic multimodal microparticle sorter, Lab Chip, 2015; 15, 1350–1359.

[97] Nagrath S, Sequist LV, Maheswaran S, Bell DW, Irimia D, Ulkus L, Smith MR, Kwak EL, Digumarthy S, Muzikansky A, Ryan P, Balis UJ, Tompkins RG, Haber DA and Toner M, Isolation of rare circulating tumour cells in cancer patients by microchip technology, Nature, 2007;450: 1235–1239.

[98] Bhagat AA, Bow H, Hou HW, Tan SJ, Han J, Lim CT, Microfluidics for cell separation, Med Biol Eng Comput, 2010;48: 999–1014.

[99] Xu CX, Yin XF, Continuous cell introduction and rapid dynamic lysis for high-throughput single-cell analysis on microfluidic chips with hydrodynamic focusing, J Chromatograph A, 2011; 1218: 726–732.

[100] Ganguly R, Hahn T, Hardt S, Magnetophoretic mixing for in situ immunochemical binding on magnetic beads in a microfluidic channel, Microfluid Nanofluid, 2010; 8: 739–753.

[101] Rong R, Choi JW, Ahn CH, An on-chip magnetic bead separator for biocell sorting, J Micromech Microeng, 2006; 16: 2783–2790.

[102] Pekas N, Gragner M, Tondra M, Popple A, Porter MD, Magnetic particle diverter in an integrated microfluidic format, J Magn Magn Mater, 2005; 293: 584–588.

[103] Son OT, Roh JW, Song S-H, Park J-S, Lee W, Jung HI, Continuous micro-magnetophoretic separation using a dipole magnetic field, Biochip J, 2008; 2: 186–191.

[104] Carr C, Espy M, Nath P, Martin SL, Ward MD, Martin J, Design, fabrication and demonstration of a magnetophoresis chamber with 25 output fractions, J Magn Magn Mater, 2009; 321: 1440–1445.

[105] Inglis DW, Riehn R, Austin RH, Sturm JC, Continuous microfluidic immunomagnetic cell separation, Appl Phys Lett, 2004; 85: 5093–5095.

[106] Kim KS, Park J-K, Magnetic force-based multiplexed immunoassay using superparamagnetic nanoparticles in microfluidic channel, Lab Chip, 2005; 5: 657–664.

[107] Yung CW, Fiering J, Mueller AJ, Ingber DE, Micromagnetic–microfluidic blood cleansing device, Lab Chip, 2009; 9: 1171–1177.

[108] Modak N, Datta A, Ganguly R, Cell separation in a microfluidic channel using magnetic microspheres, Microfluid Nanofluid, 2009; 6: 647–660.

[109] Kirby D, Siegrist J, Kijanka G, Zavattoni L, Sheils O, O'Leary J, Burger R, Ducree J, Centrifugo-magnetophoretic particle separation, Microfluid Nanofluid, 2012; 13: 899–908.

[110] Khashan SA, Furlani EP, Scalability analysis of magnetic bead separation in a microchannel with an array of soft magnetic elements in a uniform magnetic field, Separation and Purification Technology, 2014; 125: 311–318.

[111] Khashan SA, Alazzam A, Furlani EP, Computational Analysis of Enhanced Magnetic Bioseparation in Microfluidic Systems with Flow-Invasive Magnetic Elements, Scientific Reports, 2014; 4: 5299.

[112] Kose AR, Fischer B, Mao L, Koser H, Label-free cellular manipulation and sorting via biocompatible ferrofluids, PNAS 2009; 106: 21478–21483.

[113] Liang L, Xuan X, Diamagnetic particle focusing using ferromicrofluidics with a single magnet, Microfluid Nanofluid, 2012; 13: 637–643.

[114] Zhu T, Marrero F, Mao L, Continuous separation of non-magnetic particles inside ferrofluids, Microfluid Nanofluid, 2010; 9: 1003–1009.

[115] Hahn YK, Park J-K, Versatile immunoassays based on isomagnetophoresis, Lab Chip 2011; 11: 2045–2048.

[116] Zhu T, Cheng R, Liu Y, He J, Mao L, Combining positive and negative magnetophoreses to separate particles of different magnetic properties, Microfluid Nanofluid 2014; 17: 973–982.

[117] Cheng R, Zhu T, Mao L, Three-dimensional and analytical modeling of microfluidic particle transport in magnetic fluids, Microfluid Nanofluid, 2014; 16: 1143–1154.

[118] Tarn MD, Hirota N, Iles A and Pamme N, On-chip diamagnetic repulsion in continuous flow, Sci Technol Adv Mater, 2009; 10: 014611.

[119] Pamme N, Manz A, On-Chip Free-Flow Magnetophoresis: Continuous flow separation of magnetic particles and agglomerates, Anal Chem, 2004; 76: 7250–7256.

[120] Pamme N, Eijkel JCT, Manz A, On-chip free-flow magnetophoresis: Separation and detection of mixtures of magnetic particles in continuous flow, J Magn Magn Mater, 2006; 307: 237–244.

[121] Liu C, Lagae L, Speetjens RW, Borghs G, On-chip separation of magnetic particles with different magnetophoretic mobilities, Journal of Applied Physics, 2007; 101: 024913.

[122] Adams JD, Kim U, Soh HT, Multitarget magnetic activated cell sorter, Proc Natl Acad Sci USA, 2008; 105: 18165–18170.

[123] Latham AH, Freitas RS, Schiffer P, Williams ME, Capillary magnetic field flow fractionation and analysis of magnetic nanoparticles, Anal Chem, 2005; 77: 5055–5062.

[124] McCloskey KE, Chalmers JJ, Zborowski M, Magnetic cell separation: characterization of magnetophoretic mobility, Anal Chem, 2003; 75: 6668–6874.

[125] Graham DL, Ferreira HA, Freitas PP, Magneto resistive based biosensors and biochips, Trends Biotechnol, 2004; 22: 455–462.

[126] Modak N, Pal AR, Datta A and Ganguly R, Bioseparation in a microfluidic channel using magnetic field flow fractionation, Int J Micro Nanoscale Transp, 2012; 3: 21.

[127] Modak N, Datta A, Ganguly R, Influence of the microchannel geometry on magnetophoretic separation of functionalized magnetic beads in a microfluidic sorter and field flow fractionation device, Magnetohydrodynamics, 2013; 49: 391-396.

[128] Williams PS, Carpino F and Zborowski M, Characterization of magnetic nanoparticlesusing programmed quadrupole magneticfield-flow fractionation, Phil Trans R Soc A, 2010; 368: 4419-4437.

[129] Carpino F, Moore LR, Chalmers JJ, Zborowski M and Williams PS, Quadrupole magnetic field-flow fractionation for the analysis of magnetic nanoparticles, J Phys: Conf Ser, 2005; 17: 174-180.

[130] Springston SR, Myers MN, Giddings JC, Continuous particle fractionation based on gravitational sedimentation in split thin cells, Anal Chem, 1987; 59: 344–350.

[131] Giddings JV, Field-flow fractionation: analysis of macromolecular, colloidal, and particulate materials, Science, 1993; 260: 1456–1465.

[132] Fuh CB, Chen SY, Magnetic split-flow thin fractionation of magnetically susceptible particles, J Chromatograph A, 1999; 857: 193–204.

[133] Cantado C, Reschiglian P, Faccini S, Zattoni A, Dondi F, Continuous split-flow thin cell and gravitational field-flow fractionation of wheat starch particles, J Chromatograph A, 2000; 871: 449–460.

[134] Fuh CB, Split-flow thin fractionation, Anal Chem, 2000; 72: 266A–271A.

[135] Cardot P, Batta S, Sinon A, Delage C, Hyphenation of sedimentation field flow fractionation with flow cytometry, J Chromatograph B 2002; 768: 285–295.

[136] Tsai H, Fang YS, Fuh CB, Analytical and preparative applications of magnetic split-flow thin fractionation on several ion-labeled red blood cells, BioMagnetic Research and Technology, 2006; 4: 1–7.

[137] Zhang Y, Emerson DR, Reese JM, General theory for flow optimisation of split-flow thin fractionation, J Chromatograph A, 2003; 1010: 87–94.

[138] Williams PS, Decker K, Nakamura M, Chalmers JJ, Moore LR, Zborowski M, Splitter imperfections in annular split-Flow thin separation channels: Experimental study of nonspecific crossover, Anal Chem, 2003; 75: 6687–6695.

[139] Zhang Y, Emerson DR, Effect of flow development region and fringing magnetic force field on annular split-flow thin fractionation, J Chromatograph A, 2004; 1042: 137–145.

[140] Fuh CB, Tsai HY, Lai JZ, Development of magnetic split-flow thin fractionation for continuous particle separation, Anal Chimia Acta, 2003; 497: 115–122.

[141] Hoyos M, Moore L, Williams PS, Zborowski M, The use of a linear Halbach array combined with a step-SPLITT channel for continuous sorting of magnetic species, J Magn Magn Mater, 2011; 323: 1384–1388.

[142] Hoyos M, Moore LR, McCloskey KE, Margel S, Zuberid M, Chalmers JJ, Zborowski M, Study of magnetic particles pulse-injected into an annular SPLITT-like channel inside a quadrupole magnetic field, Journal of Chromatography A, 2000; 903: 99–116.

[143] Ganguly R, Puri IK, Field-assisted self-assembly of superparamagnetic nanoparticles for bio-medical, MEMS and bioMEMS applications, Adv Appl Mech, 2007; 41:293–335.

[144] Modak N, Datta A, Ganguly R, Immunomagnetic Separation and Transport of Magnetic Beads in Microfluidic Field Flow Fractionation Devices for Bio-MEMS Application, Procedia Engineering, 2015; 127: 1243-1249

[145] Smistrup K, Hansen O, Bruus H, Hansen MF, Magnetic separation in microfluidic systems using microfabricated electromagnets—experiments and simulations, J Magn Magn Mater, 2005; 293: 597–604.

[146] Clift R, Grace JR, Weber ME (1978) Bubbles drops and particles. Academic Press, New York.

[147] Hwang JY, Youn S, Yang IH, Gravitational field flow fractionation: Enhancing the resolution power by using an acoustic force field, Anal Chim Acta, 2019; 1047: 238-247.

[148] Ganguly R, Sen S, Puri IK, Heat transfer augmentation in a channel with a magnetic fluid under the influence of a linedipole, J Magn Magn Mater, 2004; 271: 63–73.

[149] Faeth GM, Evaporation and combustion of sprays, Prog Energy Combust Sci, 1983; 9:1–76.

[150] Hirt CW, Nicols BD, Romero NC (1975) SOLA — A Numerical solution algorithm for transient fluid flows. Los Alamos Scientific Laboratory Report LA-5852 Los Alamos, New Mexico.

[151] Patankar SV (1980) Numerical heat transfer and fluid flow. Hemisphere Publishing Corporation, Washington.

[152] Sinha A, Ganguly R, and Puri IK, Numerical investigation of flow-through immunoassay in a microchannel, Journal of Applied Physics, 2010; 107: 034907.

[153] McDonald JC et al, Fabrication of microfluidic systems in poly(dimethylsiloxane). Electrophoresis, 2000; 21: 27–40.

[154] Thorsen T, Maerkl SJ, Quake SR, Microfluidic large-scale integration. Science, 2002; 298: 580–584.

[155] Basore JR, Baker LA, Applications of microelectromagnetic traps, Anal Bioanal Chem, 2012; 403: 2077–2088.

[156] Li X, Ballerini DR, Shena W, A perspective on paper-based microfluidics: Current status and future trends, BIOMICROFLUIDICS, 2012; 6: 011301.

[157] Stone HA, Stroock AD, Ajdari A, Engineering flows in small devices: microfluidics toward a lab-on-a-chip. Annu Rev Fluid Mech, 2004; 36: 381–411.